

CERN-TH/95-263  
 HD-THEP-95-44  
 HU-TFT-95-57  
 IUHET-318  
 hep-lat/9510020  
 October 12, 1995

**THE ELECTROWEAK PHASE TRANSITION:  
 A NON-PERTURBATIVE ANALYSIS**

K. Kajantie<sup>a,b,1</sup>, M. Laine<sup>a,c,2</sup>, K. Rummukainen<sup>d,3</sup> and M. Shaposhnikov<sup>b,4</sup>

<sup>a</sup>*Department of Physics, P.O.Box 9, 00014 University of Helsinki, Finland*

<sup>b</sup>*Theory Division, CERN, CH-1211 Geneva 23, Switzerland*

<sup>c</sup>*Institut für Theoretische Physik, Philosophenweg 16,  
 D-69120 Heidelberg, Germany*

<sup>d</sup>*Indiana University, Department of Physics, Swain Hall West 117,  
 Bloomington IN 47405 USA*

**Abstract**

We study on the lattice the 3d SU(2)+Higgs model, which is an effective theory of a large class of 4d high temperature gauge theories. Using the exact constant physics curve, continuum ( $V \rightarrow \infty, a \rightarrow 0$ ) results for the properties of the phase transition (critical temperature, latent heat, interface tension) are given. The 3-loop correction to the effective potential of the scalar field is determined. The masses of scalar and vector excitations are determined and found to be larger in the symmetric than in the broken phase. The vector mass is considerably larger than the scalar one, which suggests a further simplification to a scalar effective theory at large  $m_H$ . The use of consistent 1-loop relations between 3d parameters and 4d physics permits one to convert the 3d simulation results to quantitatively accurate numbers for different physical theories, such as the Standard Model – excluding possible nonperturbative effects of the U(1) subgroup – for Higgs masses up to about 70 GeV. The applications of our results to cosmology are discussed.

---

<sup>1</sup>kajantie@phcu.helsinki.fi

<sup>2</sup>mlaine@rock.helsinki.fi

<sup>3</sup>kari@trek.physics.indiana.edu

<sup>4</sup>mshaposh@nxth04.cern.ch

# 1 Introduction

The 3d  $SU(2)\times U(1)$ +Higgs model is a universal theory for the description of the electroweak phase transition in the standard electroweak theory and many extensions thereof, including the MSSM [1–5] (for a motivation of the study of the electroweak phase transition, see [1–4]). In the present paper, we study with lattice simulations the dominant  $SU(2)$ +Higgs part of the theory, defined by the Lagrangian

$$L = \frac{1}{4}F_{ij}^a F_{ij}^a + (D_i\phi)^\dagger(D_i\phi) + m_3^2\phi^\dagger\phi + \lambda_3(\phi^\dagger\phi)^2. \quad (1.1)$$

The procedure of dimensional reduction [2], [6–13] allows one to compute perturbatively the relationship between the temperature  $T$  and the physical parameters of the underlying 4d electroweak theory or its extensions, and the parameters of the 3d theory. Concrete formulae for the  $SU(2)$ +Higgs model and MSM can be found in [5] (see also below).

The aim of the present paper is to study the 3d  $SU(2)$ +Higgs model, especially its phase diagram, on the lattice. We confine ourselves to a small ratio  $\lambda_3/g_3^2 < 1/8$ , which in 4d terms corresponds to the case of small Higgs masses,  $m_H < m_W \approx 80$  GeV. This case seems to be the most interesting one for cosmological applications, because the phase transition at least in this region is of first order.

First Monte Carlo results on the electroweak phase transition using a 3d effective theory have already been given in [1, 3], see also [14, 15]. In comparison with [1, 3] we considerably extend numerical calculations. This makes it possible to determine for the first time or more accurately than previously a number of finite  $T$  quantities such as latent heat, correlation lengths, interface tension, magnitude of the higher order perturbative terms, etc. An essential ingredient in the increased accuracy is that the continuum-lattice mapping formulae, which are exact in 3d, are now known [4, 16]. Thus the continuum limit  $V \rightarrow \infty, a \rightarrow 0$  can be carried out under controlled conditions. Preliminary results of the simulations described here were published in [17].

Lattice Monte Carlo studies of the 4d  $SU(2)$ +Higgs model have been reported in [18–23]. Whenever comparison can be made, the results are in agreement within errorbars. However, the 3d approach used in this paper gives much smaller errors than the 4d one. Monte Carlo simulations of the  $O(4)$  pure scalar theory in 3d with a non-analytic cubic term have been performed in [14]. The spectrum of excitations in this theory, however, is very different from that of the  $SU(2)$  model, so that comparison is not possible.

The paper is organized as follows. In Section 2 we present the basic relations for the 3d  $SU(2)$ +Higgs model in continuum and on lattice. In Section 3 we describe the Monte Carlo update algorithm. In Section 4 we study the properties of the broken phase and the convergence of perturbation theory there. Section 5 is a lattice investigation of the phase transition for different values of the scalar self-coupling. In Section 6 we measure the different correlation lengths, and in Section 7 we study the metastability region and

the properties of the symmetric phase. Section 8 contains a short account of simulations with a larger Higgs mass, and in Section 9 we discuss the problem of studying large Higgs masses more generally. In Section 10 we summarize the information acquired on lattice about the properties of the 3d SU(2)+Higgs theory, and compare to perturbation theory and to some non-perturbative approaches. In Section 11 we relate the 3d lattice results to 4d continuum physics. Section 12 is a discussion of some implications of our results to cosmology. The conclusions and proposals for future work are in Section 13.

Readers not interested in details of lattice simulations could check tables 5-7, and go directly to Section 10, which contains a summary of the non-perturbative results.

In this paper we use results from [2] and [4]. All references to specific formulae from these papers are indicated by I and II followed by the number of the corresponding expression.

## 2 3d theory in continuum and on lattice

To make the paper self-contained, we summarize here the essential properties of the 3d theory in continuum and on lattice. A more detailed discussion can be found in [4, 5, 16].

The two couplings  $g_3^2$  and  $\lambda_3$  of the theory in eq. (1.1) have the dimensionality of mass. They do not possess ultraviolet renormalization and, say, in the  $\overline{\text{MS}}$  scheme are scale ( $\mu$ ) independent. The mass squared of the scalar field has a linear and logarithmic divergence on the 1- and 2-loop levels, respectively. In the  $\overline{\text{MS}}$  scheme the relation between the scalar mass and the renormalization-group invariant parameter  $\Lambda_m$  is

$$m_3^2(\mu) = \frac{f_{2m}}{16\pi^2} \log \frac{\Lambda_m}{\mu}, \quad (2.1)$$

where, in the SU(2)+Higgs theory,

$$f_{2m} = \frac{51}{16}g_3^4 + 9\lambda_3g_3^2 - 12\lambda_3^2. \quad (2.2)$$

Since all the three parameters of the 3d theory are dimensionful, the theory is uniquely fixed by giving three parameters, the gauge coupling of dimension mass and two dimensionless ratios:

$$g_3^2, \quad x \equiv \frac{\lambda_3}{g_3^2}, \quad y \equiv \frac{m_3^2(g_3^2)}{g_3^4} = \frac{1}{g_3^4} \frac{f_{2m}}{16\pi^2} \log \frac{\Lambda_m}{g_3^2}. \quad (2.3)$$

Renormalization introduces an intermediate mass scale on which the physics does not depend.

The 3d theory of eq. (1.1) is described on a lattice with the lattice constant  $a$  by the action

$$\begin{aligned}
S &= \beta_G \sum_x \sum_{i < j} (1 - \frac{1}{2} \text{Tr } P_{ij}) + \\
&- \beta_H \sum_x \sum_i \frac{1}{2} \text{Tr } \Phi^\dagger(\mathbf{x}) U_i(\mathbf{x}) \Phi(\mathbf{x} + i) + \\
&+ \sum_x \frac{1}{2} \text{Tr } \Phi^\dagger(\mathbf{x}) \Phi(\mathbf{x}) + \beta_R \sum_x [\frac{1}{2} \text{Tr } \Phi^\dagger(\mathbf{x}) \Phi(\mathbf{x}) - 1]^2.
\end{aligned} \tag{2.4}$$

The three dimensionless parameters  $\beta_G, \beta_H, \beta_R$  of eq. (2.4) are in the continuum limit  $a \rightarrow 0$  related to the three dimensionless parameters  $g_3^2 a, x, y$  by the following equations:

$$g_3^2 a = \frac{4}{\beta_G}, \tag{2.5}$$

$$x = \frac{1}{4} \lambda_3 a \beta_G = \frac{\beta_R \beta_G}{\beta_H^2}, \tag{2.6}$$

$$\begin{aligned}
y &= \frac{\beta_G^2}{8} \left( \frac{1}{\beta_H} - 3 - \frac{2x\beta_H}{\beta_G} \right) + \frac{3\Sigma\beta_G}{32\pi} (1 + 4x) + \\
&+ \frac{1}{16\pi^2} \left[ \left( \frac{51}{16} + 9x - 12x^2 \right) \left( \ln \frac{3\beta_G}{2} + \zeta \right) + 5.0 + 5.2x \right].
\end{aligned} \tag{2.7}$$

Eq. (2.7) depends on several constants arising from lattice perturbation theory;  $\Sigma = 3.17591$ ,  $\zeta = 0.09$  and the two numbers 5.0 and 5.2, specific for SU(2)+Higgs theory, and computed in [16]. This reference also gives the analogous numbers for some other relevant 3d theories. Note that the logarithmic 2-loop term on the second line in eq. (2.7) is absolutely necessary with the accuracy which we have in our lattice simulations. For instance, changing the number 5.0 in the 2-loop part by 0.05 changes the critical temperature by an amount equal to the statistical uncertainty in one of our lattice simulations ( $138.38 \pm 0.05$  GeV).

When the lattice constant  $a$  is varied, eqs. (2.5–2.7) define for the fixed parameters  $g_3^2, x, y$  of eq. (2.3) a curve, the constant physics curve (CPC), in the space of  $\beta_G, \beta_H, \beta_R$ . All the curves end in the point  $(\infty, 1/3, 0)$  for  $a \rightarrow 0$ .

The above discussion was entirely confined to the 3d theory. As explained in [5], a single 3d theory is the effective theory of a large class of finite  $T$  field theories and we shall later give several quantitative examples of this. For each 4d theory one separately has to establish the transformation from the physical parameters of the 4d theory to  $g_3^2, x, y$ . For the Standard Model these are given in [5].

Since the use of the 3d parameters  $g_3^2, x, y$  is rather unilluminating, we shall in the presentation of lattice results replace them by a ‘‘Higgs mass’’  $m_H^*$  and ‘‘temperature’’  $T^*$  using the following equations:

$$g_3^2 \equiv 0.44015 T^*, \tag{2.8}$$

$$x = \frac{\lambda_3}{g_3^2} = -0.00550 + 0.12622h^2, \quad (2.9)$$

$$y = \frac{m_3^2(g_3^2)}{g_3^4} \quad (2.10)$$

$$= 0.39818 + 0.15545h^2 - 0.00190h^4 - 2.58088 \frac{(m_H^*)^2}{(T^*)^2},$$

where

$$h \equiv \frac{m_H^*}{80.6 \text{ GeV}}. \quad (2.11)$$

These equations follow from the tree-level formulae

$$g = 2/3, \quad \lambda = \frac{1}{8}g^2 \frac{(m_H^*)^2}{m_W^2}, \quad m_W = 80.6 \text{ GeV}, \quad m_D = \sqrt{\frac{5}{6}}gT = 0.60858T, \quad (2.12)$$

from a formula relating  $m_3^2(\mu)$  to 4d quantities (I.66), and from a subsequent integration over the  $A_0$ -field [2]. Each quoted set of  $(m_H^*, T^*)$  can with eqs. (2.8–2.10) be converted to a set of  $g_3^2, x, y$ , which for a given theory can, as discussed in Sec. 11, in turn be converted to a precise set of values for the zero-temperature pole Higgs mass and the physical temperature. For the SU(2)+Higgs theory without fermions the difference between the simplified parameters  $m_H^*, T^*$  and the physical parameters is relatively small.

In studying the phase structure of the 3d theory we search for a critical curve in the  $(x, y)$ -plane. On the tree level this curve is the line  $y = 0$ : for  $y > 0$  the theory is in a symmetric, for  $y < 0$  in a broken phase. In 1- or 2-loop perturbation theory the line splits in three: a critical curve  $y = y_c(x)$  and upper and lower ends  $y = y_{\pm}(x)$  of metastability branches. On the critical curve the system can exist in two different phases with the same vacuum energy  $\epsilon_{\text{vac}}$  but different values of various gauge invariant condensates like  $\langle \phi^\dagger \phi \rangle$ . The broken phase exists for  $y < y_+(x)$ , the symmetric phase for  $y > y_-(x)$ . One knows that perturbation theory can never conclusively determine the curve  $y = y_c(x)$  or the jumps of various gauge invariant condensates like  $\langle \phi^\dagger \phi \rangle$  across the curve, and the main purpose of the lattice Monte Carlo study is to do this. For instance, one is interested in knowing whether the curve  $y = y_c(x)$  continues to large ( $> 1/8$ ) values of  $x$  or whether it terminates. Our present simulations do not provide an answer to the last question.

When performing simulations with the action (2.4), the procedure is somewhat different depending on whether one is performing simulations at some fixed  $(x, y)$  or whether one is searching for the critical curve  $y = y_c(x)$ .

Assume first that one is studying the system, e.g., determining correlation lengths or the value of  $\langle \phi^\dagger \phi \rangle$ , at some fixed  $(x, y)$ . The procedure then is as follows. Choose some  $\beta_G$  which then gives the lattice constant  $a$ . The value of  $\beta_G$  on an  $N^3$  lattice should satisfy the constraints that the smallest correlation length is larger than  $a$  and

the largest correlation length is smaller than  $Na$ . The former requirement gives a lower limit for  $\beta_G$  and the latter a lower limit for  $N$ . Since  $(x, y)$  are fixed, eq. (2.7) gives the value of  $\beta_H$  and eq. (2.6) the value of  $\beta_R$ . Simulate the system with these values for larger and larger  $N$  and perform an extrapolation to  $N \rightarrow \infty$ . Choose then larger and larger values of  $\beta_G$  (smaller and smaller  $a$ ) doing always the same. The set of different extrapolations to  $N \rightarrow \infty$  can then be extrapolated to  $\beta_G \rightarrow \infty$  ( $a \rightarrow 0$ ), which is the final continuum limit.

When searching for the critical curve  $y_c(x)$ , one can in the beginning only fix the value of  $x$ . Then one again first chooses  $\beta_G$  subject to the constraints given above, simulates the system for various  $\beta_H$  with  $\beta_R = x\beta_H^2/\beta_G$  and finds the value of  $\beta_{H,c}$ . Extrapolating at fixed  $\beta_G$  to  $N = \infty$  gives a value  $\beta_{H,c}(N = \infty)$  which using eq. (2.7) can be converted to a value of  $y(x)$  at this  $a$ . The extrapolation to  $a \rightarrow 0$  is carried out as before and gives the final  $y = y_c(x)$ .

### 3 The Monte Carlo update algorithm

The lattice spacing  $a$  and the linear lattice size  $Na$  are constrained by the length scales set by the  $W$  and Higgs masses:  $a \ll 1/m_W(T) < 1/m_H(T) \ll Na$  (assuming  $m_H(T) < m_W(T)$ ). Even though this requirement is much milder than the 4d one ( $a \ll 1/T$ ) [4], in many cases it still mandates quite large lattice sizes (our largest volume is  $50^2 \times 200$ ). Therefore, it is important that the update algorithm be as efficient as possible.

The gauge field update is not qualitatively different from the standard SU(2) pure gauge update, in spite of the hopping term  $\text{Tr} \Phi^\dagger(\mathbf{x})U_i(\mathbf{x})\Phi(\mathbf{x} + i)$  in the action. To update the gauge links we use the conventional reflection overrelaxation and Kennedy-Pendleton heat bath [24] methods. All the gauge field modes are much ‘faster’ than the Higgs modes, i.e., they have much shorter autocorrelation times.

Due to the flatness of the Higgs potential, the ‘slow’ modes of the system are associated with the radial sector of the Higgs field  $\Phi = RV$ ,  $R \geq 0$ ,  $V \in \text{SU}(2)$ . In what follows we summarize the more non-standard methods we use to increase the efficiency of the update program.

**Global radial update.** First improvement comes from multiplying the radial part of the Higgs field at all locations simultaneously by the *same* factor:  $R(\mathbf{x}) \rightarrow e^\xi R(\mathbf{x})$ , where  $\xi$  is randomly chosen from a constant distribution around zero:  $\xi \in [-\epsilon, \epsilon]$ . Under this update, the action (2.4) changes as  $\Delta S(\xi) = ae^{2\xi} + be^{4\xi} - a - b$ , where  $a$  and  $b$  are the sums of the terms proportional to  $R^2$  and  $R^4$  in the action. Accounting for the measure factors, the update is accepted with the Metropolis probability  $p(\xi) = \min(1, \exp[4V\xi - \Delta S(\xi)])$ , where  $V$  is the volume of the system.

The multiplication factor  $e^\xi$  has to be very close to unity in order for  $p(\xi)$  to be non-negligible. In practice, we choose  $\xi$  from a window of width  $\sim 0.05 - 0.001$  around zero, depending on the volume. The width of the window is chosen so that the acceptance is approximately 60–70%.

In fig. 1 we show the autocorrelation functions for an  $m_H^* = 60$ ,  $\beta_G = 8$  system on a  $14^3$  lattice with both (a) local Metropolis and (b) local + global update. Even though the change in  $R(x)$  in each global multiplication is very small, the gain over only local Metropolis/heat bath is about a factor of 5. The additional cost of the global update in terms of cpu time is negligible, since it involves only one accept/reject step for the whole volume.

**Higgs field overrelaxation.** Let us parametrize the Higgs field as  $\Phi = \alpha_\mu \tau_\mu$ ,  $\mu = 0 \dots 3$ ,  $\alpha_\mu \in \mathbf{R}$ , where  $\tau_i$  are Pauli matrices and  $\tau_0$  is the  $2 \times 2$  unit matrix. From eq. (2.4) we see that the local potential of the Higgs field at location  $\mathbf{x}$  is

$$V[\Phi(\mathbf{x})] = -\alpha_\mu(\mathbf{x})F_\mu(\mathbf{x}) + R(\mathbf{x})^2 + \beta_R(R(\mathbf{x})^2 - 1)^2 \quad (3.1)$$

where  $R^2 = \alpha_\mu \alpha_\mu$  and  $F_\mu$  is the sum of the hopping terms

$$F_\mu(\mathbf{x}) = \beta_H \frac{1}{2} \text{Tr} \tau_\mu \left[ \sum_{i=1,2,3} \Phi^\dagger(\mathbf{x} - i) U_i(\mathbf{x} - i) + \Phi^\dagger(\mathbf{x} + i) U_i^\dagger(\mathbf{x}) \right]. \quad (3.2)$$

This form seems to suggest separate update steps for the radial and SU(2)-components of the Higgs field. However, this is *not* the optimal method: even though the overrelaxation for the SU(2) direction can be readily performed, updating the radial component becomes quite complicated. In this case the overrelaxation step  $R \rightarrow R'$  would require finding  $R'$  so that

$$[dG(R)/dR]^{-1} \exp[-G(R)], \quad \text{where} \quad G(R) = V(R) - \log R^3, \quad (3.3)$$

remains invariant (here we use a notation where the  $\mathbf{x}$ -dependence of the variables is suppressed). This can be approximated by finding a solution  $R'$  to the equation  $G(R') = G(R)$ , and performing a Metropolis accept/reject step using the probability weight  $[dG(R)/dR]/[dG(R')/dR']$ . This update has been used in 4d Higgs model simulations [25, 21]. However, the acceptance rate is only  $\sim 80\%$ , and the algorithm behaves dynamically rather like a heat bath or Metropolis update.

A more efficient method is to update the Higgs variables in the plane defined by 4-dimensional vectors  $\alpha_\mu$  and  $F_\mu$ , using the Cartesian components of  $\alpha_\mu$  parallel and perpendicular to  $F_\mu$ :

$$X = \alpha_\mu f_\mu, \quad Y_\mu = \alpha_\mu - X f_\mu, \quad (3.4)$$

where  $f_\mu = F_\mu/F$  and  $F = \sqrt{F_\mu F_\mu}$ . In terms of  $X$  and  $Y_\mu$  eq. (3.1) becomes

$$V[\Phi] = -XF + (1 + 2\beta_R(Y^2 - 1))X^2 + \beta_R(X^4 + Y^4). \quad (3.5)$$

Now we can update the  $X$  and  $Y$  components of  $\Phi$  separately: overrelaxation in  $Y$  is simply the reflection  $Y_\mu \rightarrow Y'_\mu = -Y_\mu$ , or  $\alpha'_\mu = -\alpha_\mu + 2Xf_\mu$  (this is exactly equivalent to the conventional SU(2) reflection overrelaxation procedure). In order to perform an exact overrelaxation to the  $X$ -component, we need to find  $X'$  so that

$$[dV(X')/dX']^{-1} \exp[-V(X')] = [dV(X)/dX]^{-1} \exp[-V(X)]. \quad (3.6)$$

To solve this equation we would have to resort to iterative numerical methods, which can be costly in terms of cpu-time. Instead, we used the following approximation to the overrelaxation (3.6): we find the solution to equation  $V(X') = V(X)$  and accept  $X'$  with the probability

$$p(X') = \min(p_0, 1), \quad p_0 = \frac{dV(X)/dX}{dV(X')/dX'}. \quad (3.7)$$

Since  $V(X)$  is a fourth order polynomial, solving the equation  $V(X') = V(X)$  boils down to finding zeros to a third order polynomial (we already know one zero  $X' = X$ , which can be factored out). In all realistic cases the parameters of  $V(X)$  are such that there always is only one other real root, and it is straightforward to write a closed expression for  $X'$ . This update is an almost perfect overrelaxation: in our simulations the acceptance rate varies between 99.7% – 99.98%, depending on the  $\beta_G$  used. The acceptance is high enough so that the “diffusive” update dynamics inherent in the Metropolis acceptance step does not play any role, and the evolution of the field configurations is almost deterministic. A different but related overrelaxation schema to the one described here has also been used in 4d simulations [22].

**Wavefront update.** Let us next consider the order in which the lattice variables are traversed. In the conventional even-odd update, the lattice is decomposed into even and odd sectors – in our 3d case, to two sets with  $x + y + z$  even and odd. The variables are first updated on all the even points before updating the odd points. Using this schema it takes  $L/2$  whole lattice updates before any kind of signal from a given location on the lattice can propagate through the whole volume.

In the wavefront traversal we pick an arbitrary 2-dimensional plane from the system, defined by one of the conditions  $\pm x \pm y \pm z = \text{const.}$  (modulo periodic boundary conditions). We select one of the directions perpendicular to the plane to be the positive direction. The update proceeds in two stages: first, we update the Higgs variables  $\Phi$  on this plane, and second, the gauge matrices  $U$  on the links emanating from this plane to the positive direction. Both updates are performed with the overrelaxation algorithms. After the gauge field update we move up to the next plane to the positive direction, and start the updates again. With this method, a planar wave of overrelaxation updates propagates through the volume in a single update sweep. In our implementation we keep the same orientation of the plane until the volume has been swept through 4–9 times.



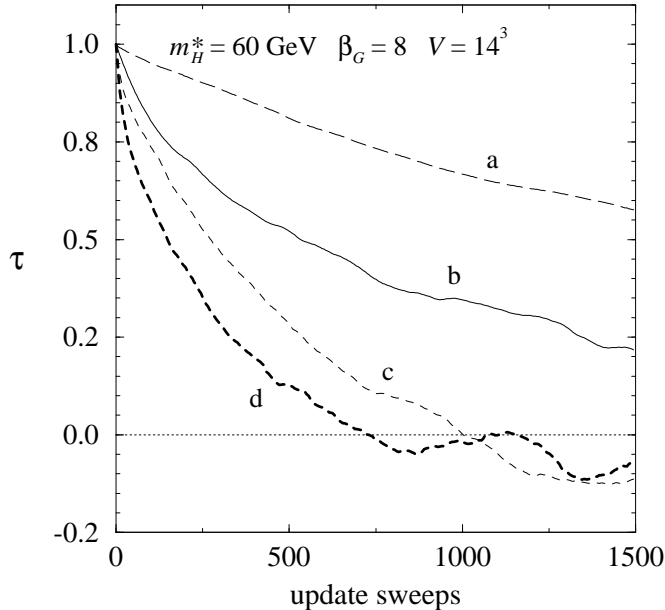


Figure 1: The autocorrelation function of the observable  $L = V^\dagger(\mathbf{x})U_i(x)V(\mathbf{x} + i)$  calculated from an  $m_H^* = 60$  GeV,  $V = 14^3$  lattice. (a) Heat bath/Metropolis, (b) Heat bath/Metropolis with global  $R$ -update, (c)  $4\times$  (overrelaxation with even-odd traversal) +  $1\times$  (heat bath + global update), and (d)  $4\times$  (wavefront overrelaxation) +  $1\times$  (heat bath + global update). In all the cases, one update means going once through all the lattice points.

The particular diagonal orientation of the plane is chosen in order to simplify the update: the spins and gauge links on the plane can be updated independently of each other, and all the gauge links have an equal footing with respect to the plane — there are no link variables within the plane, as would be the case if the plane was oriented along the principal axes.

In fig. 1 we compare the autocorrelation functions of the standard even-odd overrelaxation (c) and the wavefront overrelaxation (d). In both cases we perform four overrelaxation sweeps through the volume, followed by one heat bath/Metropolis update and one global radial update. For both cases the individual Higgs variable overrelaxation step is the  $XY$  overrelaxation described in paragraph II above. The overrelaxation methods perform much better than the pure heat bath algorithms (a and b). The wavefront overrelaxation has much better initial decorrelation, as seen from the very rapid decrease in the autocorrelation function, even though it seems to have roughly the same exponential autocorrelation time as the conventional even-odd method. However, this rapid initial decrease means that the *integrated autocorrelation time*  $\tau_{\text{int}}$  is small, giving correspondingly small statistical errors for the observables. In our tests the wavefront overrelaxation had typically 1.5–3 times smaller  $\tau_{\text{int}}$  than the even-odd overrelaxation.

**Multicanonical update.** Multicanonical update [26] is essential for the interface tension calculations with the histogram method (see Sec. 5.3). At the transition temperature the probability distribution of some order parameter, say  $R^2$ , has two distinct peaks corresponding to the two pure phases. The probability that the system resides in a mixed state, consisting of domains of the two phases separated by phase interfaces, is suppressed by the interface tension times the area of the interface (see, for example, fig. 5).

To enhance the probability of the mixed states the action eq. (2.4) is modified with the multicanonical weight function  $W$ :

$$S_{\text{MC}} = S + W(R_S^2), \quad R_S^2 = \sum_x R(\mathbf{x})^2 \quad (3.8)$$

The weight function  $W(R_S^2)$  is chosen so that the resulting distribution  $p(R_S^2)$  is approximately constant in the interval  $R_{S,1}^2 \leq R_S^2 \leq R_{S,2}^2$ , where  $R_{S,1}^2$  and  $R_{S,2}^2$  denote the pure phase peak locations. This is the main disadvantage of the multicanonical method: a priori, the weight function is not known; an exact knowledge of the weight function is equivalent to knowing the probability distribution of the order parameter, which is one of the quantities we attempt to calculate with the Monte Carlo simulation.

The canonical expectation value of an operator  $\mathcal{O}$  can be calculated by reweighting the individual multicanonical measurements  $\mathcal{O}_k$  with the weight function:

$$\langle \mathcal{O} \rangle = \frac{\sum_k \mathcal{O}_k e^{-W(R_{S,k}^2)}}{\sum_k e^{-W(R_{S,k}^2)}} \quad (3.9)$$

where the sums go over all measurements of  $\mathcal{O}$  and  $R_S^2$ .

The choice of  $R_S^2$  for the argument of the weight function is by no means unique; equally well one could use, for example, the hopping term  $\sum_{x,i} \frac{1}{2} \text{Tr} \Phi^\dagger(\mathbf{x}) U_i(\mathbf{x}) \Phi(\mathbf{x}+i)$ . The advantage of  $R_S^2$  is that in this case the weight function does not modify the update of the gauge fields  $U$  and the SU(2)-direction of the Higgs field  $V$ . However, the  $XY$  overrelaxation described above has to be modified.

We parametrize  $W$  with a continuous piecewise linear function:

$$W(R_S^2) = w_i + (w_{i+1} - w_i) \frac{R_S^2 - r_i}{r_{i+1} - r_i}, \quad r_i \leq R_S^2 < r_{i+1}. \quad (3.10)$$

An initial guess for the parameters  $w_i$  can be obtained by finite size scaling the probability distributions obtained from simulations using smaller lattice sizes. If deemed necessary, the parameters are further adjusted after preliminary runs.

Since we perform most of the simulations with vector supercomputers, it is important to vectorize the multicanonical update. This is achieved with the following steps:

- (i) If  $r_i \leq R_S^2 < r_{i+1}$  initially, the weight function is fixed to the linear form  $W'(R_S^2) = w_i + (w_{i+1} - w_i)(R_S^2 - r_i)/(r_{i+1} - r_i)$  for all  $R_S^2$ .

- (ii) A number of Higgs variables are updated with the action  $S' = S + W'$ . Since  $W'$  is linear in  $R^2$ , it is straightforward to do this with a fully vectorized algorithm. We update  $\Phi$  in  $\sim 100$ – $200$  points in one vector.
- (iii) The whole vector of updates is accepted with the probability  $p_{\text{mc}} = \min(1, \exp[W'(R_S^2) - W(R_S^2)])$ .

Obviously, the acceptance in the step (iii) decreases when the number of variables updated in a single vector increases. Here the vector length  $\sim 100$  is short enough so that  $R_S^2$  in practice often remains between the limits  $r_i$  and  $r_{i+1}$  after the update, and the acceptance is exceptionally good: in our runs the rejection rate was only  $\sim 10^{-6}$ ! At the same time the vector length is long enough so that increasing it does not give any significant gain in computational speed. Thus, the performance hit caused by the implementation of the multicanonical algorithm is negligible.

The simulations were performed with Cray C-90 and X-MP supercomputers and, for the smaller volumes, with IBM RS6000 and HP 9000/735 workstations. The total amount of computing power used was about  $5 \cdot 10^{15}$  flop = 160 Mflops year.

## 4 Properties of the broken phase: the 3-loop effective potential

We shall first study the 3d SU(2)+Higgs system when it is in the broken phase. This will permit us to show the accuracy of the method and, in particular, to determine the size of the so far uncomputed 3-loop term in the effective potential (see (I.73), (II.151-152)), and verify that it is linear in  $\phi$ .

Although the object of study is the 3d theory, we use the simple parametrisation in eqs. (2.8–2.10) to permit one to use the 4d quantities  $m_H^*, T^*$  in fixing the 3d parameters  $x, y$ . Whenever  $m_H^*, T^*$  are quoted, the values of  $g_3^2, x, y$  are to be computed from eqs. (2.8–2.10). The same values of  $m_H^*, T^*$  can correspond to different physical parameters in different theories.

We study the effective potential in the broken phase with the help of the scalar condensate  $\langle \phi^\dagger \phi \rangle$  [4]. Eq. (II.139) relates the value of the scalar condensate in the  $\overline{\text{MS}}$  scheme, where

$$\langle \phi^\dagger \phi(\mu_1) \rangle - \langle \phi^\dagger \phi(\mu_2) \rangle = \frac{3g_3^2}{16\pi^2} \log \frac{\mu_1}{\mu_2}, \quad (4.1)$$

to the corresponding lattice quantity  $\langle R^2 \rangle$ . The relation, in which the correction term vanishes in the continuum limit, is

$$\frac{\langle \phi^\dagger \phi(\mu) \rangle}{g_3^2} = \frac{1}{8} \beta_G \beta_H \left( \langle R^2 \rangle - \frac{\Sigma}{\pi \beta_H} \right) - \frac{3}{(4\pi)^2} \left( \log \frac{3\beta_G g_3^2}{2\mu} + \zeta + \frac{1}{4} \Sigma^2 - \delta \right) + O\left(\frac{1}{\beta_G}\right). \quad (4.2)$$

$T^*$	110	145	155	165	167
$\langle \phi^\dagger \phi(T^*) \rangle / T^*$	1.9553(13)	0.7061(7)	0.4718(6)	0.2506(10)	0.2052(36)
$\mu = 1.2m_T$	1.9642	0.7184	0.4861	0.2707	0.2235
$\mu = 4.7m_T$	1.9650	0.7207	0.4898	0.2793	0.2359
CW $\mu = 1.2m_T$	1.9649	0.7206	0.4902	0.2818	0.2397
CW $\mu = 4.7m_T$	1.9660	0.7223	0.4922	0.2847	0.2433

Table 1: Measured and computed values of  $\langle \phi^\dagger \phi(T^*) \rangle / T^*$  for  $m_H^* = 80$  GeV and  $T^* = 110, 145, 155, 165, 167$  GeV. The first row gives the lattice value in the limit  $V \rightarrow \infty, a \rightarrow 0$ , obtained using eq. (4.2). The following two rows with  $\mu$ -values refer to the result in  $\hbar$  expansion including the 2-loop term and the known part of the 3-loop term (Appendix A, eq. (A.22) with  $\beta(h) = 0$ ), and the last two rows to a numerical CW calculation using the RG-improved 2-loop effective potential.

Here numerically  $\zeta + \frac{1}{4}\Sigma^2 - \delta = 0.67$ . Thus, the extrapolation of lattice measurements of the quantity  $\langle R^2 \rangle$  to the limit  $\beta_G \rightarrow \infty$  allows one to determine an "exact" value of the scalar condensate which then may be confronted with the perturbative expression.

We use the strategy appropriate for simulations at  $T < T_c$  as explained in Sec. 2. We take  $m_H^* = 80$  GeV and select several temperatures for which the system is in the broken phase:  $T^* = 110, 145, 155, 165, 166, 167$  GeV. For each temperature we choose different values of  $\beta_G$  (usually,  $6 \leq \beta_G \leq 32$ ). These numbers completely define the parameters of simulation through the constant physics curve (2.5-2.7). For every simulation, the volume of the system was large enough to make finite size effects smaller than the statistical uncertainty in  $\langle R^2 \rangle$ .

Examples of measurements at  $T^* = 110, 145$  GeV and  $165$  GeV are shown in figs. 2–3, and the values of  $\langle \phi^\dagger \phi(T^*) \rangle / T^*$  in the continuum limit are collected in table 1. The range of the temperatures used is quite wide, the expectation value of the Higgs field varies (in 4d units) from  $\phi_b/T^* \approx 2$  to  $\phi_b/T^* \approx 0.6$ .

The perturbative 2-loop computations were done with two methods, described in Sec. 5 of II. The first method is based on a straightforward  $\hbar$  expansion of the condensate. The result is given in Appendix A (eq.(A.22)) and shown in fig. 4. Fig. 4 contains the tree, 1-loop and 2-loop terms (eqs. (II.76-78)) but also that part of the 3-loop term which is known because it is related to lower order potentials. In the second method (which we call the CW – Coleman-Weinberg – type of computation), one numerically finds the location of the broken minimum of the 2-loop effective potential, determines the ground state energy, and then computes the condensate with the help of (II.42) as  $\partial V(\phi_b)/\partial m_3^2$ . To avoid infrared divergences, the straightforward CW-method has to be somewhat improved, see Appendix B.

The expansion parameter of the  $\hbar$  expansion is  $\sim g_3^2/\sqrt{-m_3^2}$  and thus it converges the better the deeper one is in the broken phase. This also means that the signal for

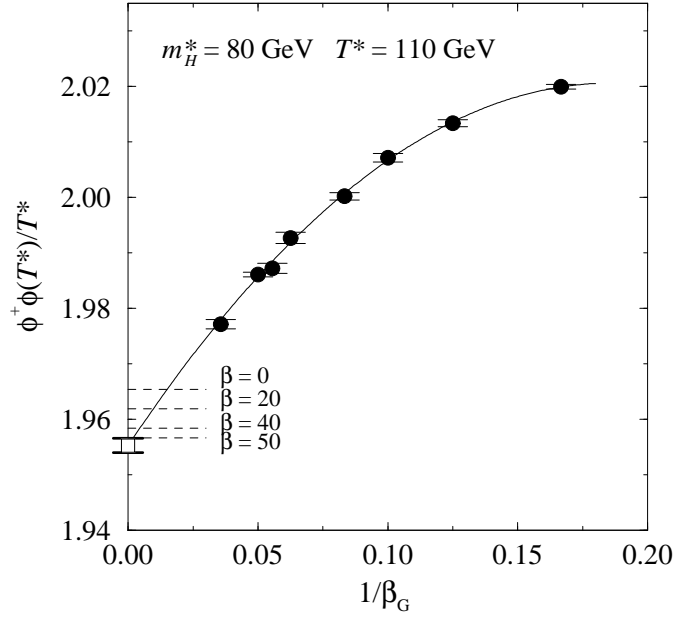


Figure 2: Data for  $\langle \phi^\dagger \phi(T^*) \rangle / T^*$  as a function of  $1/\beta_G$  for  $m_H^* = 80$ ,  $T^* = 110$  GeV computed from measured values of  $\langle R^2 \rangle$  using eq. (4.2) with  $\mu = T^*$ ,  $g_3^2 = 0.44015T^*$  (parametrisation in eq. (2.8)). The perturbative values corresponding to  $\beta = 0, 20, 40, 50$ , calculated with the CW-method at the scale  $\mu = 2.37m_T$  and then run to  $\mu = T^*$  with eq. (4.1), are shown on the vertical axis.

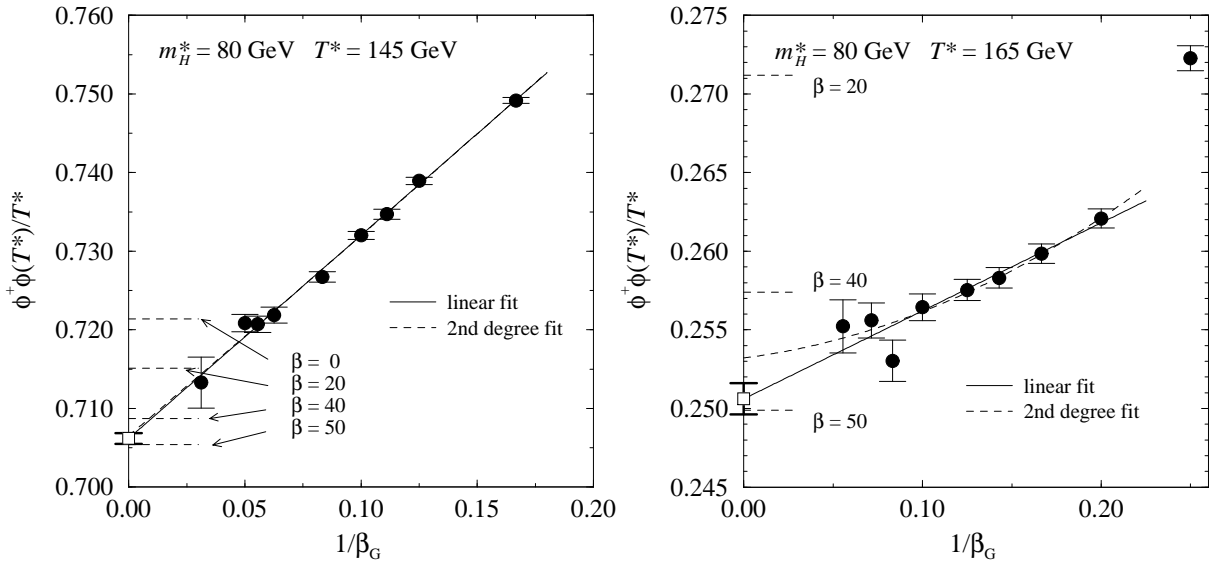


Figure 3: As fig. 2, but for  $T^* = 145$  GeV and  $T^* = 165$  GeV.

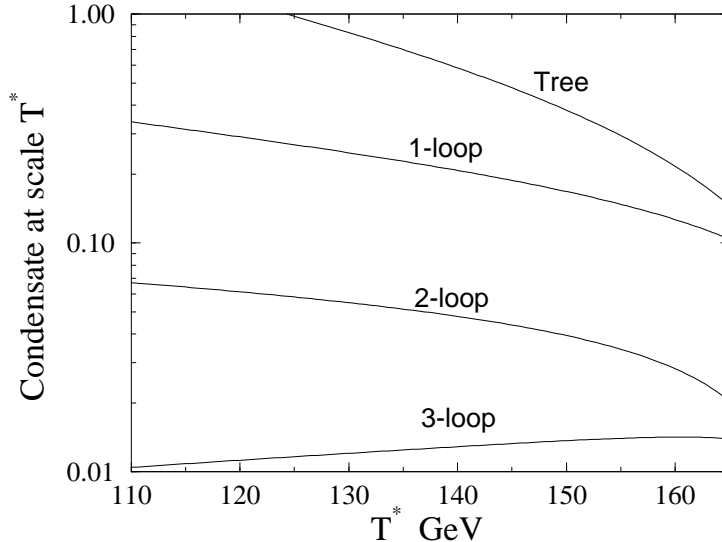


Figure 4: The values of  $\langle \phi^\dagger \phi(T^*) \rangle / T^*$  in the  $\hbar$  expansion as a function of temperature for  $m_H^* = 80$  GeV from eq. (A.22). The 3-loop curve contains the known part thereof, with  $\beta(h) = 0$ . It is seen that the  $\hbar$ -calculation becomes increasingly unreliable as one approaches the critical temperature.

the 3-loop term vanishes if one goes too deep into the broken phase. Since one cannot be too close to  $m_3^2 = 0$  (or  $T^* = 173.5$  GeV in table 1) either, there is an optimal region in between. The numerical CW method works also at  $T_c$  and is thus more accurate. We include the  $\hbar$  results mainly since the formulas are very explicit.

When all orders of perturbation theory are summed,  $\langle \phi^\dagger \phi(\mu) \rangle$  depends on  $\mu$  according to eq. (4.1). At a finite order in perturbation theory, however, there is extra  $\mu$ -dependence which can be used as an indication of the accuracy of the calculation. In table 1 the parameter  $\mu$  used in the calculation of  $\langle \phi^\dagger \phi(\mu) \rangle$  was varied within the limits  $0.5 \cdot 2.37 < \mu/m_T < 2 \cdot 2.37$ , the central value 2.37 (table 2 of I) being determined by the requirement of the "best" convergence of perturbation theory for the effective potential in the vicinity of the minimum. Then  $\langle \phi^\dagger \phi(\mu) \rangle$  was run to  $\mu = T^*$  according to the exact running in eq. (4.1).

Inspection of table 1 shows that the CW values of the condensate are practically independent of  $\mu$  so that the convergence of CW type perturbation theory is better than that of the ordinary one. The difference between these two methods is due to higher order corrections; the CW method sums a subset of them and can be used at the phase transition, where the first method fails<sup>5</sup>. One can see that the CW values of the condensate are larger than the corresponding lattice values, and that the difference

<sup>5</sup>The CW method provides an automatic summation of one-particle reducible diagrams, whereas in ordinary perturbation theory they have to explicitly calculated to the desired order, see Appendix A.

$T^*$	110	145	155	165	167
$\beta$	53.0(7.3)(2.7)	41.8(2.1)(5.1)	38.3(1.3)(6.7)	35.1(1.1)(12.0)	28.8(2.8)(14.4)
$\beta_{\text{CW}}$	58.0(7.4)(2.3)	48.1(2.3)(2.3)	46.6(1.8)(3.6)	49.1(1.3)(2.6)	46.2(3.6)(2.5)

Table 2: The values of the 3-loop coefficient  $\beta$  at different temperatures using the  $\hbar$  expansion and the numerical CW computation. The first number in brackets is statistical uncertainty and the second is an estimate of the systematic error associated with the change of the parameter  $\mu$  within the interval in table 1.

between the two is statistically significant. This proves the necessity of higher order effects and singles out their sign: the “exact” vev of the Higgs field at some fixed temperature is *smaller* than that given by 2-loop perturbation theory.

The study of the difference between the 2-loop and lattice values of the scalar condensate allows one to determine the magnitude and the structure of the 3-loop term. In CW perturbation theory for the scalar condensate we add to the 2-loop effective potential a linear term, expected on the 3-loop level (see (I.73)):<sup>6</sup>

$$\Delta V_3 = \frac{\beta}{(4\pi)^3} g_3^4 m_T(\phi). \quad (4.3)$$

Here  $\beta$  is a constant to be determined by fitting the prediction to the lattice number at each temperature (for constant  $m_H^*$ )<sup>7</sup>. In the  $\hbar$  expansion method the procedure is extremely simple: one takes  $\langle \phi^\dagger \phi(\mu) \rangle$  from eq. (A.22) of Appendix A, runs it to the scale  $T^*$  using eq.(4.1) and fits the constant  $\beta$  to get agreement with data. In other words,  $\beta$  is linearly proportional to the difference of the perturbative and the lattice value in table 1. The outcome of this procedure is in table 2.

Within the  $T^*$  range discussed the vev of the scalar field varies from  $0.6T^*$  to  $2T^*$ . Since the value of  $\beta$  does not depend on  $T^*$  within error bars, one may conclude on the basis of the lattice data that for  $m_H^*$  around 80 GeV there exists in the effective potential a 3-loop linear term with positive sign and  $\beta \simeq 50$ .

We estimated  $\beta$  at different Higgs masses also by another method. We computed on the lattice the continuum limit of the critical temperature and the value of the condensate at  $T_c^*$  (the methods are described in detail in the next section). We found for  $m_H^* = 60$  GeV that  $T_c^* = 138.38(5)$  GeV and  $\langle \phi^\dagger \phi(T_c^*) \rangle / T_c^* = 0.227(6)$ ; and for  $m_H^* = 70$  GeV that  $T_c^* = 154.52(10)$  GeV and  $\langle \phi^\dagger \phi(T_c^*) \rangle / T_c^* = 0.162(12)$ . These numbers may be reproduced with the 3-loop effective potential with  $\beta \simeq 49(2)$  and with  $\beta \simeq 46(4)$ , respectively. The small Higgs mass  $m_H^* = 35$  GeV is not informative

<sup>6</sup> The structure of the 3-loop effective potential is discussed in more detail in Appendix A.

<sup>7</sup>In [4] a rough estimate of the parameter  $\beta$  was given,  $\beta = -15(20)$  with only statistical errors quoted. After the analytical computation of the constant physics curve [16] the systematic errors can be removed, while the higher statistics allows to reduce the statistical errors considerably.

since higher order corrections at the critical temperature are numerically small and the extraction of  $\beta$  with any reasonable accuracy is not possible with the data we have.

Results at  $m_H^* = 60, 70$  GeV indicate that within errorbars,  $\beta$  does not depend on  $m_H^*$ . This is what one expects: in the abelian U(1)+Higgs model there is no linear term [27], so that its coefficient should be proportional to the non-abelian gauge coupling.

## 5 The phase transition

Since we are mostly interested in the properties of the phase transition, most of our simulations are performed at and immediately around the transition temperature. We study three different Higgs mass parameters  $m_H^* = 35, 60$  and  $70$  GeV. We have mostly concentrated on  $60$  GeV Higgs, since it is close to the physically allowed mass range, but the transition is not yet too weakly first order to be studied with moderately sized lattices.

$m_H^*$	$\beta_G$	volumes							
35	8	$6^2 \times 18$		$8^2 \times 24_m$		$10^2 \times 30_m$		$12^2 \times 36_m$	
		$14^2 \times 42_m$		$8^2 \times 80_m$		$10^2 \times 80_m$			
	12	$12^3$		$16^3_m$		$12^2 \times 24_m$		$12^2 \times 48_m$	
		$16^2 \times 32_m$		$18^2 \times 36_m$		$20^2 \times 40_m$		$22^2 \times 44_m$	
	20	$10^3$		$10^2 \times 30$		$12^2 \times 36_m$			
		$16^2 \times 48_m$		$20^2 \times 60_m$		$24^2 \times 72_m$			
60	5	$12^2 \times 72_m$		$16^2 \times 80_m$					
		$12^3$		$16^3$		$24^3_m$		$32^3_m$	
	8	$20^2 \times 140_m$		$24^2 \times 120_m$		$30^2 \times 120_m$			
		$16^3$		$24^3_m$		$32^3_m$		$40^3_m$	
	12	$26^2 \times 156_m$		$30^2 \times 150_m$		$36^2 \times 144_m$			
		$16^3$		$24^3$		$32^3$		$40^3$	
	20	$40^2 \times 200_m$		$50^2 \times 200_m$					
70	8	$12^3$		$16^3$		$24^3$		$32^3$	
	12	$12^3$		$16^3$		$24^3$		$32^3$	
	20	$12^3$		$16^3$		$24^3$		$32^3$	

Table 3: Lattice sizes used for the simulations at the transition temperature for each  $(m_H^*, \beta_G)$ -pair. In most of the cases, several  $\beta_H$ -values were used around the transition point. Multicanonical simulations are marked by subscript ( $_m$ ).

For each of the three values of  $m_H^*$  we use the gauge couplings  $\beta_G = 8, 12$  and  $20$ , and for  $m_H^* = 60$  GeV also  $\beta_G = 5$  (remember that  $\beta_G$  is directly related to the



lattice spacing through  $\beta_G = 4/(g_3^2 a)$ . In table 3 we list the lattice sizes for each  $(m_H^*, \beta_G)$  -pair. Each lattice has several runs with different values for  $\beta_H$  in order to accurately locate the transition; typically smaller lattices have 5–20 and larger ones 1–3 values of  $\beta_H$ . Separate runs are then joined together with the Ferrenberg-Swendsen multihistogram method [28]. When the interface tension causes noticeable supercritical slowing down, the multicanonical algorithm is used. All in all, the total number of separate ‘runs’ — different combinations of lattice sizes and coupling constants — described in this paper is 289; this includes also runs away from the transition region.

The large number of lattice volumes with several lattice spacings makes it possible to accurately extract continuum values of the physical observables:

- (1) For fixed lattice spacing  $a$  (fixed  $\beta_G$ ), we extrapolate the lattice measurements to the thermodynamical limit  $V \rightarrow \infty$ .
- (2) Each of the  $V = \infty$  values are in turn extrapolated to the continuum limit  $a \rightarrow 0$  ( $\beta_G \rightarrow \infty$ ).

Note that in the 3d continuum theory the lowest-dimensional gauge-invariant operator  $\phi^\dagger \phi$  has the dimensionality GeV. This means that the scaling violations in physical quantities start from the first power of the lattice spacing  $a$  (in the 4d theory, scaling violations are proportional to  $a^2$ ).

The transition becomes weaker — the latent heat and the interface tension become smaller — when  $m_H^*$  increases. Measured in dimensionless lattice units, the transition also becomes weaker when the lattice spacing  $a$  decreases for fixed  $m_H^*$ . This can be observed from the probability distributions of the average Higgs field squared:  $R^2 = \frac{1}{V} \sum_x R(\mathbf{x})^2$ . In fig. 5 we show the distributions for some of the largest volumes for  $m_H^* = 60$  GeV,  $\beta_G = 5, 8, 12$  and 20. When  $\beta_G$  increases, the separation between the peaks becomes smaller and the minimum between the peaks becomes shallower. As we will explain in Secs. 5.2 and 5.3, these features are directly related to the latent heat and the interface tension, respectively.

In fig. 6 the corresponding  $\beta_G = 8$  histograms are shown for  $m_H^* = 35$  and 70 GeV. The dramatic effect of the Higgs mass to the strength of the phase transition is clearly evident. Note that all the distributions in figs. 5 and 6 correspond to different values of  $\beta_H$ ; each of the histograms has been reweighted to the ‘‘equal weight’’  $\beta_H$ -value (see Sec. 5.1).

## 5.1 The critical temperature

The critical temperature can be determined extremely accurately from the Monte Carlo data. In the SU(2)+Higgs model there are no known local order parameters, which would acquire a non-zero value only in one of the two phases of the model. Instead, we use order parameter like quantities which display a discontinuity at the transition

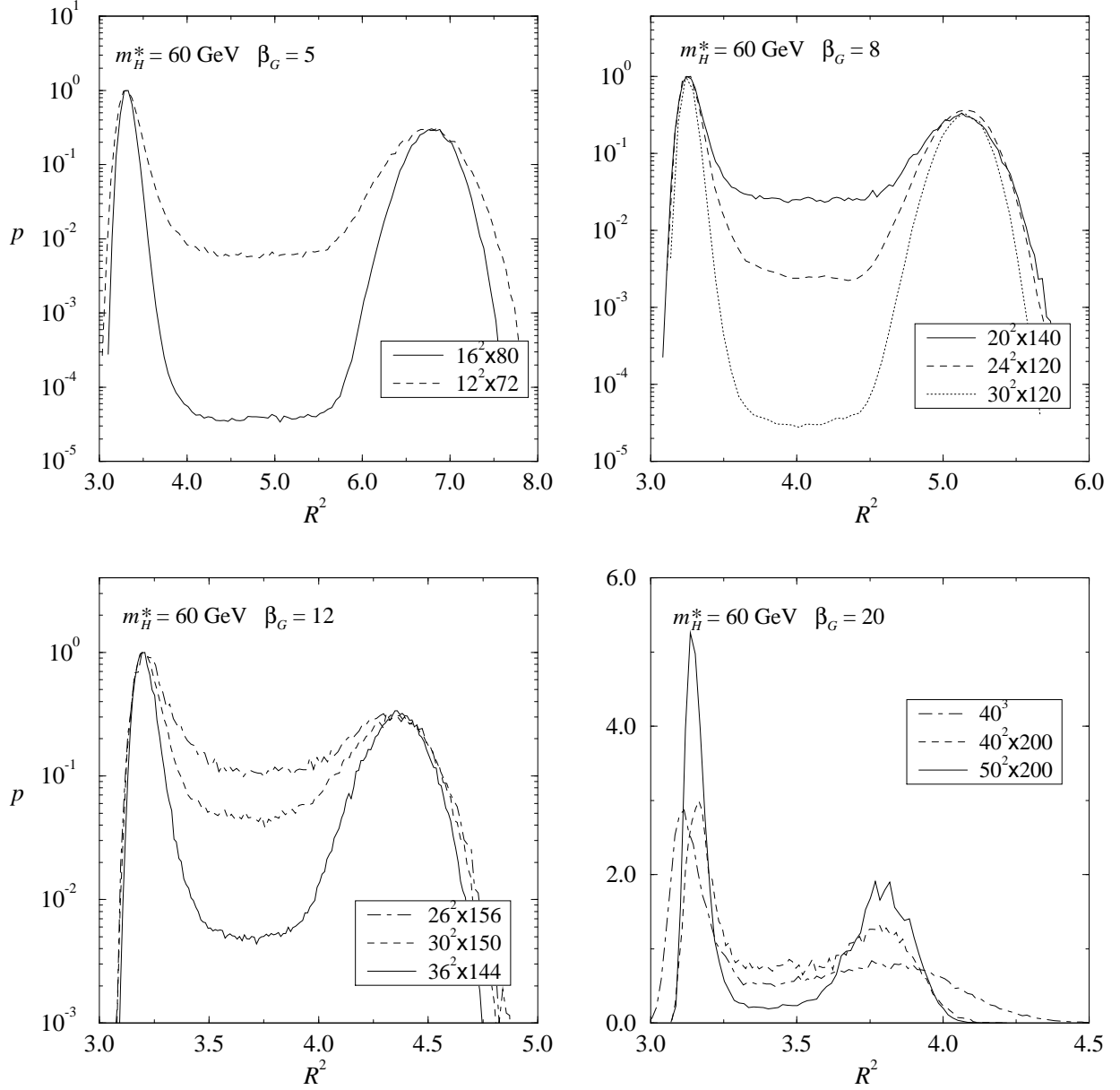


Figure 5: The probability distribution of the average Higgs length squared  $R^2$  for  $m_H^* = 60$  and  $\beta_G = 5, 8, 12$  and  $20$ .

point (when  $V \rightarrow \infty$ ). The quantities we use are  $R^2$  and the hopping term

$$L = \frac{1}{3V} \sum_{x,i} \frac{1}{2} \text{Tr} V^\dagger(\mathbf{x}) U_i(\mathbf{x}) V(\mathbf{x} + i) \quad (5.1)$$

where  $V(\mathbf{x})$  is the SU(2) direction of the Higgs variable  $\Phi(\mathbf{x}) = R(\mathbf{x})V(\mathbf{x})$ . The behaviour of  $\langle L \rangle$  as a function of  $\beta_H$  is shown in fig. 7 for  $m_H^* = 60$  GeV,  $\beta_G = 8$  case

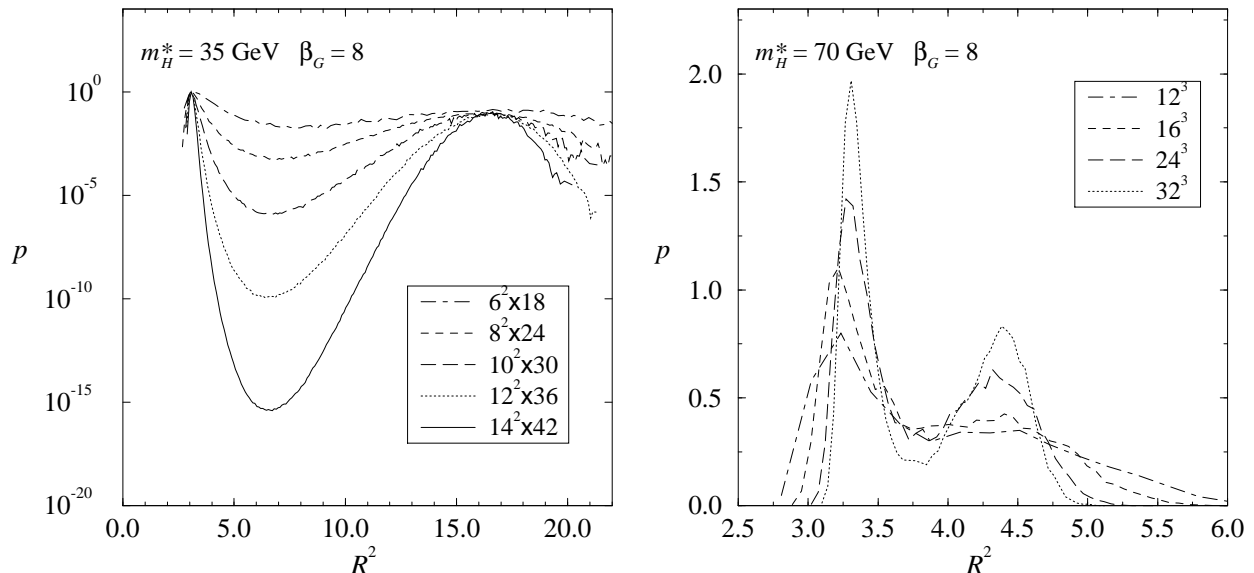


Figure 6:  $R^2$  distributions for  $\beta_G = 8$ ,  $m_H^* = 35$  and  $70$  GeV.

for lattice sizes up to  $32^3$ . The development of the discontinuity is clearly visible. The continuous lines are a result of the multihistogram method calculation.

For each individual lattice volume and  $(m_H^*, \beta_G)$ -pair, we locate the *pseudocritical coupling*  $\beta_{H,c}$  with several different methods (see, for example, [29] and references therein):

- (1) maximum of the  $L$ -susceptibility  $C(L) = \langle (L - \langle L \rangle)^2 \rangle$
- (2) maximum of  $C(R^2) = \langle (R^2 - \langle R^2 \rangle)^2 \rangle$
- (3) minimum of the 4th order Binder cumulant of  $L$ :  $B(L) = 1 - \langle L^4 \rangle / (3\langle L^2 \rangle^2)$
- (4) “equal weight”  $\beta_H$  -value of the distribution  $p(R^2)$
- (5) “equal height”  $\beta_H$  -value of the distribution  $p(L)$

The locations of the extrema of the observables  $C(L)$ ,  $C(R^2)$  and  $B(L)$  are computed by reweighting the original measurements; the error analysis is performed with the jackknife method, using independent reweighting for each of the jackknife blocks. As an example, we show  $C(R^2)$  and  $B(L)$  for  $m_H^* = 60$  GeV,  $\beta_G = 8$  lattices in fig. 8 as functions of  $\beta_H$ . For clarity, the errors are omitted from the figures. Again, we would like to point out the unambiguous first order scaling displayed by the data in these figures.

The  $\beta_H$ -values for the “equal weight” and the “equal height” distributions are also found by reweighting the histograms independently for each jackknife block. The histograms in figs. 5 and 6 are all equal weight  $R^2$  histograms; that is, the areas in the symmetric phase and broken phase peaks are equal. The calculation of the peak area

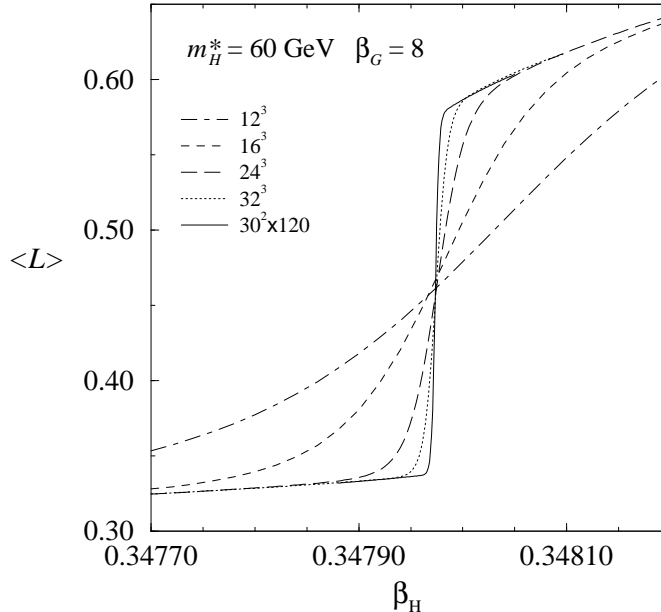


Figure 7: The hopping term  $\langle L \rangle$  as a function of  $\beta_H$  for different lattice sizes, for  $m_H^* = 60 \text{ GeV}$ ,  $\beta_G = 8$ .

requires an arbitrary selection of the value of  $R^2$  which is used to separate the peaks; we used a fixed value for all the lattices in each  $(m_H^*, \beta_G)$ -set, defined by the minimum of the distribution of the largest volume.

**The infinite volume limit:** The values of  $\beta_{H,c}$  determined with the methods (1)–(5) above differ for each individual lattice, but the  $V \rightarrow \infty$  extrapolations are very well compatible within the statistical errors. It should be noted that the different methods for determining  $\beta_{H,c}$  do *not* give statistically independent results, and it is not justified to combine the values given by different methods together. However, they serve the purpose of checking the consistency of the infinite volume and continuum limits.

In figs. 9–10 we show the infinite volume limits for  $m_H^* = 60 \text{ GeV}$  and  $\beta_G = 8$ , 12 and 20. As can be observed, different methods converge extremely well (the intercepts of the dashed lines at  $1/V = 0$  are nearly equal). The same holds true for Higgs masses  $m_H^* = 35$  and  $70 \text{ GeV}$ , which are not shown here. In table 4 we show the  $V \rightarrow \infty$  extrapolations of  $\beta_{H,c}$ , using the data obtained with the equal weight of  $p(R^2)$ -method. The corresponding values of the critical temperature  $T_c^*$ , calculated with eqs. (2.7), (2.10), are also shown.

**The continuum limit:** In fig. 11 the  $V = \infty$  values of  $T_c^*$  are extrapolated to the continuum limit  $a \rightarrow 0$  for  $m_H^* = 60 \text{ GeV}$ . We expect the leading deviation from the

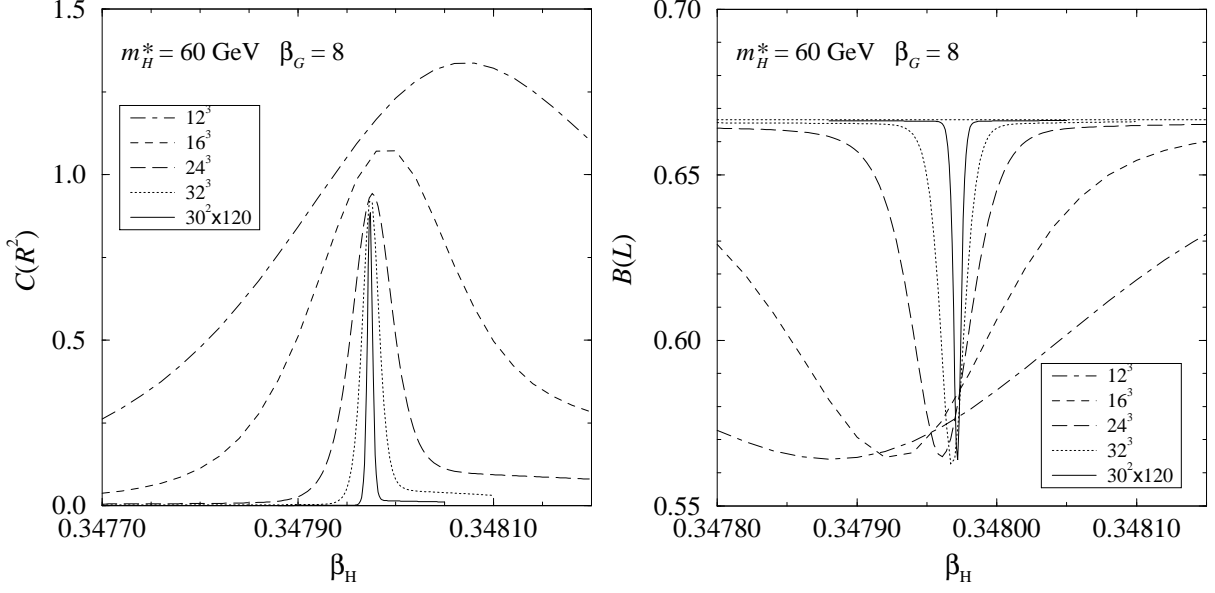


Figure 8:  $C(R^2)$ , the susceptibility of the order parameter  $R^2$  (top), and the Binder cumulant  $B(L)$  of the order parameter  $L$  (bottom), plotted as a function of  $\beta_H$  for  $m_H^* = 60$  GeV and  $\beta_G = 8$  runs.

$m_H^*/\text{GeV}$	$\beta_G$	$\beta_{H,c}$	$T_c^*/\text{GeV}$
35	8	0.3450806(17)	94.181(15)
	12	0.3411047(11)	93.666(23)
	20	0.3379421(28)	93.27(16)
60	5	0.358495(5)	137.534(17)
	8	0.3479735(6)	137.669(5)
	12	0.3426840(6)	137.842(12)
	20	0.3387418(4)	138.019(27)
70	8	0.3491523(39)	153.620(37)
	12	0.3433841(12)	153.930(26)
	20	0.3391279(26)	154.03(16)

Table 4: The infinite volume critical couplings  $\beta_{H,c}$ , and the critical temperatures  $T_c^*$ . The values of  $\beta_{H,c}$  are calculated from the “equal weight of  $p(R^2)$ ” data.

continuum limit value to be of order  $\mathcal{O}(a)$ ; in this case, there are 4 values for  $\beta_G$ , and the accuracy of the data is high enough that quadratic fits are needed in order to have good  $\chi^2/\text{d.o.f.}$  values for the fits. The quality of the fits is very good for the  $T_c^*$  values calculated with any of the five criteria, and the final extrapolations are statistically

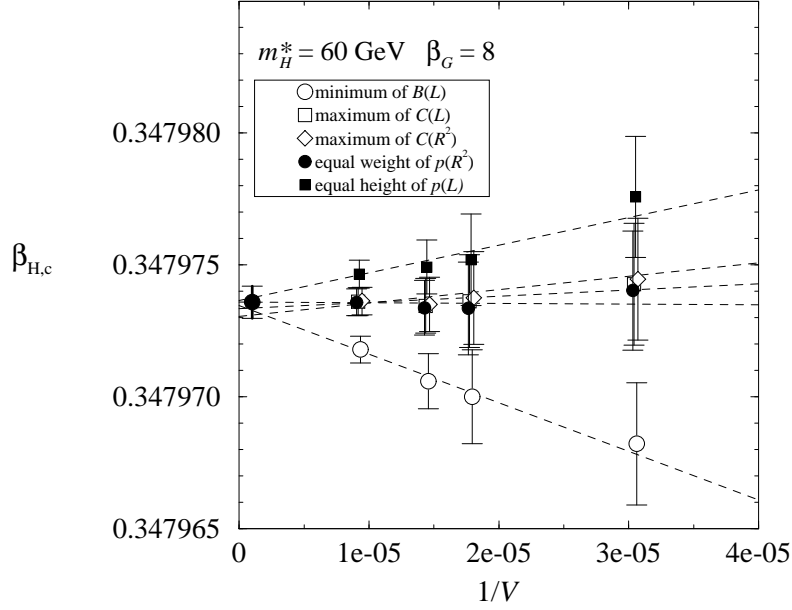


Figure 9: The  $V = \infty$  limit of the pseudocritical couplings  $\beta_{H,c}$  for  $m_H^* = 60$  GeV,  $\beta_G = 8$ , calculated with five different methods. All the methods give compatible  $V = \infty$  limits; the point near  $1/V = 0$  is the result from linear extrapolation of the “equal weight of  $p(R^2)$ ” -values. Only the largest volumes are shown.

compatible. For concreteness, we use the equal weight of  $p(R^2)$  -results for our final

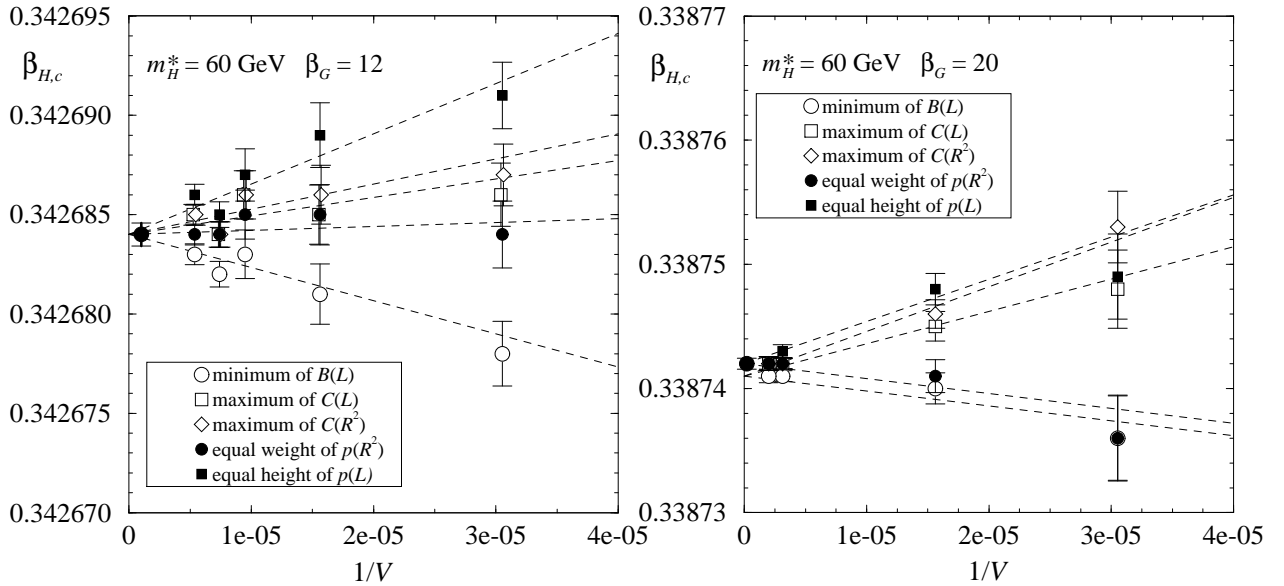


Figure 10: The same as fig. 9 for  $\beta_G = 12$  and  $\beta_G = 20$ .

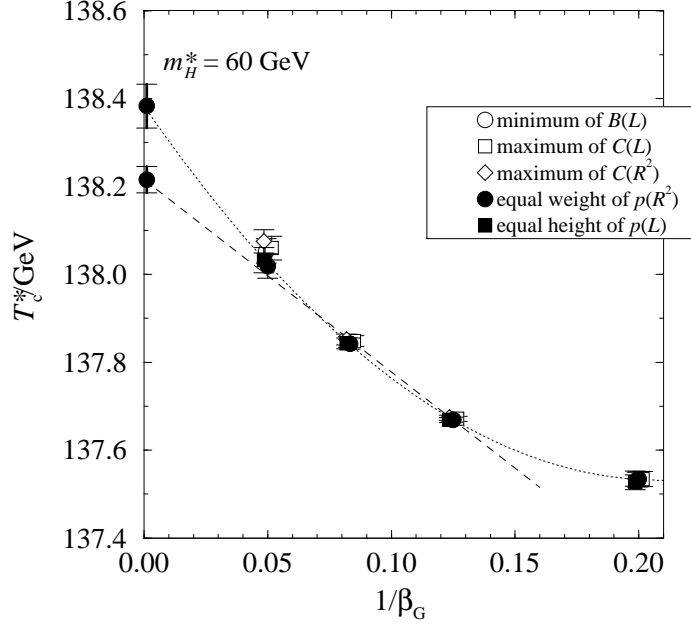


Figure 11: The continuum limit ( $\beta_G \rightarrow \infty$ ) of the critical temperature for  $m_H^* = 60$  GeV. A quadratic fit (dotted line) in  $1/\beta_G$  to all four  $\beta_G$ -values gives good  $\chi^2/\text{d.o.f.}$ , whereas a linear fit (dashed line) using only  $\beta_G \geq 8$  does not have acceptable  $\chi^2$ . The extrapolations shown are for “equal weight of  $p(R^2)$ ” data.

numbers.

In fig. 12 we show the corresponding extrapolations for  $m_H^* = 35$  and 70 GeV. In these cases we use linear fits. The final results are summarized in table 5, together with the perturbative values of  $T_c^*$ .

$m_H^*/\text{GeV}$	$T_c^*/\text{GeV}$	$T_c^{*\text{pert}}/\text{GeV}$
35	92.64(7)	93.3
60	138.38(5)	140.3
70	154.52(10)	157.2

Table 5: The continuum limit extrapolations of the critical temperatures. The  $m_H^* = 60$  GeV point has been calculated with a quadratic fit, others with linear fits.

There is a systematic difference between the perturbative and the lattice results; the perturbative  $T_c^*$  is considerably larger. The values are closest to each other when  $m_H^* = 35$  GeV, but for  $m_H^* = 60$  and 70 GeV the difference is more than 20 standard deviations. These results agree qualitatively with the results from the simulations with the  $A_0$  field [1, 3], but the errors here are almost an order of magnitude smaller.

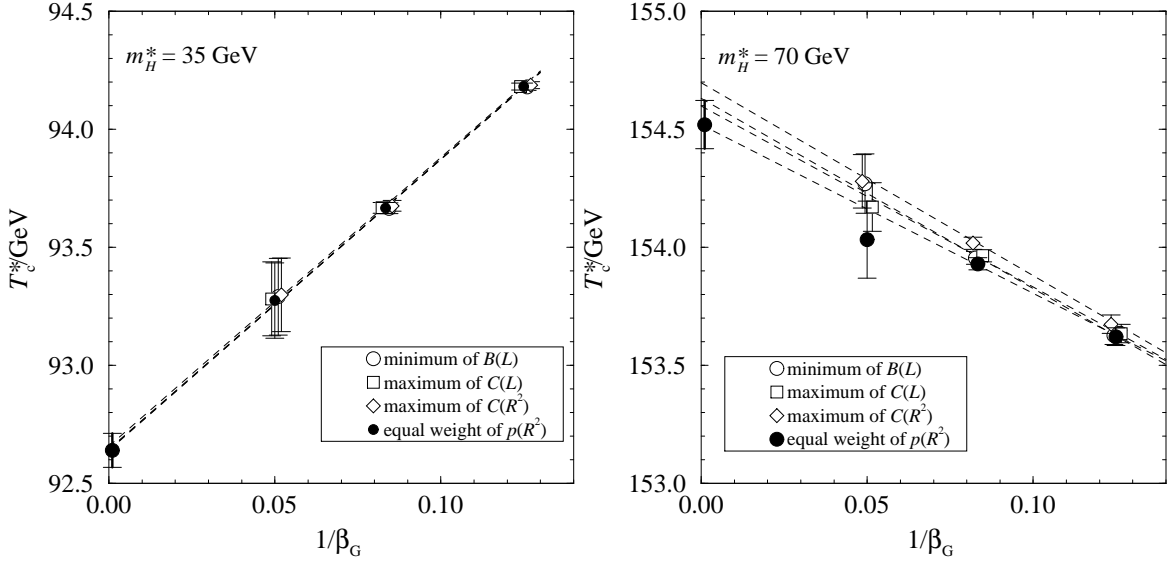


Figure 12: The same as fig. 11 for  $m_H^* = 35$  GeV and 70 GeV, using linear fits.

They also agree qualitatively with 4d simulations [21, 22] and recent 3d simulations by Ilgenfritz et al. [15]. Note, however, that in 4d case the errors are considerably larger, and in [15] the extrapolation to continuum limit is not taken.

## 5.2 The latent heat and $v(T_c^*)$

The latent heat  $L$  — the energy released in the transition — can be calculated from

$$\frac{L}{T} = \frac{d\Delta p}{dT} = \frac{T}{V} \frac{d}{dT} \Delta \log Z = \frac{T}{V} \frac{d}{dT} \Delta P, \quad (5.2)$$

where the derivatives are evaluated at the critical temperature,  $\Delta p$  is the difference of the pressures of the symmetric and broken phases, and  $\Delta P$  is the difference of the probabilities of the phases in volume  $V$ . In eq. (5.2),  $T$  is the physical (4d) temperature; for simplicity, in the following we substitute  $T \rightarrow T^*$ . In Sec. 11 we discuss how the correct physical result can be obtained. The quantity  $\Delta P$  is directly proportional to the difference of the areas of the two peaks in the order parameter distributions near  $T_c^*$ , and  $d(\Delta P)/dT^*$  is readily calculable by reweighting.

An alternative method is to evaluate  $d(\Delta p)/dT^*$  directly from the action in eq. (1.1):

$$\frac{L}{T_c^{*4}} = \frac{m_H^{*2}}{T_c^{*3}} \Delta \langle \phi^\dagger \phi \rangle = \frac{1}{8} \frac{m_H^{*2}}{T_c^{*3}} g_3^2 \beta_H \beta_G \Delta \langle R^2 \rangle. \quad (5.3)$$

Both methods give compatible results in the  $V \rightarrow \infty$  limit. The results shown here have been calculated with eq. (5.2).



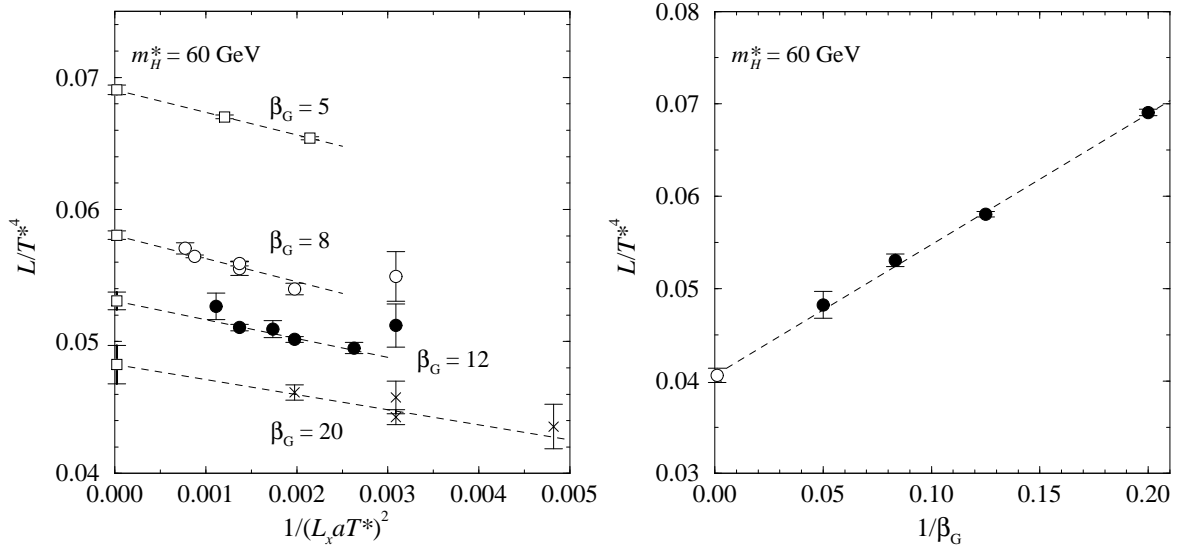


Figure 13: Extrapolation of the latent heat to  $V \rightarrow \infty$  limit (left figure) and to the continuum limit  $a \rightarrow 0$  (right figure) for  $m_H^* = 60$  GeV lattices.

Fig. 13 displays the limits  $V \rightarrow \infty$  and  $a \rightarrow 0$  for the latent heat for  $m_H^* = 60$  GeV systems. The infinite volume limit is taken by extrapolating linearly with respect to the inverse area  $1/(AT^{*2}) = (L_x a T^*)^{-2}$  of the system, where  $L_x a$  is the linear length of the lattice (one of the short dimensions for the cylindrical volumes). The extrapolation with respect to the inverse volume would fail to accommodate the cubical and cylindrical lattices simultaneously with the same scaling ansatz. The inverse area -type behaviour of the latent heat is known to occur for the Potts models in 2 dimensions [30, 31] (the area in this case being the linear dimension of the lattice).

The Higgs field expectation value in the broken phase  $v(T^*)$ , defined here by

$$\frac{v^2(T^*)}{T^{*2}} \equiv 2 \frac{\langle \phi^\dagger \phi(T^*) \rangle}{T^*}, \quad (5.4)$$

can be calculated from  $\langle R^2 \rangle$  using eq. (4.2). Because of the close relation between the equations (5.2) and (4.2), the limits are very similar in both cases. In fig. 14 we show the approach of  $v^2(T_c^*)$  to the continuum limit.

Higgs masses 35 and 70 GeV are analyzed in a similar way; the results for  $v(T_c^*)$  and the latent heat are shown in table 6.

Note that the values for both  $v$  and  $L$  are quite close to the perturbative values, *evaluated at the perturbative critical temperature*  $T_c^{*P}$ . If we use the lattice critical temperature  $v^P$  becomes larger, as can be seen from the last column in table 6. This shows the presence of higher-loop perturbative corrections in the broken phase, discussed in detail in the previous section.

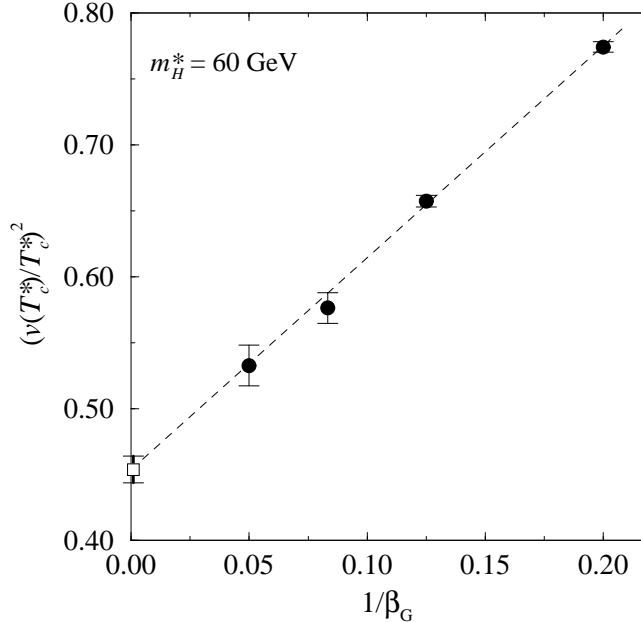


Figure 14: The continuum limit of the square of the Higgs field vev  $v^2(T_c^*)$ .

$m_H^*/\text{GeV}$	$L/(T_c^*)^4$	$L^P/(T_c^{*P})^4$	$v(T_c^*)/T_c^*$	$v^P(T_c^{*P})/T_c^{*P}$	$v^P(T_c^*)/T_c^*$
35	0.256(8)	0.22	1.86(3)	1.75	1.87
60	0.0406(7)	0.040	0.674(8)	0.68	0.82
70	0.0273(16)	0.027	0.57(2)	0.55	0.70

Table 6: The latent heat  $L$  and the Higgs field expectation value  $v(T_c^*)$  in the broken phase. Here  $T_c^{*P}$  is the perturbative critical temperature (see table 5). The comparison between lattice results and perturbation theory is discussed in Sec. 10.

### 5.3 The interface tension

The interface tension is one of the primary quantities which characterize the strength of the phase transition. We measure it with the *histogram method* [32]: at the pseudocritical temperature, a system in a finite volume predominantly resides in either the broken or the symmetric phase, but it can also exist in a mixed state consisting of domains of the two states. The probability of the mixed state is suppressed by the extra free energy associated with the interfaces between the phases. This causes the typical 2-peak structure of the probability distribution of the order parameter at the critical temperature (see figs. 5 and 6): the midpoint between the peaks corresponds to a state which consists of equal volumes of the symmetric and broken phases. Because of the associated extra free energy, the area of the interfaces tends to minimize. Assuming a lattice with periodic boundary conditions and geometry  $L_x^2 \times L_z$ , where  $L_x \leq L_z$ , the minimum area is  $2 \times A = 2(L_x a)^2$  — the number 2 appears because there are two

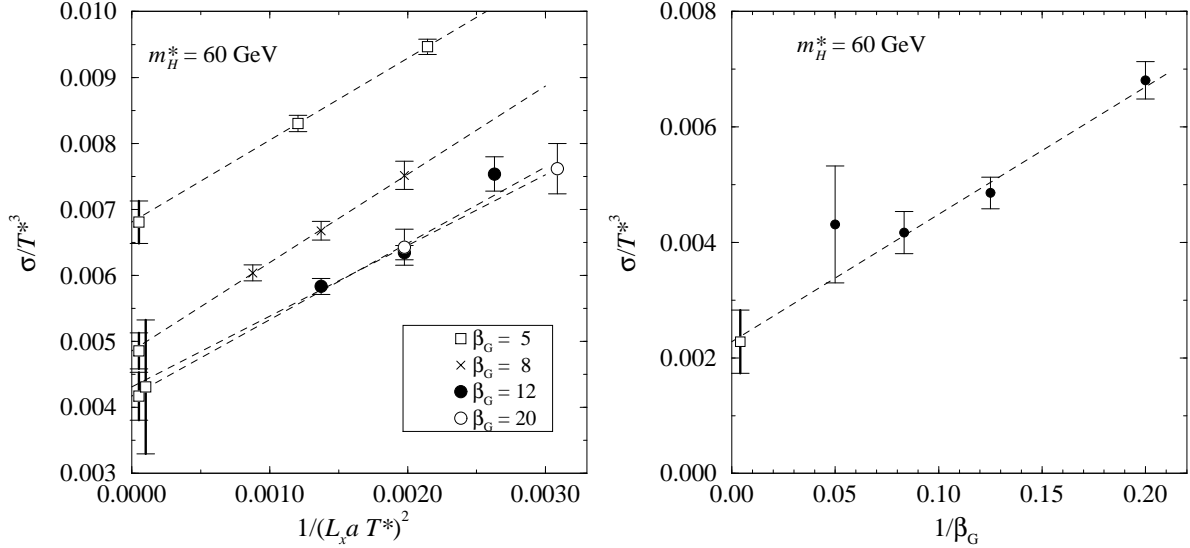


Figure 15: The interface tension for  $m_H^* = 60 \text{ GeV}$  extrapolated to  $V \rightarrow \infty$  (left) and  $a \rightarrow 0$  (right).

separate interfaces. The interface tension  $\sigma$  can be extracted from the limit

$$\frac{\sigma}{T} = \lim_{V \rightarrow \infty} \frac{1}{2A} \log \frac{P_{\max}}{P_{\min}}, \quad (5.5)$$

where  $P_{\max}$  and  $P_{\min}$  are the probability distribution maximum and the minimum between the peaks.

In practice, the infinite volume value of  $\sigma$  is reached in such large volumes that careful finite size analysis of eq. (5.5) is necessary. Numerous studies exist in the literature [33, 34, 35]; here we follow [35]:

$$\sigma \frac{a^2}{T} = \frac{1}{2L_x^2} \log \frac{P_{\max}}{P_{\min}} + \frac{1}{L_x^2} \left[ \frac{3}{4} \log L_z - \frac{1}{2} \log L_x + \frac{1}{2} G + \text{const.} \right]. \quad (5.6)$$

The function  $G$  interpolates between lattice geometries; the limiting values are  $G = \log 3$  for cubical volumes ( $L_z = L_x$ ) and  $G = 0$  for long cylinders ( $L_z \gg L_x$ ).

The finite size scaling ansatz (5.6) assumes that the two interfaces are far enough apart from each other that their mutual interaction is negligible. In practice, this is very difficult to achieve in cubical volumes and usually requires the use of long cylindrical lattices. The order parameter histograms develop a flat minimum when this condition is fulfilled: the flatness signals a constant free energy when the volume fractions of the two phases slightly change, and the interfaces move with respect to each other.

In order to find the flat part of the histograms we use large cylindrical volumes for all  $\beta_G$  values for  $m_H^* = 60 \text{ GeV}$ . The volumes included for the analysis are:  $\beta_G = 5$ :

$12^2 \times 72$  and  $16^2 \times 80$ ;  $\beta_G = 8$ :  $20^2 \times 140$ ,  $24^2 \times 120$ , and  $30^2 \times 120$ ;  $\beta_G = 12$ :  $26^2 \times 156$ ,  $30^2 \times 150$ , and  $36^2 \times 144$ ;  $\beta_G = 20$ :  $40^2 \times 200$  and  $50^2 \times 200$ . In fig. 5 we show the equal weight histograms of  $p(R^2)$  for these lattices.

In the interface tension analysis we use *equal height histograms of  $p(L)$* . Equal height histograms were chosen instead of equal weight because the determination of  $P_{\max}$  in equation 5.6 then becomes unambiguous; and  $p(L)$  instead of  $p(R^2)$  since the former histograms have more symmetric shapes than the latter, and the equal height and equal weight  $\beta_{H,c}$  values are quite close to each other. Nevertheless, we check the measurements with equal weight  $p(R^2)$  histograms (using  $P_{\max}$  which is a linear interpolation of the two peak heights to the  $R^2$  value of the minimum); the results are very well compatible within statistical errors.

A comment about extracting the extrema from the histograms is in order: we find the maximum values by fitting a parabola close around the peaks of the histograms, and the value of the flat minimum by fitting a constant. This method gives much smaller errors and more reliable results than simply using the absolute extrema values, which are very prone to statistical noise. The same method was used also to locate the equal height  $\beta_{H,c}$ -values.

In the left part of fig. 15 we show the interface tension measurements from each lattice. The values shown here include the finite size scaling correction  $1/L_x^2(\frac{3}{2} \log L_z - \frac{1}{2} \log L_x)$  from eq. (5.6), so that only a factor *const./ $L_x^2$*  remains. For each  $\beta_G$ , the behaviour of the data is linear in  $1/L_x^2$ . On the right part of fig. 15 we extrapolate  $\sigma$  to the continuum limit. The results are shown in table 7.

$m_H^*/\text{GeV}$	$\sigma/(T_c^*)^3$	$\sigma^p/(T_c^{*p})^3$
35	0.0917(25)	0.066
60	0.0023(5)	0.0078
70	—	0.0049

Table 7: The interface tension  $\sigma$ . Only the  $m_H^* = 60$  GeV result is an extrapolation to the continuum limit; the  $m_H^* = 35$  GeV value is only from  $\beta_G = 8$  simulations.

The  $m_H^* = 60$  GeV continuum limit result in table 7 is obtained by a linear extrapolation in  $1/\beta_G$ . However, on closer inspection the data from  $\beta_G = 12$  and 20 lattices on the left part of fig. 15 seem to indicate that the interface tension is already scaling when  $\beta_G \geq 12$ , even in finite volumes. If we use the finite volume  $\beta_G = 8$  and 12 data and extrapolate to infinite volume, we obtain the result  $\sigma/(T_c^*)^3 = 0.0042(3)$ , which is not compatible with the result in table 7. Nevertheless, since the data for the latent heat or  $v(T^*)$  do not display similar scaling behaviour, we use the linear extrapolation in  $1/\beta_G$  in all cases.

For  $m_H^* = 35$  GeV, only  $\beta_G = 8$  lattices are cylindrical enough so that we can estimate the  $V \rightarrow \infty$  limit. However, the continuum value can not be extrapolated.

For  $m_H^* = 70$  GeV we did not observe good enough flat parts in the order parameter histograms, and we do not attempt to estimate the interface tension.

## 6 The correlation lengths for $m_H^* = 60$ GeV

The measurement of the Higgs and  $W$  masses around the transition temperature is somewhat orthogonal to the measurements of the quantities directly associated with the transition itself: instead of attempting to enhance the tunnelling of the system from one phase to another, in this case it is imperative that the system stays in one homogenous phase throughout the measurement. This is due to the spurious signal caused by the *tunnelling correlations*:  $m_{\text{tunnel}} \propto \exp(-\sigma A/T)$  [29]. Even an incomplete tunnelling can make the extraction of the physical mass very complicated. Since the tunnellings are suppressed by the exponential factor  $\exp(-\sigma A/T)$ , we perform a separate set of simulations around the critical temperature using large volumes and monitor the simulation time history of order parameters in order to ensure that the system stays in a single phase throughout the measurement.

We perform the measurement only for  $m_H^* = 60$  GeV systems, using lattice sizes  $30^2 \times 60$  and  $40^2 \times 80$  for  $\beta_G = 8$  and  $40^2 \times 80$  and  $50^3$  for  $\beta_G = 12$ . Let us define operators

$$c_d^a(z) = \sum_{i=1,2} \sum_{\mathbf{x}} \delta_{x_3,z} \text{Tr} [\tau^a \Phi^\dagger(\mathbf{x}) U_i(\mathbf{x}) \dots U_i(\mathbf{x} + (d-1)\mathbf{e}_i) \Phi(\mathbf{x} + d\mathbf{e}_i)] \quad (6.1)$$

where  $a = 0, \dots, 3$ ;  $\tau^a$ ,  $a = 1, 2, 3$ , are the Pauli matrices and  $\tau^0 = \mathbf{1}$ ; and  $d = 0, \dots, 4$  is the length of the ‘chain’ of link matrices between  $\Phi^\dagger$  and  $\Phi$ . Using eq. (6.1) we can define correlation functions sensitive to the Higgs and  $W$  channels:

$$h_d(l) = \frac{1}{V} \sum_z c_d^0(z) c_d^0(z+l) \quad (6.2)$$

$$w_d(l) = \frac{1}{3V} \sum_z \sum_{a=1}^3 c_d^a(z) c_d^a(z+l). \quad (6.3)$$

The masses  $m_H(T^*)$  and  $m_W(T^*)$  are found from the exponential fall-off of  $h_d$  and  $w_d$ . The results are independent of the parameter  $d$ , and it is chosen to minimize the statistical errors. We obtain best results with  $d = 0$  for  $h_d$  ( $c_d^0 = \Phi^\dagger \Phi$ ) and  $d = 4$  for  $w_d$ .

The measured values of  $m_H(T^*)$  and  $m_W(T^*)$  are shown in fig. 16. The scaling between  $\beta_G = 8$  and 12 is very good, and both  $m_H$  and  $m_W$  display a discontinuity at the transition. At the transition temperature we are able to maintain the systems in either the broken or the symmetric phase throughout the measurement, so that immediately around  $T_c$  we have two values for the masses. Both  $m_H(T^*)$  and  $m_W(T^*)$  are *higher* in the symmetric phase than in the broken phase.

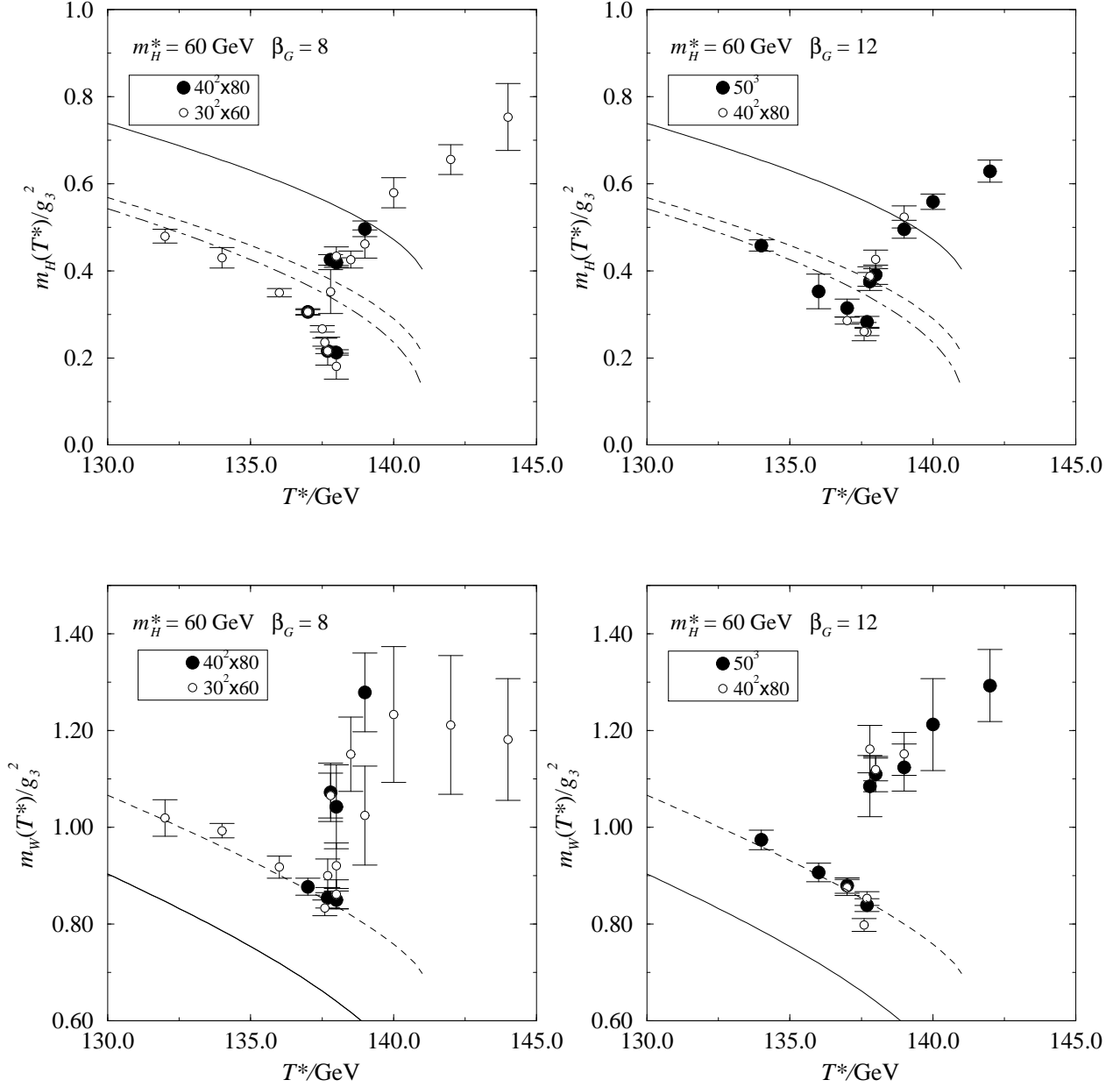


Figure 16: The Higgs masses (top) and the W masses (bottom) for  $m_H^* = 60 \text{ GeV}$ ,  $\beta_G = 8$  and 12 systems as functions of the temperature. The perturbative results are shown for  $m_H$  with solid (tree-level value), dashed (1-loop pole) and dot-dashed (some 2-loop corrections, see Sec. 10.1) lines; for  $m_W$  with solid (tree-level) and dashed (1-loop) lines. Note that the ratio  $m_W/m_H$  is much larger than indicated by the tree-level curves, since radiative corrections make  $m_W$  larger and  $m_H$  smaller.

## 7 The metastability ranges and scaling properties of the symmetric phase

An important characteristic of the phase transition is the range of metastability of the broken and symmetric phases. The symmetric phase is metastable below the critical temperature down to  $T = T_-$ , and the broken phase is metastable above the critical temperature up to  $T = T_+$ . The aim of the present section is to estimate the metastability range, and to study the dynamics of the composite field  $\langle\phi^\dagger\phi\rangle$  by determining its effective action. We shall concentrate on the case  $m_H^* = 60$  GeV ( $x=0.06444$ ) and  $T^*$  near  $T_c^*$  ( $|y - y_c| < 0.06$ ).

### 7.1 The metastability range from the correlation lengths

Consider the behaviour of the scalar mass near the phase transition, fig. 16. When the temperature decreases,  $m_H$  in the symmetric phase rapidly decreases. This behaviour suggests that it reaches zero at some point, and the symmetric correlation length diverges. This is the lower spinoidal decomposition point and corresponds to the temperature at which the symmetric phase ceases to be metastable,  $T_-$ . Similar behaviour takes place in the broken phase, when the temperature increases towards  $T_+$ . This observation allows us to estimate the metastability range, i.e., the upper and lower spinoidal decomposition temperatures. In general, one would expect the following dependence of the Higgs correlation lengths on the temperature:

$$\xi_H^i = c_i |T^*/T_i - 1|^{-\gamma_i}, \quad (7.1)$$

where  $i = b, s$  labels the broken and symmetric phases, and  $T_b \equiv T_+, T_s \equiv T_-$ . The data we have does not allow one to determine the critical exponents and the temperatures  $T_\pm$  simultaneously with good accuracy, so that we have chosen  $\gamma_i = 1/2$ , following the guidance from mean field theory. The results for the metastability region are given in table 8, using the  $m_H^* = 60$  GeV,  $\beta_G = 8$  and 12 results from fig. 16.

$\beta_G$	$T_-/\text{GeV}$	$c_s g_3^2$	$T_+/\text{GeV}$	$c_b g_3^2$
8	135.0(4)	0.35(2)	140.1(4)	0.49(2)
12	135.5(3)	0.33(2)	139.6(4)	0.45(2)

Table 8: The endpoints of the metastability temperature ranges for the symmetric ( $T_-$ ) and broken ( $T_+$ ) phases, determined from  $m_H^* = 60$  GeV Higgs correlations with the ansatz (7.1).

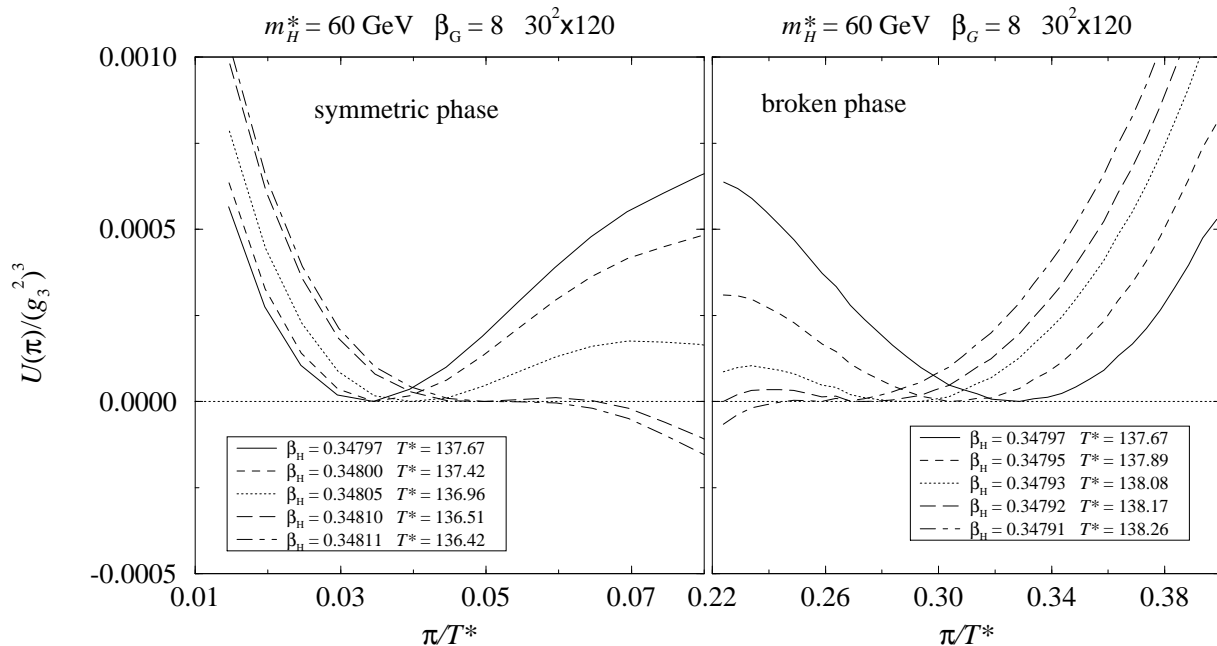


Figure 17: Evolution of the potential  $U(\pi)$  for the effective field  $\pi = \phi^\dagger \phi$ , related to the lattice variable  $R^2$  through relation (4.2), in the vicinity of the phase transition for  $m_H^* = 60$  GeV and  $\beta_G = 8$ . Different  $\beta_H$  values are reached by reweighting a single (multicanonical) simulation.

## 7.2 Metastability from reweighting

A direct method to measure the metastability range is to use the order parameter distributions and reweighting. Let us define an effective variable  $\pi \equiv \phi^\dagger \phi = \frac{\beta_H}{2a} R^2 + \text{const.}$ , where the last equality follows from eq. (4.2). Around the pure phase peaks, the probability distribution  $p(R^2)$  is related to an effective potential  $U(\pi)$ :

$$p(R^2) \propto e^{-VU(\pi)}, \quad (7.2)$$

where  $V$  is the volume of the system. Eq. (7.2) has pre-exponential corrections; however, to the accuracy we are working here the above formula is sufficient [36]. By reweighting the distribution  $p(R^2)$  we obtain the temperature dependence of the potential. It should be noted that eq. (7.2) is only valid in the immediate neighbourhood of the pure phases; it does not correctly describe the mixed state between the pure phases.

The endpoints of the metastability branches can be found by locating the temperature at which the barrier against the tunnelling vanishes — the minimum of the potential in eq. (7.2) turns into an inflection point. We present the evolution of the



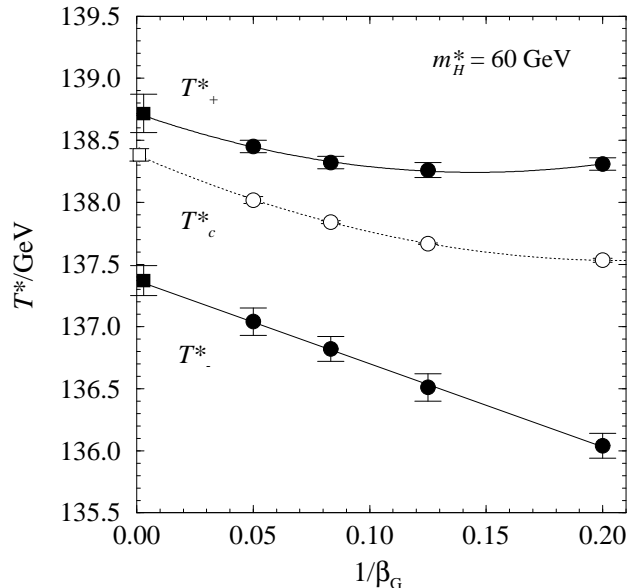


Figure 18: The metastability range for  $m_H^* = 60$  GeV Higgs systems, calculated with the reweighting analysis and extrapolated to  $a \rightarrow 0$ .

potential in fig. 17 for the symmetric and the Higgs phases for an  $m_H^* = 60$  GeV,  $\beta_G = 8$  system. These potentials are reweighted from the  $30^2 \times 120$  lattice histograms shown in fig. 5. In fig. 18 we extrapolate the temperatures  $T_-$  and  $T_+$  to the continuum limit, with the result

$$T_-^* = 137.37(12) \text{ GeV} \quad T_+^* = 138.72(15) \text{ GeV}. \quad (7.3)$$

The metastability range here is smaller than the range determined by fitting the correlation lengths (table 8). We believe that the values in eq. (7.3) are more reliable, because the power law extrapolation of the correlation lengths is very sensitive to statistical errors and finite volume effects. Note also that the range of  $\beta_H$  over which reweighting is carried out is very small.

### 7.3 The effective theory description

More information on the dynamics of the composite field  $\pi$  is contained in its effective action. We shall write it separately for each phase in the form

$$S_{\text{eff}} = \int d^3x \left[ \frac{1}{Z^2} \frac{1}{2} (\partial_i \pi)^2 + U(\pi) \right], \quad (7.4)$$

where near the minima corresponding to the two phases  $s, b$ :

$$U(\pi) = \frac{1}{2} v_2^2 (\pi - \pi_{\min})^2 + v_3 (\pi - \pi_{\min})^3 + v_4 (\pi - \pi_{\min})^4 + \dots \quad (7.5)$$

The quantities

$$\frac{\pi}{g_3^2}, \quad \frac{Z^2}{g_3^2}, \quad \frac{v_2^2}{g_3^2}, \quad v_3, \quad v_4 g_3^2 \quad (7.6)$$

are dimensionless functions of  $x, y$  and are different in the broken and symmetric phases.

Including only the quadratic terms the correlator is

$$\langle \pi(\mathbf{x})\pi(0) \rangle = \frac{Z^2}{4\pi|\mathbf{x}|} \exp(-Zv_2|\mathbf{x}|). \quad (7.7)$$

However, it is more convenient to define a plane-averaged field

$$\pi(z) = \int \frac{dx dy}{\text{Area}} \pi(x, y, z) \quad (7.8)$$

satisfying

$$\langle \pi(z)\pi(0) \rangle = \frac{1}{\text{Area}} \frac{Z}{2v_2} \exp(-Zv_2z). \quad (7.9)$$

Determining the exponential decay and the magnitude of plane-averaged correlator thus gives the parameters  $Z$  and  $v_2$  of the effective action.

By scaling  $\pi = (\beta_H/2a)R^2 + \text{const.}$ , these formulas can be directly rewritten for  $R^2$ . For a lattice with the geometry  $N^2 \times L$  the plane Higgs variable is defined as  $R_p^2(z) = [\sum_{x,y} R^2(x, y, z)]/N^2$ . At large distances the plane-plane correlator has the asymptotic form

$$\langle R_p^2(z)R_p^2(0) \rangle = AN^{-2}(e^{-zm_H} + e^{-(La-z)m_H}) + \text{const.}, \quad (7.10)$$

where  $m_H = 1/\xi_H$ . Using eq. (7.9) this determines the quadratic parameters of  $S_{\text{eff}}(\pi)$  as

$$m_H = Zv_2, \quad Z^2 = \frac{1}{2}A\beta_H^2 m_H. \quad (7.11)$$

For the potential we write

$$\begin{aligned} U(\pi)a^3 &= U\left(\frac{\beta_H}{2a}R^2 + \text{const.}\right)a^3 \\ &= V_2(R^2 - R_{\min}^2)^2 + V_3(R^2 - R_{\min}^2)^3 + V_4(R^2 - R_{\min}^2)^4 + \dots, \end{aligned} \quad (7.12)$$

where the couplings are related to the previous ones by

$$V_2 = \frac{1}{2} \frac{v_2^2}{g_3^2} \left(\frac{1}{2}\beta_H\right)^2 \times ag_3^2, \quad (7.13)$$

$$V_3 = v_3 \left(\frac{1}{2}\beta_H\right)^3,$$

$$V_4 = v_4 g_3^2 \left(\frac{1}{2}\beta_H\right)^4 \times \frac{1}{ag_3^2}. \quad (7.14)$$

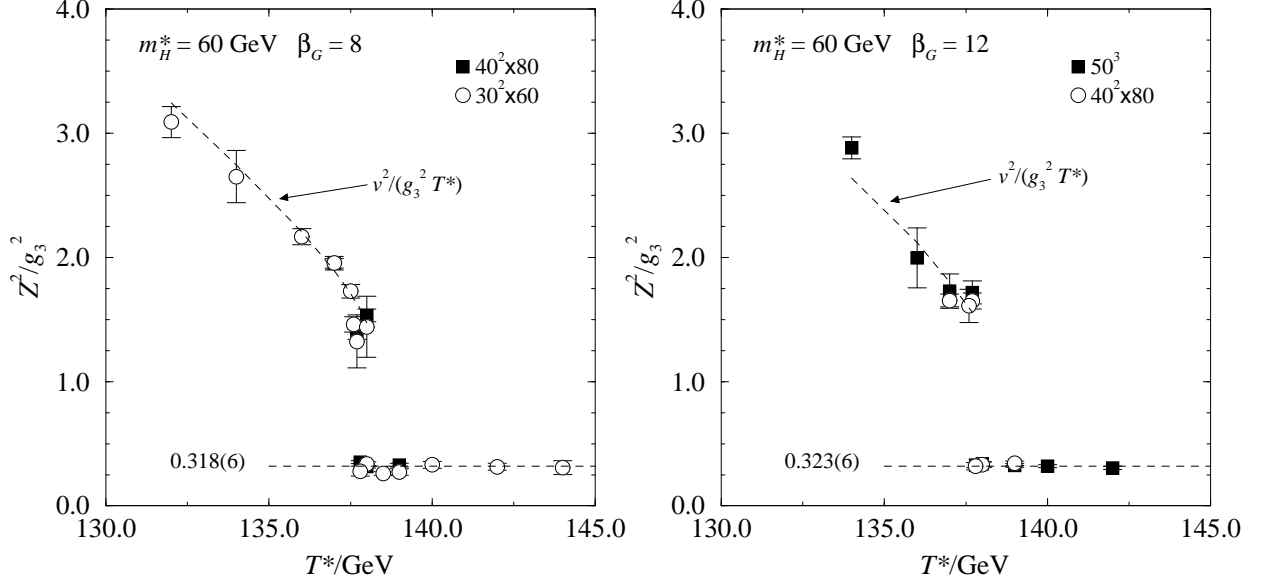


Figure 19: The wave function normalization of the scalar field near the phase transition for  $m_H^* = 60$  GeV and  $\beta_G = 8, 12$ . The horizontal lines are constant fits to the symmetric phase data. The dashed curves labeled  $v^2/g_3^2 T^*$  connect the MC datapoints for that quantity.

**The wave function normalization.** The lattice data for the quantity  $Z^2/g_3^2$  is shown in fig. 19 for  $m_H^* = 60$  GeV and for  $T$  near  $T_c^*$ . One can see that  $Z$  depends considerably on  $T$  in the broken phase, but is very accurately constant in the symmetric phase. The value of  $Z^2$  in the symmetric phase is

$$Z_s^2 = 0.320(5) g_3^2, \quad (7.15)$$

where the result is the average of the constant fits to the  $\beta_G = 8$  and 12 data. In the broken phase the behaviour of  $Z_b$  can be easily understood via the tree level relation

$$\frac{Z_b^2}{g_3^2} = \frac{v^2(T^*)}{g_3^2 T^*}. \quad (7.16)$$

The quantity  $v^2/(g_3^2 T^*)$  is also plotted in fig. 19, calculated from eq. (4.2). We can observe that the relation (7.16) is valid to good accuracy.

**The potential.** The potential part  $U(\pi)$  of the effective theory can be derived from the probability distribution  $p(R^2)$  using the relation (7.2) and by fitting the parameters  $R_{\min}^2$  and  $V_i$  in (7.12)<sup>8</sup>. Using again the  $m_H^* = 60$  GeV,  $\beta_G = 8$  data we are able to determine the three parameters  $R_{\min}^2$ ,  $V_2$  and  $V_3$ ; the statistical accuracy does not allow one to fix  $V_4$  with reasonable precision. The results of the fits are shown in fig. 20.

<sup>8</sup>This method is known as the constrained effective potential [36].

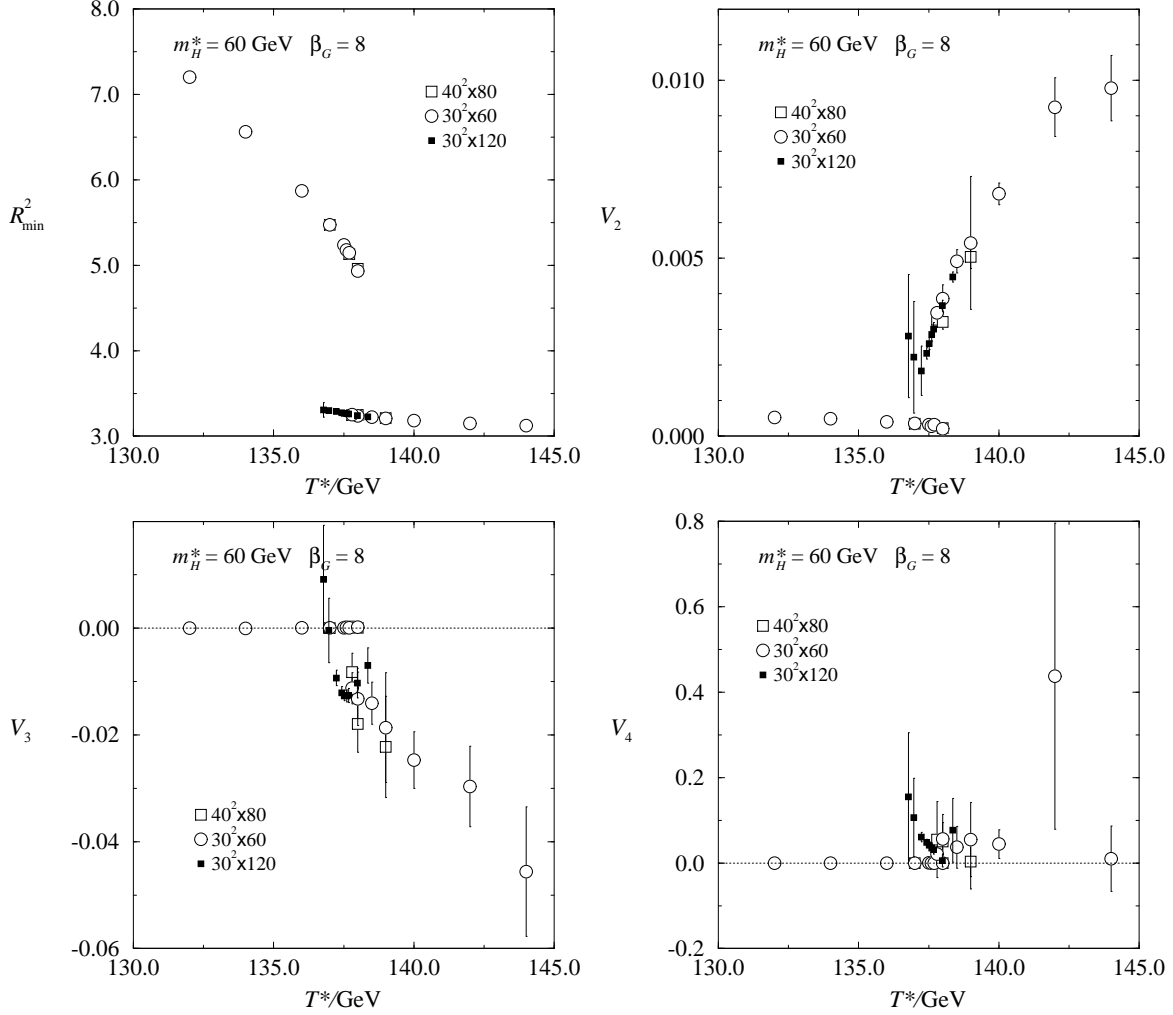


Figure 20: The lattice results for the effective potential coefficients, determined from  $m_H^* = 60$  GeV,  $\beta_G = 8$  systems.

There is an important consistency check for the validity of the effective theory description: using eqs. (7.11) and (7.13) the mass of the scalar particle is

$$m_H^2 = \frac{8V_2 Z^2}{a\beta_H^2}. \quad (7.17)$$

Substituting  $Z^2$  from (7.11) this becomes

$$4A(\xi_H/a)V_2 = 1. \quad (7.18)$$

Here  $\xi_H/a$  is the Higgs correlator in lattice units. Eq. (7.18) establishes a non-trivial connection between the different methods of mass determination. The first method is

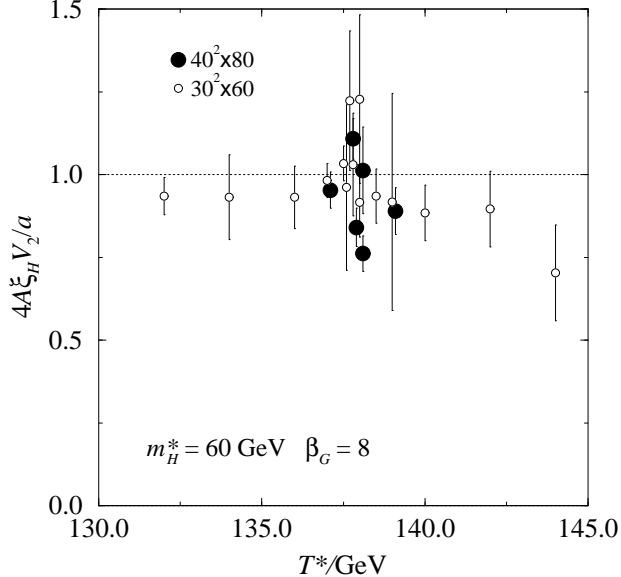


Figure 21: The lattice results for the test of the effective theory description.

the direct measurement via correlation functions and the second one is through the potential curvature. The lattice data for  $4A(\xi_H/a)V_2$  is presented in fig. 21. It is seen that the prediction of eq. (7.18) is satisfied reasonably well in both phases.

Let us turn now to the discussion of the behaviour of the coefficients  $V_2$  and  $V_3$ . When the temperature decreases (increases),  $V_2$  in the symmetric (broken) phase rapidly decreases, in fact repeating the behaviour of the scalar mass from the correlation function measurements. This gives another method for the metastability range determination. We write

$$V_2^i \propto |T - T_i|^{\gamma_i} \quad (7.19)$$

and fit  $T_i$  and  $\gamma_i$  separately for symmetric and broken phases. In the symmetric phase, the results are

$$\begin{aligned} \beta_G = 8 : T_- &= 137.0(5) \text{ GeV}, \quad \gamma_s = 0.51(14) \\ \beta_G = 12 : T_- &= 137.3(5) \text{ GeV}, \quad \gamma_s = 0.47(16). \end{aligned} \quad (7.20)$$

These values are quite consistent with the numbers in Sec. 7.2. However, in the broken phase we could not obtain acceptable fits.

It is interesting to note that the coefficient  $V_3$  has a strong dependence on temperature in the symmetric phase. This suggests that the effective potential  $U(\pi)$  has a scale-invariant form in the vicinity of the lower spinodal decomposition point. If we introduce the dimensionless variables

$$\tilde{\pi} = (\pi - \pi_{\min}) / (Z\sqrt{m_H}), \quad \tilde{x} = xm_H, \quad (7.21)$$

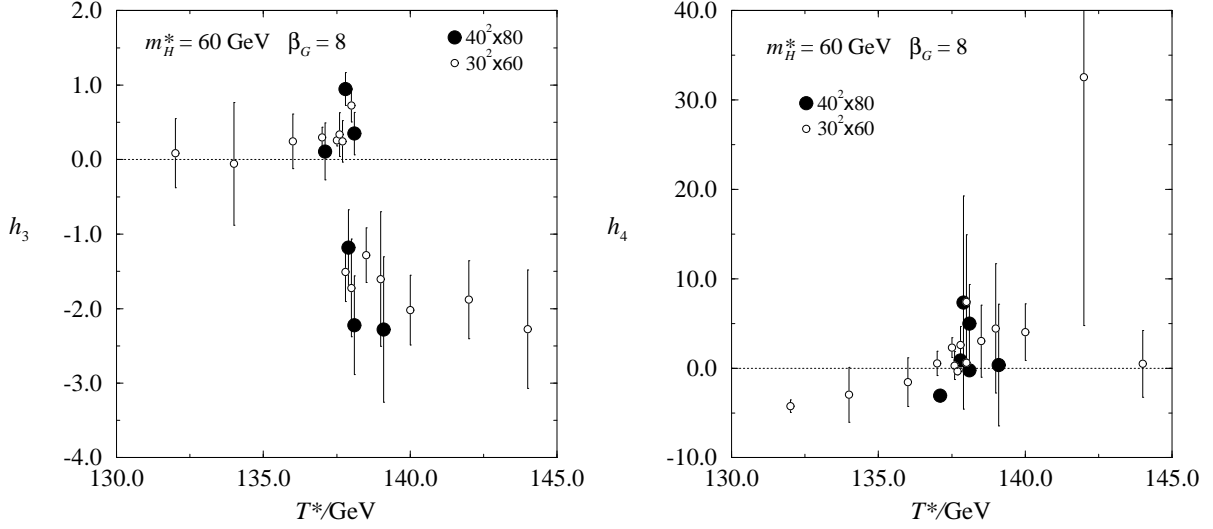


Figure 22: The temperature dependence of the effective coupling constants  $h_3$  and  $h_4$ .

then the action can be written in the form

$$S = \int d^3\tilde{x} \left[ \frac{1}{2}(\tilde{\partial}\tilde{\pi})^2 + \frac{1}{2}\tilde{\pi}^2 + h_3\tilde{\pi}^3 + h_4\tilde{\pi}^4 + \dots \right], \quad (7.22)$$

where the dimensionless couplings  $h_3$  and  $h_4$  are expressed via lattice observables as

$$h_3 = V_3(2A)^{3/2}, \quad h_4 = 16V_2V_4A^3. \quad (7.23)$$

Now, if  $h_3$  and  $h_4$  do not depend on the temperature, then the system has scale-invariant behaviour near the point of absolute metastability. The lattice data is shown in fig. 22. Indeed,  $h_3$  is reasonably temperature independent, while the quality of the data does not allow to make a definite conclusion on the higher interactions. The values of the coupling constants are completely different in distinct phases; they are larger in the symmetric phase, showing that interactions are strong there.

## 8 Simulations with $A_0$ field, $m_H^* = 80$ GeV

In [3] Monte Carlo studies of the  $m_H^* = 80$  GeV system, using a lattice action which includes the adjoint Higgs field  $A_0$ , were reported. The  $A_0$  field, a remnant of the timelike component of the gauge field, is a heavy field of mass  $\sim gT$ , and has been integrated out in the theory of eq. (1.1). The lattice action is

$$S = S[U, \Phi] + \frac{1}{2}\beta_G \sum_{x,i} [\text{Tr} A_0(\mathbf{x})U_i^\dagger(\mathbf{x})A_0(\mathbf{x}+i)U_i(\mathbf{x}) - \text{Tr} A_0^2(\mathbf{x})]$$

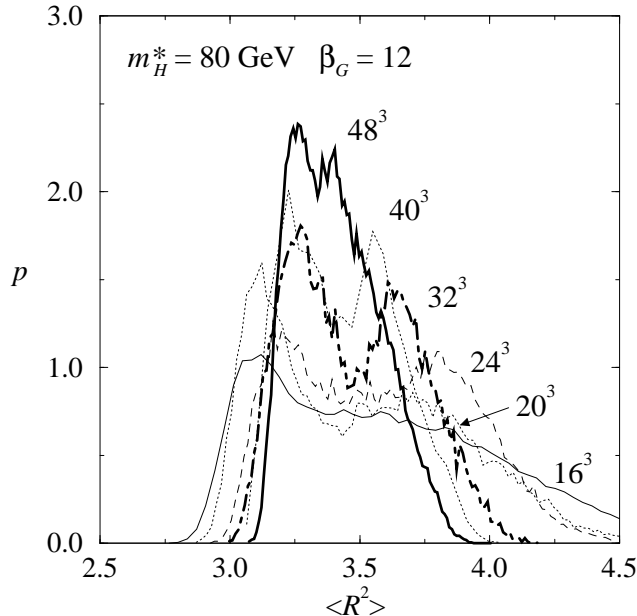


Figure 23: The  $p(R^2)$  distributions for  $m_H^* = 80$  GeV,  $\beta_G = 12$  lattices. The histograms are evaluated at  $\beta_H = 0.34771$ . The double-peak structure of the histograms becomes less pronounced when the volume becomes larger than  $32^3$ .

$$\begin{aligned}
& + \beta_2^A \sum_x \frac{1}{2} \text{Tr} A_0^2(\mathbf{x}) + \beta_4^A \sum_x \left[ \frac{1}{2} \text{Tr} A_0^2(\mathbf{x}) \right]^2 \\
& - \frac{1}{2} \beta_H \sum_x \left[ \frac{1}{2} \text{Tr} A_0^2(\mathbf{x}) \frac{1}{2} \text{Tr} \Phi^\dagger(\mathbf{x}) \Phi(\mathbf{x}) \right]
\end{aligned} \tag{8.1}$$

where  $S[U, \Phi]$  is the action given in eq. (2.4), and the lattice field  $A_0$  is given in terms of the continuum field  $A_0^a$  as  $A_0 = \frac{i}{2} g_3 a \tau_a A_0^a$ . The parameters  $\beta_2^A$  and  $\beta_4^A$  can be written in terms of the 4d continuum variables (see eqs. (II.15–19) and (II.97–99)).

In [3] lattices of sizes up to  $32^3$ , with  $\beta_G = 12$  and 20, were studied. Clear double-peak histograms were observed for both values of  $\beta_G$ , signaling a first order transition. However, since the publication of [3] we have performed simulations using lattice volumes up to  $48^3$ . Surprisingly, with increasing volume the double-peak feature of the histograms becomes *less* pronounced, in contrast to the expected behaviour in first order transitions (see fig. 23). The most striking finite volume effect is the shift of the peak positions towards each other when the volume is increased. Qualitatively similar finite volume behaviour occurs also in several other systems, which can exhibit either first or second order phase transitions in the infinite volume limit (for example, the 2-dimensional 7-state and 4-state Potts models, which have respectively first and second order transitions [30, 31]). Thus we cannot yet make definite conclusions about the order of the phase transition.

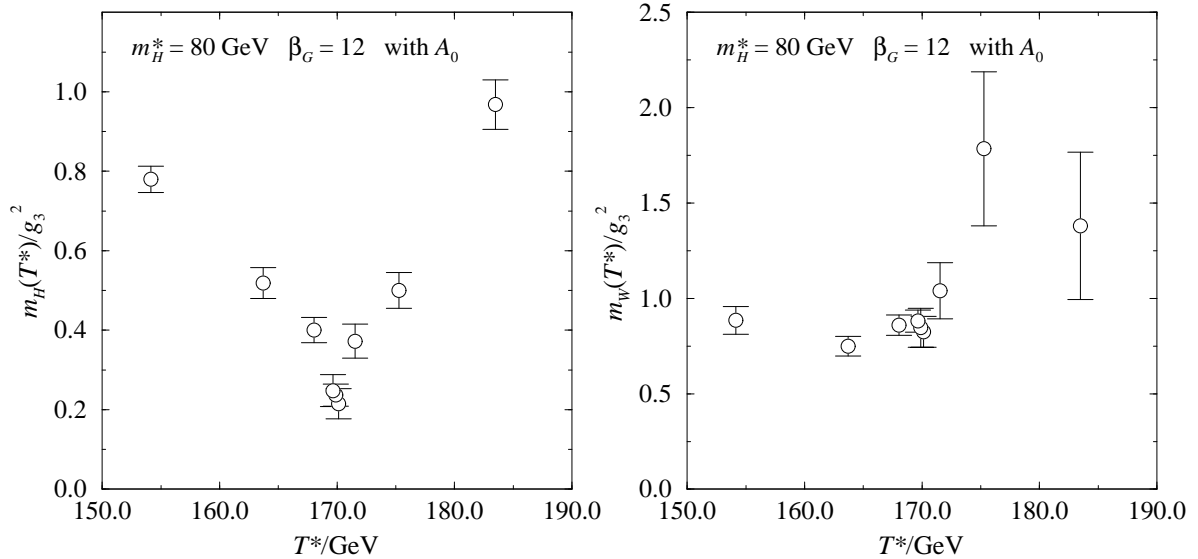


Figure 24: The Higgs and  $W$  masses of  $m_H^* = 80$  GeV,  $\beta_G = 12$ , and  $V = 40^3$  lattices around the transition temperature.

However, a note about the computer simulations is in order: the action (8.1) used in these simulations includes the  $A_0$  field, and because of the  $A_0$  hopping term in the action it is difficult to write an efficient overrelaxation algorithm. The algorithm we use here uses heat bath and Metropolis updates, and it performs more than an order of magnitude worse than the overrelaxation described in Sec. 3. Therefore, the statistical accuracy of the  $m_H^* = 80$  GeV results is not nearly comparable to the  $m_H^* \leq 70$  GeV results, described in Secs. 5–6. There are also more systematic uncertainties than in the simulations in Secs. 5–6, since the relations of lattice and  $\overline{\text{MS}}$  schemes were not fully known at the time of the  $m_H^* = 80$  GeV simulations.

In fig. 24 we show the Higgs and  $W$  masses around the transition temperature. To the accuracy of our data, we do not observe any discontinuities at the transition, as opposed to the  $m_H^* = 60$  GeV masses in fig. 16. However, the errors here are about a factor of 5 larger. In the immediate vicinity of the transition, the ratio of the  $W$  and Higgs masses is  $m_W/m_H \approx 4$ .

We measure the critical coupling  $\beta_{H,c}$  for each individual volume as described in Sec. 5. The infinite volume extrapolation is done using volumes larger than  $20^3$ , with the results  $\beta_{H,c} = 0.347715(8)$  for  $\beta_G = 12$ , and  $\beta_{H,c} = 0.341700(10)$  for  $\beta_G = 20$ . In contrast to simulations with  $m_H^* \leq 70$  GeV, in these simulations  $m_H^*$  was not kept constant, but instead the coupling constant  $\beta_R$  was fixed to values  $\beta_R = 0.00124$  and  $\beta_R = 0.000712$ , respectively. Using the relation  $m_H^{*2}/m_W^2 = 8\beta_R\beta_G/\beta_H^2$ , these correspond to  $m_H^* = 79.98$  and  $79.62$  GeV. The transition temperatures and the linear extrapolations to the continuum limit are given in table 9. The numbers are somewhat



different from those presented in [3]. The discrepancy is due to an error in the 2-loop term of the constant physics curve in [3].

$\beta_G$	$m_H^*/\text{GeV}$	$T_c^*/\text{GeV}$
12	79.976(1)	170.0(2)
20	79.614(2)	169.8(7)
$\infty$	79.072(6)	169.4(17)

Table 9: Results from  $m_H^* \approx 80$  GeV simulations, together with the extrapolations to the continuum limit. The perturbative critical temperature corresponding to  $m_H^* = 79.072$  GeV is about 171.5 GeV.

The continuum limit  $T_c^*$  is somewhat below the perturbative value; however, the statistical errors are too large for the difference to be significant. To resolve the situation at  $m_H^* = 80$  GeV requires simulations performed without the  $A_0$  field. Let us note that the value of  $x$  corresponding to  $m_H^* = 80$  GeV is  $x_c = 0.1188$ , and the physical Higgs mass in the Standard Model corresponding this  $x_c$  is about 81 GeV.

## 9 What happens at large Higgs masses

The phase transition in the 3d SU(2)+Higgs system becomes weaker and weaker with increasing scalar self-coupling  $x \sim m_H^{*2}$ . An important question is whether the transition for some value of  $x$  terminates in a 2nd order transition or whether it continues as a 1st order one for all  $x$ .

The main difficulty in resolving the order of the phase transition at large scalar self-coupling is the presence of the two distinct physical mass scales (inverse correlation lengths,  $m(T) = 1/\xi$ ). In fact, inspection of fig. 16 shows that for  $m_H^* = 60$  GeV near the transition point,

$$\frac{m_H(T)}{m_W(T)} \Big|_{\text{symmetric}} \approx \frac{m_H(T)}{m_W(T)} \Big|_{\text{broken}} \approx \frac{1}{3}. \quad (9.1)$$

Furthermore, fig. 24 indicates that this ratio is even smaller for larger  $m_H^*$ , and data for smaller  $m_H^*$  indicates that it is larger for them. Note also that vector masses do not seem to go to zero at the points of absolute metastability defined in Sec. 7.

Given the observed hierarchy  $\xi_H > \xi_W$ , the lattice spacing must be much smaller than the vector correlation length, while the lattice size must be much larger than the scalar correlation length. This puts stringent constraints on the lattice size and makes definite numerical conclusions more and more difficult with increasing  $m_H$  (see the discussion of the simulations with  $m_H^* = 80$  GeV in Sec. 8).

However, if the ratio  $m_H(T)/m_W(T)$  continues decreasing with increasing  $m_H$ , a solution to the problem immediately suggests itself: the vector degrees of freedom

become relatively heavy, decouple, and should be integrated out. From the effective 3d SU(2)+Higgs theory one thus at large  $m_H$  proceeds to an effective 3d scalar theory with just one degree of freedom. The transition to the scalar theory cannot be carried out by integrating out  $A_i$  perturbatively, and we first have to discuss the relevant degrees of freedom in more detail.

The 3d Euclidean SU(2)+Higgs theory originating from dimensional reduction corresponds to a (2+1)-dimensional Minkowskian SU(2)+Higgs theory. This theory has an analogy with QCD: we have doublets of scalar “quarks” bound together by an SU(2) triplet of “gluons”. We have chosen a Minkowskian language in order to keep the analogy with QCD transparent.

Then, one would expect that the lowest lying particle states in the symmetric phase are the spin zero scalar bound state and the three degenerate vector bound states, with quantum numbers corresponding to the composite operators

$$\pi = \phi^\dagger \phi, \quad (9.2)$$

$$W_j^0 = i(\phi^\dagger D_j \phi - (D_j \phi)^\dagger \phi), \quad W_j^+ = i(\phi^\dagger D_j \tilde{\phi} - (D_j \tilde{\phi})^\dagger \phi), \quad W_j^- = (W_j^+)^*, \quad (9.3)$$

correspondingly. Here  $\tilde{\phi} = i\tau_2 \phi^*$ . Note that these operators provide also a gauge-invariant description of the Higgs particle and intermediate vector bosons in the broken phase. In other words, the particle degrees of freedom are the same in both phases. This fact alone suggests that there is no distinction between the two phases, so that in some region in the parameter space [37, 38] there may be no phase transition at all. However, it does not exclude the situation that going from one phase to another is only possible through a phase transition.

The most general renormalizable local scalar field theory in 3d has the action

$$L = \frac{1}{2}(\partial_i \chi)^2 + P(\chi) \quad (9.4)$$

where  $P(\chi)$  is a sixth order polynomial which contains five constants (a linear term can always be removed by the shift of the scalar field)<sup>9</sup>:

$$P(\chi) = \sum_{i=2}^6 \frac{c_i}{i} \chi^i. \quad (9.5)$$

One of the constants (say,  $c_4$ ) fixes the scale, and the other four (say,  $c_2/c_4^2, c_3^2/c_4^3, c_5^2/c_4$  and  $c_6$ ) are dimensionless numbers completely fixing the dynamics of the theory. If the assumption on the effective theory is correct, then all the four parameters are some functions of the dimensionless ratios  $x$  and  $y$  characterizing the SU(2)+Higgs theory. In the vicinity of the phase transition, the first of the ratios ( $c_2/c_4^2$ ) is fixed, and there is a mapping of the three last ones to the single parameter  $x$  of the gauge-Higgs system

---

<sup>9</sup>Note that there is no symmetry (discrete or continuous) which forbids odd powers of  $\chi \sim Z^{-1}\pi$ .

at  $T = T_c$ . Clearly, these relations cannot be computed in perturbation theory, since at large  $m_H^*$  the phase transition occurs in the strong coupling regime. After they have been found by some nonperturbative means, resolving the order of the phase transition on the lattice at large  $m_H$  becomes a much easier task, because only one essential scale is present.

Finally, note that the action proposed here has a different number of degrees of freedom, different symmetries, and a different range of validity than the scalar action used in the simulations of [14].

## 10 What did we learn from the lattice simulations?

The non-perturbative information we acquired by doing lattice simulations can be confronted with different hypotheses on the nature of the phase transition existing in literature. It can be used as a test of validity of a number non-perturbative approaches, such as the  $\epsilon$ -expansion [39], the renormalization group approach [40], and the Dyson-Schwinger equations [42]. In this section we provide a summary of our findings and compare them with some of the mentioned approaches.

### 10.1 Comparison with perturbation theory

Perturbation theory can be used for the computation of different quantities in the broken phase. Not many quantities are known to high order in perturbation theory in the 3d SU(2)+Higgs theory, though. The whole list consists of the 2-loop effective potential for the scalar field in different gauges [2, 43, 44] (and the values of different condensates related to the effective potential, see [3]), and the 1-loop pole masses of the gauge and Higgs particles (see [42] and below).

**The effective potential.** If the temperature is fixed to some value, the vev of the Higgs field, defined by eq. (5.4), can be computed with the use of the 2-loop effective potential. At the same time, the “exact” vev of the Higgs field can be found on the lattice (after appropriate extrapolation to the continuum limit). The 2-loop effective potential gives a reasonably good prediction for  $v/T$ . For example,  $\delta v/v \sim 0.3\%$  for the vev of the Higgs field when  $v/T \simeq 2$ , and  $\delta v/v \sim 10\%$  for  $v/T \simeq 0.64$  (these numbers refer to  $m_H^* = 80$  GeV). Here  $\delta v = v_{2\text{-loop}} - v_{\text{exact}}$ . The exact vev is found to be *smaller* than that from 2-loop perturbation theory. This proves that the 3-loop linear correction to the effective potential comes with a positive sign. If the term in eq. (4.3) is added to the 2-loop effective potential with  $\beta = 50$ , then the agreement between the exact and 3-loop results is within 1% even for  $v/T$  as small as 0.6. In other words, the temperature dependence of the vev of the Higgs field can now be found *analytically* with 1% accuracy up to rather small values of  $v$ . This result is even more non-trivial than a direct analytical 3-loop computation of the effective potential, because it indicates that higher loop corrections are indeed small in this region of vevs.

The determination of 3-loop corrections to the effective potential allows one to get a better idea of the expansion parameter of the SU(2)+Higgs theory. As we have discussed in [2] it is difficult to get a reliable estimate of the expansion parameter for the effective potential on the basis of 2-loop perturbative computations. The expansion parameter (see Sec. 10.1) is proportional to  $g_3^2/(\pi m_T) = 2g_3/(\pi\phi)$ , but how big is the constant of proportionality? Indeed, the loop expansion may be reliable in the broken phase in spite of the fact that the 1-loop correction is comparable with the tree term, just because the scalar self-coupling constant is small. Moreover, the magnitude of the 2-loop correction may be changed by adjusting the scale  $\mu$ , so that the 2-loop correction may even be tuned to zero by some choice of  $\mu$ . Hence the determination of the 3-loop correction to the effective potential is important.

Let us take for definiteness  $m_H^* = 82$  GeV, i.e.,  $\lambda_3/g_3^2 = 1/8$  according to eq. (2.9). In addition, consider the region near  $T_c$  (take  $m_3^2 = 0$ ) and include only gauge field loops (neglect  $m_1$  and  $m_2$ ). Then the estimates of the different contributions to the effective potential are

$$\begin{aligned}
V_0 &= \frac{1}{32}g_3^2\phi^4, \\
V_1 &\simeq V_0 \times \frac{g_3^2}{\pi m_T(\phi)}, \\
V_2 &\simeq V_0 \times \frac{33}{32} \left[ \frac{g_3^2}{\pi m_T(\phi)} \right]^2 \log \frac{\mu}{\phi}, \\
V_3 &\simeq V_0 \times \frac{\beta}{32} \left[ \frac{g_3^2}{\pi m_T(\phi)} \right]^3,
\end{aligned} \tag{10.1}$$

where  $m_T(\phi) = g_3\phi/2$ . Inspection of these relations immediately shows that a reasonable estimate of the expansion parameter is  $\frac{g_3^2}{\pi m_T(\phi)}$ . This quantity is rather large ( $\sim 0.8$ ) in the vicinity of the phase transition for  $m_H^* = 70$  GeV, and the convergence of perturbation theory is expected to be quite bad. The main reason why the vev of the Higgs field can be found with a pretty high accuracy is that the effective potential is known up to a high order in perturbation theory.

**Perturbative correlators in the broken phase.** The next two quantities characterizing the broken phase are the vector and scalar correlation lengths.

As in Sec. 4, at a finite order in perturbation theory there are different methods of calculating the correlators. In principle, the most straightforward is a strict perturbative calculation in powers of  $\hbar$  in the loop expansion. Such a calculation can be done by shifting the Higgs field to the classical broken minimum where the Goldstone boson mass  $m_2$  vanishes, and by then calculating all the 1-loop diagrams, including the reducible tadpoles (the calculation in [42] is organized in this way). This method gives an explicitly gauge-independent results for the pole masses. Unfortunately, such a calculation gets increasingly unreliable as one approaches the phase transition, since

the tree-level results  $m_1$ ,  $m_T$  for the Higgs and W correlators, respectively, go to zero. The same problem was met in Sec. 4 in connection with the effective potential. One should therefore solve the relevant equations numerically, hoping that the higher-order corrections included are the essential ones. With this method, a small residual gauge- and  $\mu$ -dependence remains, and its magnitude can be used as an estimate of the consistency of the approximation. We find that the gauge-dependence of the final results for the correlators is numerically small, at most of the order  $0.03g_3^2$ . Below we give results in the Landau gauge. The  $\mu$ -dependence is also briefly discussed.

To calculate the correlators, we first solve for the radiatively corrected location of the broken minimum  $\phi_b$  from the RG-improved 2-loop effective potential  $V(\phi)$  [2]. The requirement of RG-improvement used here for the renormalization scale  $\mu(\phi)$  is that the 2-loop contribution to the derivative of the effective potential,  $\partial_\phi V_2(\phi, \mu)$ , vanishes. With  $\phi_b$  fixed, we calculate the inverse propagator, and solve numerically for the real part of the location of the pole. Since  $\phi_b$  is an approximation to the exact minimum of  $V(\phi)$ , no reducible tadpole diagrams are needed in the calculation of the propagator in contrast to the  $\hbar$ -calculation. The renormalization scale used in the calculation of the propagators is chosen to be  $\mu(\phi_b)$ . The dependence on  $\mu$  is formally of higher order than the accuracy of the 1-loop calculation, but is numerically visible, see below. The details of the calculation are in Appendix C.

The pole mass obtained from the correlator for the W particle is shown in fig. 16. In this figure we also show the tree-level value  $m_T$ . It is seen that in the broken phase, 1-loop perturbation theory gives excellent results. This is quite unexpected since the expansion parameter is rather large at the transition point. In fig. 16, we show also the pole mass of the Higgs particle, together with the tree-level value. There is also a third curve: from the known 2-loop contribution  $V_2(\phi)$  to the effective potential, one can derive the momentum-independent part of the 2-loop self-energy:  $\Pi_2^H(0) = -V_2''(\phi_b)$ . When this is added to the complete 1-loop result, one gets the dotted curve. It is seen that the discrepancy between lattice and perturbation theory is larger than for the W correlator. The effect of  $V_2''$  suggests that a complete 2-loop calculation of the Higgs self-energy might give a better estimate. The importance of 2-loop corrections for the Higgs particle is in accordance with experience from the effective potential, see [2]. Finally, let us point out that the tree- and 1-loop  $W$  masses, as well as the the Higgs mass with the 2-loop contribution included, are practically independent of  $\mu$ . For the tree- and 1-loop Higgs masses, the  $\mu$ -dependence in varying  $\mu$  in the range  $0.5\mu(\phi_b) \dots 2.0\mu(\phi_b)$  is of the order of  $0.03g_3^2$ .

Attempts to describe the correlation lengths in the symmetric phase can be found in [42, 45].

**Parameters of the phase transition** The characteristics of the phase transition, such as the critical temperature, latent heat, bubble nucleation rate, surface tension, and correlation lengths in the symmetric phase cannot be defined in the perturbative framework only, because the symmetric phase is in the strong coupling regime. The

failure of perturbation theory is clearly seen in order by order computations. For example, the vector 4-loop contribution has a logarithmic singularity at  $\phi = 0$ . Nevertheless, it is still interesting to compare 2-loop and 3-loop predictions with the results of lattice simulations. The RG-improved 2-loop effective potential is real in the vicinity of the critical temperature for the whole range of  $\phi$  and is regular at the origin. Hence, the computation of the above-mentioned characteristics of the phase transition is not faced with formal mathematical difficulties.

The critical temperature of the phase transition derived by 2-loop perturbation theory is presented in table 5. It is somewhat larger than that derived on the lattice. The vev of the scalar field at  $T_c^*$  for  $m_H^* = 60, 70$  GeV coincides with the lattice value within errorbars. This perfect agreement, however, is an incident, since the comparison of vevs is done at different temperatures. The same is true also for the latent heat, since it is mainly determined by the value of the scalar condensate in the broken phase. We do not expect the same coincidence at larger Higgs masses.

One of the crucial quantities for the computation of the bubble nucleation rate is the surface tension. For  $m_H^* = 60$  GeV, its value on the lattice is considerably (about 3 times) smaller than that derived from perturbation theory as

$$\sigma = \int_0^{\phi_b(T_c)} \sqrt{2V(\phi)} d\phi. \quad (10.2)$$

Note that this equation is valid to leading order only; in higher orders the wave function renormalization must be taken into account. However, the huge discrepancy with the lattice result shows that perturbation theory is not applicable at all for the computation of the surface tension, at least for  $m_H^* \gtrsim 60$  GeV.

To summarize, the computation of the characteristics of the phase transition from 2-loop perturbation theory (for  $35 \text{ GeV} < m_H^* < 70 \text{ GeV}$ ) is accurate for the critical temperature within  $0.8 - 1.6\%$  and for the ratio  $v/T$  within  $6\%$ . Perturbation theory fails to describe the surface tension (and, therefore, the bubble nucleation rate) at least for  $m_H^* = 60$  GeV.

Adding to the effective potential the 3-loop linear term determined in Sec. 4 does not improve the accuracy of perturbative predictions. We take as an example  $m_H^* = 60$  GeV and  $\beta = 50$ , as follows from lattice simulations. The critical temperature remains roughly as far from the lattice  $T_c^*$  as at 2-loop level, being now *smaller* than the lattice value,  $T_c^{3\text{-loop}} = 136.8$  GeV. The 3-loop ratio  $v^{3\text{-loop}}(T_c^{3\text{-loop}})/T_c^{3\text{-loop}}$  is about  $20\%$  larger than the exact value<sup>10</sup>. The 3-loop perturbative latent heat is away from the lattice results by almost  $50\%$ . The most drastic deviation is in the surface tension. The 3-loop value of it is  $\sigma/(T_c^*)^3 \simeq 0.018$  - a factor 7 larger than the lattice number! The behaviour of the effective potential in two different situations is illustrated in

---

<sup>10</sup>The estimate of  $v/T$  in the broken phase at a *given* temperature of course does improve, since the 3-loop part is determined by just this requirement. The discrepancy is due to the fact that the exact and 3-loop critical temperatures are different, and  $v/T$  is strongly temperature dependent near  $T_c$ .

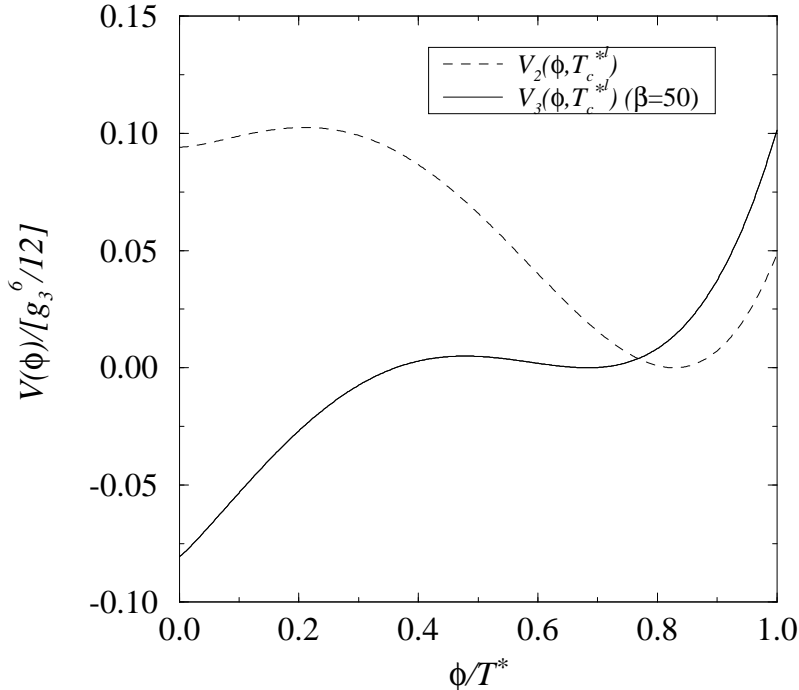


Figure 25: The RG-improved 2-loop effective potential (dashed line) and the 3-loop effective potential with  $\beta = 50$  (solid line) for  $m_H^* = 60$  GeV at the non-perturbative critical temperature  $T_c^* = 138.38$  GeV. Note that in this figure we have expressed  $\phi$  in 4d units [ $\phi_{4d} = \phi_{3d}(T^*)^{1/2}$ ].

figs. 25, 26. It is clearly seen that perturbation theory cannot quantitatively describe the phase transition.

## 10.2 Comparison with other non-perturbative approaches

We were not able to make a detailed comparison of the results of lattice simulations with all the non-perturbative approaches suggested in literature. For example, in [39] devoted to the application of the  $\epsilon$ -expansion, the authors compare their results to 1-loop effective potential predictions. As we argued in [2], 1-loop computations in 3d have a considerable unphysical scale dependence, and this fact makes a direct comparison difficult. We could not make a comparison with the renormalization group approach in [40], either, nor with [45]. Hence we discuss here [41] and [42, 46, 47].

In [41] it was suggested that the non-perturbative effects may considerably modify the effective potential of the Higgs field near the origin. Assuming that perturbation theory works in the broken phase, a measure of the non-perturbative energy shift at  $\phi = 0$  was introduced,

$$A_F = \frac{12}{g_3^6} [V(0, T_c^*) - V(\phi_b, T_c^*)]. \quad (10.3)$$

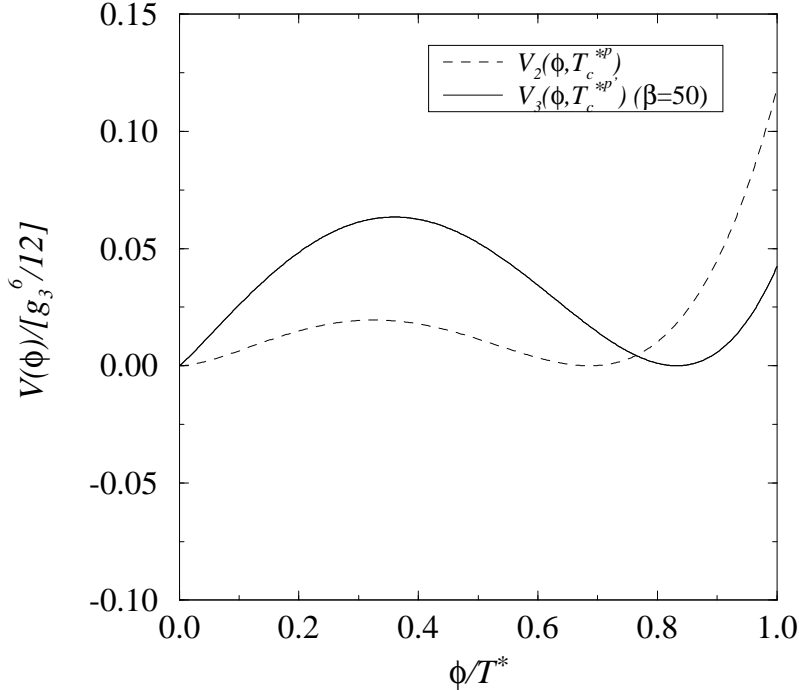


Figure 26: The 2-loop and 3-loop effective potentials at the corresponding perturbative critical temperatures,  $T_c^{*p} = 140.25$  GeV and  $136.82$  GeV, respectively.

Here  $T_c^*$  is the exact value of the critical temperature. It was conjectured in [41] that if  $A_F$  is positive then the phase transition is stronger than predicted by perturbation theory. In particular, if  $A_F$  is sufficiently large (say,  $A_F = 0.4$ ), then the lower metastability temperature is considerably smaller than the critical temperature, and the vev of the Higgs field at  $T_-$  is substantially larger than it is at the critical temperature. The lattice simulations allow to check the validity of this hypothesis. Let us take for definiteness  $m_H^* = 60$  GeV. Then,  $A_F$  is to be found from 3-loop perturbation theory (2-loop perturbation theory gives a result off by 20% for the vev of the Higgs field and therefore is not to be used). We get  $A_F \simeq -0.08$ , see fig. 25<sup>11</sup>. In other words, the phase transition is weaker than predicted by 3-loop perturbation theory. Hence the assumption of the dominance of the gluonic condensate contribution to the vacuum energy in the symmetric phase, used in [41], appears not to be satisfied .

In [42] it was suggested that a reasonable description of the symmetric phase can be achieved with the 1-loop Schwinger-Dyson equation. From the analysis of this equation it was anticipated that the symmetric phase can be interpreted as a Higgs phase whose parameters are determined non-perturbatively. One of the predictions of this approach

<sup>11</sup>In [3] we had another estimate of the parameter  $A_F$ ,  $A_F = 0.2$ . The difference is because in [3] 2-loop perturbation theory was used, the 2-loop relations of the lattice and  $\overline{\text{MS}}$  schemes were not fully available, and the proper extrapolation of the lattice results to the continuum limit was not done due to the limited amount of data.



is that the vector boson mass in the symmetric phase is smaller than  $0.27g_3^2$ , what is to be confronted with the lattice value  $m_W \sim 1.1g_3^2$ . We believe that the main reason why this approach does not work is because it relies on an accurate description of the symmetric phase by 1-loop perturbation theory. In particular, it was estimated in [42] that the expansion parameter in the 3d theory is  $\frac{1}{6\pi} \frac{g_3^2}{m_T}$ , while we find it to be about 6 times larger.

In [46, 47] it was suggested that the introduction of a “magnetic mass”  $m_M \sim g_3^2/3\pi$  in the propagator of the gauge boson will cure the infrared problem and allow one to estimate the magnitude of non-perturbative effects. This recipe would effectively produce a linear 3-loop term with a negative coefficient:

$$V_1(\phi) \sim -\frac{1}{2\pi}(m_M^2 + m_T^2)^{3/2} = -\frac{1}{2\pi}\left(m_T^3 + \frac{3}{4}g_3\phi m_M^2 + \dots\right), \quad (10.4)$$

where  $m_T = g_3\phi/2$ . This is clearly in contradiction to the existence of the positive linear term we found in the simulations.

## 11 Results for different physical 4d theories

So far we have given results for the characteristics of the phase transition in the SU(2)+Higgs model using the simplified relations of 4d and 3d parameters given in eqs. (2.8)-(2.10). Here we explain how these results can be converted into characteristics of finite-temperature phase transitions in physical theories where the relations between 4d and 3d are more complicated. We also give explicit results for the phase transition in the 4d SU(2)+Higgs theory without fermions, in the 4d SU(2)+Higgs theory with the fermionic content of the Standard Model, and in the Standard Model.

To begin with, let us restate the observables relevant for the phase transition in terms of properties of the 3d theory alone. The parameters of the 3d theory are  $g_3^2, x, y$ , defined in eqs. (2.8)–(2.10). From lattice measurements, one can derive the expectation value of dimensionless gauge-invariant observables, like  $\langle\phi^\dagger\phi(g_3^2)\rangle/g_3^2$  (one must use eq. (4.2) to change scheme from lattice to  $\overline{\text{MS}}$  at  $\mu = g_3^2$ ). Let us denote this particular expectation value by  $\ell_3$ ,  $\ell_3 \equiv \langle\phi^\dagger\phi(g_3^2)\rangle/g_3^2$ . Let  $\ell_3^b$  be the value of  $\ell_3$  in the broken phase at the critical point  $(x_c, y_c)$ , and  $\Delta\ell_3$  be the difference of the values of  $\ell_3$  in the broken and symmetric phases at the critical point,  $\Delta\ell_3 = \ell_3^b - \ell_3^s$ . The critical point  $(x_c, y_c)$  is determined as explained in Sec. 5.1. The observable  $\Delta\ell_3$  is related to the dimensionless quantity  $\epsilon_3(x, y)$  defined by

$$\exp[-V_3g_3^6\epsilon_3(x, y)] = \int \mathcal{D}\phi\mathcal{D}A \exp(-S[\phi, A]), \quad (11.1)$$

through

$$\frac{\partial\Delta\epsilon_3(x_c, y_c)}{\partial y_c} = \Delta\ell_3 \quad (11.2)$$

where  $\Delta\epsilon_3(x, y) = \epsilon_3^b(x, y) - \epsilon_3^s(x, y)$  and  $V_3$  is the volume of the system. Finally, we define the dimensionless quantity  $\sigma_3$  related to the surface tension by

$$\sigma_3 = \lim_{V \rightarrow \infty} \frac{1}{2g_3^4 A} \ln \frac{P_{\max}}{P_{\min}}, \quad (11.3)$$

in analogy with eq. (5.5). The observables  $x_c, y_c, \ell_3^b, \Delta\ell_3$  and  $\sigma_3$  are all dimensionless quantities defined strictly inside the 3d theory, are independent of the parametrization used in eqs. (2.8)-(2.10), and are measurable, in principle, to arbitrary accuracy with lattice simulations, since the lattice counterterms of the 3d theory are known exactly.

Next, one needs the relations to 4d. The relations to 4d consist of two parts:

(a) One needs the expressions of the parameters  $g_3^2, x$  and  $y$  of the 3d theory in terms of temperature and the physical parameters of the 4d theory. For definiteness, let us take as one of the physical parameters the pole mass of the Higgs field,  $m_H$ . Then the parameters of the 3d theory are of the form  $g_3^2 = g_3^2(m_H, T)$ ,  $x = x(m_H, T)$  and  $y = y(m_H, T)$ .

(b) One needs the relation of 3d observables to 4d thermodynamics. This relation is completely determined by the equation  $p(T) = -Tg_3^6\epsilon_3(x, y)$ , which holds apart from inessential mass-independent terms.

Using the relations in (a) and (b), one can relate  $x_c, y_c, \ell_3^b, \Delta\ell_3$  and  $\sigma_3$  to 4d quantities characterizing the thermodynamics of the phase transition. First, from the equations

$$\begin{cases} x_c = x(m_H, T_c) \\ y_c = y(m_H, T_c), \end{cases} \quad (11.4)$$

one can solve for the Higgs mass  $m_H$  and critical temperature  $T_c$  to which the phase transition in the 3d theory at the point  $(x_c, y_c)$  corresponds. When  $T_c$  is known, one can calculate the gauge coupling:  $g_3^2 = g_3^2(m_H, T_c)$ . Then one can determine  $v^2(T_c)/T_c^2$ , defined by  $v^2(T_c)/T_c^2 = 2\langle\phi_3^\dagger\phi_3(T_c)\rangle/T_c$  according to eq. (5.4), from

$$\frac{v^2(T_c)}{T_c^2} = 2\frac{g_3^2}{T_c} \left[ \ell_3^b - \frac{3}{16\pi^2} \ln \frac{g_3^2}{T_c} \right]. \quad (11.5)$$

The surface tension  $\sigma/T_c^3$  is obtained from

$$\frac{\sigma}{T_c^3} = \sigma_3 \frac{g_3^4}{T_c^2}. \quad (11.6)$$

For the latent heat  $L = T_c[p'_s(T) - p'_b(T)]$ , one gets

$$\begin{aligned} \frac{L}{T_c^4} &= \frac{1}{T_c^3} \frac{d}{dT} \left[ Tg_3^6 \Delta\epsilon_3(x, y) \right] \Big|_{T=T_c} \\ &= \Delta\ell_3 \frac{g_3^6}{T_c^2} \left( \frac{dy}{dT} - \frac{dx}{dT} \frac{dy_c}{dx_c} \right). \end{aligned} \quad (11.7)$$

Here we utilized eq. (11.2) together with the fact that at the critical line, the following two equations hold:

$$\Delta\epsilon_3(x_c, y_c) = 0, \quad (11.8)$$

$$\frac{\partial\Delta\epsilon_3(x, y)}{\partial x} = -\frac{dy_c}{dx_c} \frac{\partial\Delta\epsilon_3(x, y)}{\partial y}. \quad (11.9)$$

Note that both  $dx/dT$  and  $dy_c/dx_c$  in eq. (11.7) are non-zero through loop corrections:  $dx/dT$  is non-vanishing due to logarithmic 1-loop corrections to the dimensional reduction of the coupling constants  $g_3^2$ ,  $\lambda_3$ , and  $dy_c/dx_c$  is non-zero due to loop corrections inside the 3d theory (at tree-level, the phase transition takes place at  $y = 0$  independent of  $x$ ). Numerically,  $dy_c/dx_c \sim -1$  but  $dx/dT \ll dy/dT$ , so that in realistic cases

$$\frac{(dx/dT)(dy_c/dx_c)}{dy/dT} \sim 0.02. \quad (11.10)$$

Hence one does not need to determine the derivative of the critical line  $y = y_c(x)$  with as good a relative accuracy as the jump  $\Delta\ell_3$  of the order parameter at the point  $(x_c, y_c)$ . If one uses the parametrization of eqs. (2.8)-(2.10) in eq. (11.7), then  $dx/dT^* = 0$  and one gets the expression in eq. (5.3).

To get the values of  $\ell_3^b$ ,  $\Delta\ell_3$  and  $\sigma_3$  from the results given in Sec. 5, one has to use eqs. (11.5)-(11.7) in the inverse direction, employing the parametrization of eqs. (2.8)-(2.10). For instance, the surface tension  $\sigma/T_c^{*3} = 0.0023$  for  $m_H^* = 60$  GeV given in table 7 corresponds to  $\sigma_3 = 0.0023/0.44015^2 = 0.0119$  according to eqs. (11.6) and (2.8). The values of  $x_c$ ,  $y_c$ ,  $\ell_3^b$ ,  $\Delta\ell_3$  and  $\sigma_3$  obtained this way are shown in the second block in table 10. To go back to 4d units for different physical theories, one needs the true values of  $g_3^2/T_c$ ,  $x'(T_c)$  and  $y'(T_c)$ . In general, the value of  $g_3^2/T_c$  differs from 0.44015, so that  $\sigma/T_c^3$  differs from the value in table 7, see table 10.

The explicit form of the expressions for  $g_3^2$ ,  $x$  and  $y$  in terms of temperature and the physical 4d parameters of the Standard Model to order  $g^4$  have been given in [5], using the approximation  $g'^2 \sim g^3$ . With these relations, we can give results for the thermodynamical properties of the EW phase transition. To be more precise, we will consider three different theories reminiscent of the EW sector of the Standard Model. As a starting point, we consider the case  $m_Z = m_W$  so that  $g' = 0$ . This is a SU(2)+Higgs theory with the fermionic content of the Standard Model. The functions  $x(m_H, T)$ ,  $y(m_H, T)$  and  $g_3^2(m_H, T)$  in this theory, with  $m_{\text{top}} = 175$  GeV, have been given in figs. 7-8 of [5]. The results for the phase transition, obtained from the values in the second block in table 10 using eqs. (11.4)-(11.7), are shown in the fourth block in table 10. Results for the full Standard Model can be obtained from the SU(2)+Higgs+fermions model by taking into account the U(1)-subgroup perturbatively with the help of fig. 9 in [5]. The results are in the bottom block in table 10. Finally, we give results also for the SU(2)+Higgs model without fermions. This case is obtained from the SU(2)+Higgs+fermions model

by putting  $g_Y = n_F = \alpha_S = 0$  and fixing  $m_W = 80.22$  GeV. The results are shown in the third block in table 10. In principle, the results for the SU(2)+Higgs theory should allow a comparison with the 4d lattice simulations in [21, 22, 23]. At present such a comparison is not rigorously possible, however, since the relation of the gauge coupling  $g_R^2$  used in 4d simulations to continuum physics is not known.

## 12 Applications to cosmology

### 12.1 The phase transition

The results of non-perturbative lattice MC simulations allow one to considerably reduce the uncertainties associated with the dynamics of the electroweak phase transition. Strictly speaking, they still refer to a somewhat unphysical situation, since the U(1) subgroup present in the electroweak theory is omitted. As we discussed in the previous section, the perturbative effects associated with the U(1) subgroup are rather small; the estimate of the non-perturbative effects requires lattice simulations in the complete 3d SU(2) $\times$ U(1)+Higgs model. All specific estimates in this section are based on the assumption (quite reasonable, though) that all perturbative and non-perturbative effects of the U(1) subgroup are small.

Let us reconstruct the picture of the phase transition for  $m_H^* = 60$  GeV, for which we have the best lattice data. For the MSM with the top mass  $m_t = 175$  GeV this corresponds to the pole Higgs mass of  $m_H = 51.2$  GeV, excluded experimentally, but for a number of extensions of the Standard Model this may be quite realistic. To make the discussion less model dependent we will use the variable  $T^*$ ; with the help of the results of [5] and Sec. 11 everything can be re-computed for any specific model. We shall omit here the errorbars from the numbers.

The critical temperature of the phase transition is  $T_c^* = 138.4$  GeV, and the vev-temperature ratio at  $T_c^*$  is  $v/T_c^* = 0.67$ . The scalar correlation length in the symmetric phase is  $\xi_s \sim 6/T_c^*$ , and in the broken phase  $\xi_b \sim 8/T_c^*$ . The corresponding vector correlation lengths are a factor of three shorter. The domain wall separating the broken and symmetric phases has the surface tension  $\sigma \sim 0.002T_c^{*3}$ , and the profile of the scalar field has asymmetric tails on the different sides of the domain wall,  $\delta\phi(x) \sim \exp(-|x|/\xi_{s,b})$ . At  $T^* > T_+^* = 138.7$  GeV only the symmetric phase is stable, and at  $T^* < T_-^* = 137.4$  only the broken phase is stable, while in between both phases can exist simultaneously<sup>12</sup>. The bubble nucleation temperature  $T_{\text{bubble}}$  lies somewhere between  $T_c$  and  $T_-$  and may be estimated with the use of the surface tension and latent heat found on the lattice.

---

<sup>12</sup>We use here the results of subsection 7.2 which are the most accurate.

		$m_H^* = 35$ GeV	$m_H^* = 60$ GeV	$m_H^* = 70$ GeV
SU(2)+Higgs in 3d (perturbative)	$x_c$	0.01830	0.06444	0.08970
	$y_c$	0.0644(2)	0.0114(15)	0.0028(26)
	$\Delta\ell_3$	3.48(1)	0.493(5)	0.312(7)
	$\ell_3^b$	3.47(1)	0.508(17)	0.330(20)
	$\sigma_3$	0.339(1)	0.0401(7)	0.0253(9)
SU(2)+Higgs in 3d (lattice)	$x_c$	0.01830	0.06444	0.08970
	$y_c$	0.05904(56)	-0.00146(35)	-0.01531(69)
	$\Delta\ell_3$	4.07(13)	0.491(8)	0.302(18)
	$\ell_3^b$	3.91(13)	0.500(12)	0.353(26)
	$\sigma_3$	[0.47(1)]	0.0119(26)	?
SU(2)+Higgs in 4d	$m_H/\text{GeV}$	29.1	54.4	64.3
	$T_c/\text{GeV}$	76.85	132.6	151.2
	$L/T_c^4$	0.200	0.0294	0.0194
	$v/T_c$	1.74	0.626	0.529
	$\sigma/T_c^3$	[0.071]	0.0017	?
SU(2)+Higgs +fermions	$m_H/\text{GeV}$	–	51.2	68.0
	$T_c/\text{GeV}$	–	89.79	105.8
	$L/T_c^4$	–	0.103	0.0651
	$v/T_c$	–	0.642	0.542
	$\sigma/T_c^3$	–	0.0019	?
The Standard Model	$m_H/\text{GeV}$	–	51.2	68.0
	$T_c/\text{GeV}$	–	88.93	104.8
	$L/T_c^4$	–	0.124	0.0769
	$v/T_c$	–	0.689	0.575
	$\sigma/T_c^3$	–	0.0023	?

Table 10: Properties of the phase transition in different physical 4d theories. The simulations with  $m_H^* = 35$  GeV do not correspond to any physical pole Higgs mass in the SU(2)+Higgs+fermions model, at least according to the 1-loop formulas for the couplings used in [5]. The errors for the 2-loop perturbative results in the first block indicate the effect of varying  $\mu$  in the range  $0.5\mu_{\text{opt}} \dots 2.0\mu_{\text{opt}}$ . The error estimates for the 3d lattice SU(2)+Higgs model follow from the error estimates in Secs. 5.1-5.3. The surface tension measurements for  $m_H^* = 35$  GeV are in parentheses for reasons explained in Sec. 5.3. In the 4d results, we only show the central value. For the 4d SU(2)+Higgs model, the additional relative error from the relations to 4d should be below 1%, and for the SU(2)+Higgs+fermions model, it may be a few percent (in the critical temperature, the error is an order of magnitude smaller) [5]. The last block concerning the Standard Model is based on a purely perturbative estimate of the effect of the U(1)-subgroup [5, fig. 9], and the errors may be large if the non-perturbative effects related to the U(1)-sector are significant.

The thin wall bubble nucleation rate is given by

$$\Gamma = \kappa T_c^4 \exp\left(-\frac{4\pi\sigma R_c^2}{3T_c}\right) \quad (12.1)$$

where  $R_c = 2\sigma/\epsilon$  is the radius of the critical bubble,  $\epsilon = L\frac{\Delta T}{T_c}$  is the pressure difference between the broken and symmetric phases,  $\Delta T = T_c - T_{\text{bubble}}$ ,  $L$  is the latent heat of the transition, and  $\kappa$  is the prefactor. Estimates for  $\kappa$  in different models and approximations can be found in [48, 49]. The bubble nucleation temperature is roughly determined from the condition

$$\Gamma \frac{M_{Pl}^4}{T_c^8} \simeq 1. \quad (12.2)$$

Inserting the lattice numbers to these relations gives an estimate  $\frac{\Delta T^*}{T_c^*} \simeq 0.001$ , i.e., the bubble nucleation temperature is very close to the critical one,  $T_{\text{bubble}}^* = 138.3$  GeV. The smallness of  $\Delta T^*/T_c^*$  is due to fact that the ratio  $\sigma^3/L^2T_c^* \sim 10^{-5}$  is so small [50]. Since  $\Delta T^*/(T_c - T_-) \simeq 0.1$  is also small, one is in the thin-wall regime; indeed, the size of the bubbles when they nucleate is at least  $R_c \simeq 110/T_c^*$  which is much larger than the scalar correlation lengths in the broken and symmetric phases at  $T_{\text{bubble}}$ . Since  $T_{\text{bubble}}$  is very close to the critical temperature, the vev of the Higgs field at  $T_{\text{bubble}}$  is almost the same as at  $T_c^*$ .

## 12.2 The out of equilibrium condition for electroweak baryogenesis

One of the motivations for the study of the electroweak phase transition is its application to electroweak baryogenesis. The rate of the anomalous baryon number non-conserving processes is high in the symmetric phase [51], but is suppressed by the Boltzmann exponent in the broken phase [51]. Baryogenesis occurs at the 1st order electroweak phase transition, and the mechanism-independent constraint on the strength of the phase transition is that the rate of fermion number non-conservation in the broken phase at the bubble nucleation temperature be smaller than the rate of universe expansion [52].

We parametrize the rate of sphaleron transitions in the broken phase as

$$\Gamma = T^4 \left(\frac{\alpha_W}{4\pi}\right)^4 N_{\text{tr}} N_{\text{rot}} \left(\frac{2E_{\text{sph}}(T)}{\pi T}\right)^7 \exp\left(-\frac{E_{\text{sph}}(T)}{T}\right) \quad (12.3)$$

where the factors  $N_{\text{tr}} \simeq 26$  and  $N_{\text{rot}} \simeq 5.3 \times 10^3$  are zero mode normalizations [53] and  $E_{\text{sph}}(T)$  is the effective sphaleron mass at temperature  $T$ . Then the out of equilibrium constraint reads [52]:

$$E_{\text{sph}}(T_{\text{bubble}})/T_{\text{bubble}} > 45. \quad (12.4)$$

In principle, this bound can be converted into an upper bound on the parameter  $\lambda_3/g_3^2$ , completely defining the dynamics of the 3d theory. An exact determination of this bound would require a non-perturbative evaluation of the sphaleron rate in the broken phase (for lattice simulations of topology changing processes in the symmetric phase, see [54, 55]). Unfortunately, this problem has not been solved yet. Below we will estimate the critical value of  $\lambda_3/g_3^2$  assuming that the expansion parameter in the broken phase is  $g_3^2/(\pi m_T) = 2g_3/(\pi\phi_b)$  – a value inspired by the higher order computations and lattice simulations.

The best estimate of the sphaleron rate available now is the 1-loop computation in [56], where the determinant of small fluctuations was computed numerically in a bosonic theory<sup>13</sup>. According to [56], the rate in 1-loop approximation is just given by eq. (12.3), where

$$\frac{E_{\text{sph}}(T)}{T} = B\left(\frac{\lambda_3}{g_3^2}\right)\frac{2\pi T^{1/2}}{g_3}\frac{\phi_b}{T} \quad (12.5)$$

and  $\phi_b$  is the vev to be determined from the 1-loop effective potential (measured here in 4d units). Arguments in favour of absorption of the 1-loop effects into the vev of the scalar field have been presented in [59]. Some numerical values of the function  $B$  are: for  $m_H^* = 0, 40, 45, 50$ ,  $B = 3.04, 3.41, 3.44, 3.48$ , correspondingly [60]. We assume then that the exact value of the sphaleron mass is given by (12.5) plus corrections, and that  $\phi_b/T$  is to be replaced by the exact gauge-invariant value  $v/T$  determined on lattice. Then the first correction is of the order  $A(g_3^2/(\pi m_T))^2$ , where  $A$  is a number of the order of unity. A conservative limit on the ratio  $v/T$  is obtained when  $A$  is positive, so that  $v/T > 1.22$  (we take  $B$  corresponding to  $m_H^* = 50$  GeV). At this value the 2-loop correction is about 10% and the 3-loop correction is expected to be of the order of 4% and can be neglected. If, in the contrary,  $A$  is negative, we get  $v/T > 1.49$ .

Now, we choose the weaker constraint  $v/T > 1.22$  and convert it into an upper limit on  $m_H^*$ . Since we do not have lattice simulations for the whole range of  $m_H^*$  values from 35 GeV to 60 GeV, we take the 2-loop predictions for  $v/T$ ; as we discussed, this is accurate within a few percent. We find that if  $m_H^* \simeq 42$  GeV then  $v/T_c = 1.22$ . The bubble nucleation temperature is somewhat smaller than the critical temperature. The thin wall approximation for the tunneling rate is not applicable here. Assuming that the perturbative description of bubble nucleation is valid in this region of the Higgs masses, we estimate that  $v/T$  at the nucleation temperature is about 20% larger than at the critical temperature. This is derived by defining the bounce for the action

$$\frac{1}{2}(\partial\phi)^2 + V_{2\text{-loop}}(\phi) \quad (12.6)$$

---

<sup>13</sup>Recently the fermionic determinant in the background of a sphaleron was computed in [57]. The authors concluded that the fermionic contribution suppresses the rate and is numerically very important. However, the effect of fermions can be absorbed into the definition of the 3d coupling constants; after this the fermionic contribution is negligible, see [58].

numerically, and requiring that the value of the bounce action is  $\simeq 140$  (see, e.g., [61]). For example, for  $m_H^* = 43$  GeV,  $T_c^* = 108.6$  GeV,  $v(T_c^*)/T_c^* = 1.16$ ,  $T_{\text{bubble}} = 106.3$  GeV,  $v(T_{\text{bubble}})/T_{\text{bubble}} = 1.43$ . Then the requirement  $v/T > 1.22$  gives  $m_H^* < 46$  GeV. The perturbative account of the U(1) factor makes the phase transition stronger first order, correcting this bound by a factor

$$\sqrt{\frac{1}{3}\left(2 + \frac{1}{\cos^3 \theta_W}\right)} \quad (12.7)$$

following from the 1-loop effective potential. We then finally get  $m_H^* \lesssim 50$  GeV. If the correction to the sphaleron rate is in fact negative, then the number is smaller, about 45 GeV. It is interesting to note that this bound is very close to the initial 1-loop computation in [52]. We stress, however, that these estimates are subject to verification by the future lattice simulations of the theory with the U(1) subgroup and to non-perturbative evaluation of the sphaleron rate.

From eq. (2.9),  $m_H^* < 50$  GeV corresponds to  $x < 0.043$  and  $m_H^* < 45$  GeV to  $x < 0.034$ . To summarize, the upper limit to the parameter  $\lambda_3/g_3^2$  in the 3d SU(2) $\times$ U(1)+Higgs theory is likely to be

$$\lambda_3/g_3^2 < 0.04. \quad (12.8)$$

In order to define the constraints following from this requirement on the particle spectrum of the underlying 4d theory, one has to express this ratio through the physical parameters of the 4d theory at the critical temperature. This computation may be quite involved [5], but it is very clean from the physics point of view and does not contain any infrared divergencies. An essential point is that only *1-loop graphs need be computed*. Indeed, a 1-loop computation provides  $O(\alpha^2)$  accuracy in the coupling constants of the effective theory. Moreover, the critical temperature enters to the ratio (12.8) only through logarithms, so that even a 1-loop estimate of it will give sufficient accuracy.

The application of the constraint of eq. (12.8) to the case of the Minimal Standard Model follows immediately from fig. 8 of [5]. Indeed, if  $m_t = 175$  GeV, then *no Higgs mass* can ensure the necessary requirement of eq. (12.8)<sup>14</sup>. If the top quark were lighter, then some low Higgs mass value might be possible, see fig. 27.

According to [62] the phase transition in the MSSM occurs in the same way as it does in the MSM. If true, then MSSM also fails in generating a sufficiently strong first order phase transition. The two Higgs doublet model has more freedom, and the results of [63] indicate that the constraint (12.8) can be satisfied there.

---

<sup>14</sup>To be more precise, the computations in [5] relating the physical masses of the W boson and Higgs particle to the parameters of  $\overline{\text{MS}}$  scheme break down if the physical Higgs mass is close to the Coleman-Weinberg limit. In this limit the higher order Yukawa corrections start to be important in the procedure of dimensional reduction as well. So, it is not excluded that Higgs masses close to the Coleman-Weinberg limit are still possible.



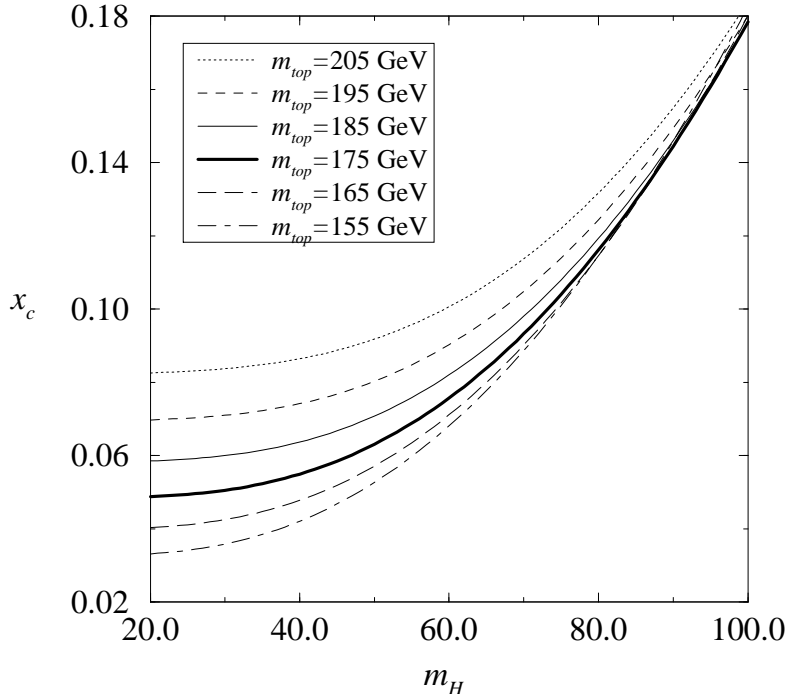


Figure 27: The critical value  $x_c = \lambda_3/g_3^2$  as a function of the physical Higgs mass  $m_H$  and the top quark mass  $m_{\text{top}}$ . In general,  $x$  depends on the Higgs mass, the top mass and logarithmically on the temperature. In calculating  $x_c$ , we have solved the temperature from the equation  $y = 0$ , which according to table 10 is very close to the true critical value of  $y_c$ . The small error in  $T_c$  does not affect  $x_c$  much due to the logarithmic dependence. The value of the dimensionless U(1)-coupling  $g_3^{\prime 2}/g_3^2$  is not shown in this figure; it is  $g_3^{\prime 2}/g_3^2 \approx 0.3$ .

## 13 Conclusions

The 3d formalism, developed in the series of papers [1]-[5],[16] provides a powerful tool for the study of phase transitions in weakly coupled gauge theories. It factorizes the perturbative and non-perturbative physics and allows one to construct effective 3d theories, describing in a universal way phase transitions in a large class of underlying 4d theories. The effective theories in 3d contain bosons only, and may be used for high precision lattice Monte Carlo simulations.

In this paper we reported on lattice simulations in the 3d SU(2)+Higgs model, which is an effective theory for the SU(2) sector of the MSM and its extensions. The nature of the phase transition at moderate Higgs masses  $m_H < m_W$  is clarified, and the results presented here form an “experimental” basis for different theoretical schemes attempting to describe strong coupling phenomena at  $T \sim T_c$ .

From the phenomenological point of view, to our mind, the most interesting further problems to be solved are the role of the U(1) factor in the phase transition, and the

rate of the sphaleron transitions in the broken phase near  $T_c$ . The solution of the first problem on the lattice is a straightforward generalization of the SU(2) case considered in this paper. The non-perturbative estimate of the sphaleron rate is a much more complicated problem, and it is even not clear how it can be solved in principle.

## Acknowledgements

We thank K. Farakos for collaboration during the early stages of the work. We are grateful to the Finnish Center for Scientific Computing and Indiana University for computational facilities. M.S. thanks Glennys Farrar for helpful comments and ITP, Santa Barbara for hospitality. K.R. is supported by the DOE grant # DE-FG02-91ER40661. This research was supported in part by the National Science Foundation under Grant No. PHY94-07194.

## Appendix A

In this Appendix we rederive the result (II.76-78) for  $\langle\phi^\dagger\phi\rangle$  in the  $\hbar$  (loop) expansion in the broken phase of the 3d SU(2)+Higgs theory writing it in a more explicit and complete form, and discuss the parametrisation of the 3-loop terms (the statistical uncertainties do not allow a determination of the 4-loop terms). The computation takes place in three steps: first find the potential (gauge and  $\mu$  dependent), then find the value  $V(v)$  of the potential at its broken minimum (gauge independent but  $\mu$  dependent)<sup>15</sup>, and finally calculate the condensate from

$$\langle\phi^\dagger\phi(\mu)\rangle = \frac{dV(v)}{dm_3^2(\mu)}. \quad (\text{A.1})$$

The starting point is the potential up to 3 loops ( $\hbar$  is a loop counting parameter):

$$V = V_0 + \hbar V_1 + \hbar^2 V_2 + \hbar^3 V_3. \quad (\text{A.2})$$

Perturbative computation gives  $V$  in the form  $V = V(m_T, m_1, m_2, \phi; \mu)$ , where

$$m_T = \frac{1}{2}g_3\phi, \quad m_1^2 = m_3^2(\mu) + 3\lambda_3\phi^2, \quad m_2^2 = m_3^2(\mu) + \lambda_3\phi^2. \quad (\text{A.3})$$

Thus, equivalently  $V = V(m_3^2(\mu), \phi; \mu)$ . Here, in contrast to eq. (A.1),  $\phi$  denotes the real Higgs field.

---

<sup>15</sup> Note that we have simplified notation here: by  $v$  we mean the the location of the minimum of the effective potential, previously denoted by  $\phi_b$ . The  $v$  used here should not be confused with the  $v(T)$  used previously and defined as  $v^2(T)/T^2 = 2\langle\phi^\dagger\phi(T)\rangle/T$ .

The tree and 1-loop potentials are

$$V_0 = \frac{1}{2}m_3^2(\mu)\phi^2 + \frac{1}{4}\lambda_3\phi^4, \quad (\text{A.4})$$

$$V_1 = -\frac{1}{12\pi}(6m_T^3 + m_1^3 + 3m_2^3), \quad (\text{A.5})$$

and the 2-loop part in the Landau gauge is in eq. (I.33), in the general covariant gauge in [43] and in the  $R(\xi)$  gauge in [44]. The 3-loop potential is near the classical broken minimum of the general form

$$V_3 = \frac{\partial V_1}{\partial m_3^2} \frac{f_{2m}}{16\pi^2} \left( \log \frac{\mu}{m_T} + \frac{1}{2} \right) - \frac{27}{128} \left( 2 + \frac{1}{2}h^3 \right)^2 \frac{g_3^4}{(4\pi)^3} \frac{m_T^2}{m_2} + \frac{\beta}{(4\pi)^3} g_3^4 m_T, \quad (\text{A.6})$$

where

$$\frac{\partial V_1}{\partial m_3^2} = -\frac{1}{8\pi}(m_1 + 3m_2), \quad h^2 \equiv \frac{8\lambda_3}{g_3^2}, \quad (\text{A.7})$$

and  $\beta$  is a complicated function of the masses, which we only need near the broken minimum. Note that  $h$  in eq. (A.7) differs from the definition in eq. (2.11).

The  $\mu$  dependent terms of  $V_3$  are known (eq. (I.70)) since they should cancel the  $\mu$  dependence of  $V_1$  so as to make the  $\mu$  dependence of  $V_1 + V_3$  to be of order  $\hbar^5$ .

The terms proportional to powers of  $1/m_2$  are singular at the tree minimum of the potential. They identically cancel when the value of the potential at the minimum is computed perturbatively, see below.

The effective potential itself is gauge dependent but its value in the broken minimum is gauge independent (but dependent on the scale  $\mu$ ). The minimum is defined by

$$\frac{\partial V(m_3^2(\mu), \phi; \mu)}{\partial \phi} = 0. \quad (\text{A.8})$$

Denoting the solution of this equation by  $\phi = v$  one can solve for it in the loop ( $\hbar$ ) expansion:

$$v^2 = v_{(0)}^2 + \hbar v_{(1)}^2 + \hbar^2 v_{(2)}^2 + \mathcal{O}(\hbar^3), \quad (\text{A.9})$$

with the result

$$v_{(0)}^2 = \frac{-m_3^2(\mu)}{\lambda_3}, \quad (\text{A.10})$$

$$v_{(1)}^2 = -\frac{2}{\lambda_3} V_1'(v_{(0)}^2) = \frac{3}{4\pi} \left( h + \frac{4}{h^2} \right) \bar{m}_T, \quad (\text{A.11})$$

$$\begin{aligned} v_{(2)}^2 &= \frac{4}{\lambda_3^2} V_1''(v_{(0)}^2) V_1'(v_{(0)}^2) - \frac{2}{\lambda_3} V_2'(v_{(0)}^2) \\ &= \frac{9\lambda_3}{32\pi^2} \left( 3 + \frac{8}{h^3} + \frac{\bar{m}_1}{m_2} \right) \left( 1 + \frac{4}{h^3} \right) - \frac{2}{\lambda_3} V_2'(v_{(0)}^2) \\ &= \frac{3g_3^2}{16\pi^2} \left[ \frac{3}{16} h^2 \left( 3 + \frac{8}{h^3} \right) \left( 1 + \frac{4}{h^3} \right) + 1 - \frac{5h}{4} - h^2 + \frac{h^3}{2} - \frac{3h^4}{8} + \frac{1}{2+h} \right]. \end{aligned} \quad (\text{A.12})$$

Here  $V'_n(v_{(0)}^2)$  etc. mean writing  $V_n = V_n(m_3^2, \phi)$ , taking partial derivative with respect to  $\phi^2$  and evaluating the result at the saddle point value (A.10). Hereby one will need the saddle point values of the masses:

$$\bar{m}_1 = h\bar{m}_T = \sqrt{-2m_3^2(\mu)}, \quad \bar{m}_2 = 0. \quad (\text{A.13})$$

The saddle point values satisfy the equations

$$\frac{d\bar{m}_T}{dm_3^2} = -\frac{1}{h^2\bar{m}_T}, \quad \frac{d\bar{m}_1}{dm_3^2} = -\frac{1}{\bar{m}_1}. \quad (\text{A.14})$$

The pole terms  $1/m_2$  in (A.12) cancel before taking the limit  $m_2 \rightarrow 0$ . These arise when taking derivatives of  $V_1 \sim m_3^2, V_2 \sim m_2, V_3 \sim 1/m_2$ , etc. In gauge invariant quantities calculated below they cancel and will not be explicitly written down.

Inserting (A.9) to (A.2) and expanding one gets

$$V(v) = V_0 + \hbar V_1 + \hbar^2 [V_2 - \lambda_3^{-1}(V'_1)^2] + \hbar^3 [V_3 + (V'_2 + \frac{1}{2}V''_1 v_{(1)}^2)v_{(1)}^2], \quad (\text{A.15})$$

where all quantities on the RHS should be evaluated at the saddle point values (A.13). Note that  $v^2$  is only needed up to 1 loop.

The potential at the minimum thus is the potential evaluated at the classical minimum corrected by some terms, related to one-particle reducible diagrams and calculable in terms of potentials of lower order. The result for the 3-loop one-particle reducible contribution is

$$\begin{aligned} (V'_2 + \frac{1}{2}V''_1 v_{(1)}^2)v_{(1)}^2 &= \frac{3}{2} \left( h + \frac{4}{h^2} \right) \bar{m}_T \frac{f_{2m}}{(4\pi)^3} \left( \log \frac{\mu}{\bar{m}_T} + \frac{1}{2} \right) + \\ &+ \beta_{\text{disc}}(h) \bar{m}_T \frac{g_3^4}{(4\pi)^3} + \\ &+ \frac{27}{128} \left( 2 + \frac{1}{2}h^3 \right)^2 \frac{g_3^4}{(4\pi)^3} \frac{\bar{m}_T^2}{m_2}, \end{aligned} \quad (\text{A.16})$$

where

$$\begin{aligned} \beta_{\text{disc}}(h) &= \frac{9}{32} \left( h + \frac{4}{h^2} \right) \left[ \left( \frac{1}{2}h^4 - 21 \right) \log 3 + h^4 \log h + \right. \\ &+ (4 - 3h^2 + h^4) \log(2+h) - h^2(1+h^2) \log(1+h) + \\ &\left. - \frac{21}{2} - \frac{6}{h^2} - \frac{5}{4}h - h^2 - h^3 + \frac{11}{16}h^4 - \frac{2}{2+h} \right]. \end{aligned} \quad (\text{A.17})$$

Defining further

$$f_2(h) = \frac{17}{2} + h^2 - \frac{1}{2}h^4, \quad (\text{A.18})$$

$$\frac{f_{2m}}{g_3^4} = \frac{3}{8} \left( \frac{17}{2} + 3h^2 - \frac{1}{2}h^4 \right), \quad (\text{A.19})$$

$$\begin{aligned} q_2(h) = & (2 - h^2 + \frac{1}{4}h^4) \log(2+h) - 2h + \frac{1}{4}h^2 - \frac{1}{2}h^3 + \\ & + \frac{1}{4}h^4 \log(3h) - \frac{21}{2} \log 3 - \frac{3}{2} - \frac{6}{h^2} - \frac{1}{4}h^4, \end{aligned} \quad (\text{A.20})$$

the vacuum energy density is

$$\begin{aligned} V(v) = & -\frac{m_3^4(\mu)}{\lambda_3} - \frac{\hbar}{12\pi} \bar{m}_T^3 (6 + h^3) + \\ & + \hbar^2 \bar{m}_T^2 \frac{3g_3^2}{64\pi^2} \left[ f_2(h) \left( \log \frac{\mu}{\bar{m}_T} + \frac{1}{2} \right) + q_2(h) \right] + \\ & + \hbar^3 \bar{m}_T \left[ \left( h + \frac{6}{h^2} \right) \frac{f_{2m}}{(4\pi)^3} \left( \log \frac{\mu}{\bar{m}_T} + \frac{1}{2} \right) + \right. \\ & \left. + [\beta_{\text{disc}}(h) + \beta(h)] \frac{g_3^4}{(4\pi)^3} \right]. \end{aligned} \quad (\text{A.21})$$

Computing  $\partial V(v)/\partial m_3^2$  gives the final result for the scalar condensate in loop expansion:

$$\begin{aligned} \frac{\langle \phi^\dagger \phi(\mu) \rangle}{g_3^2} = & \frac{\langle \phi^\dagger \phi(\mu_0) \rangle}{g_3^2} + \frac{3}{16\pi^2} \ln \frac{\mu}{\mu_0} = \\ & \frac{-m_3^2(\mu)}{2\lambda_3} \\ & + \frac{1}{4\pi} \left( h + \frac{6}{h^2} \right) \frac{\bar{m}_T(\mu)}{g_3^2} \\ & - \frac{1}{2\lambda_3} \frac{3}{8(4\pi)^2} g_3^4 \left[ f_2(h) \log \frac{\mu}{\bar{m}_T(\mu)} + q_2(h) \right] \\ & - \frac{1}{(4\pi)^3} \frac{g_3^2}{h^2 \bar{m}_T(\mu)} \left[ \frac{f_{2m}}{g_3^4} \left( h + \frac{6}{h^2} \right) \left( \log \frac{\mu}{\bar{m}_T} - \frac{1}{2} \right) + \beta_{\text{disc}}(h) + \beta(h) \right], \end{aligned} \quad (\text{A.22})$$

where the different loop contributions are on different lines and where  $\beta(h)$  is the 3-loop quantity to be determined. Note how the general  $\mu$  dependence arises from an incomplete cancellation between the tree and 2-loop terms and how the  $\mu$  dependence of the 1-loop term is compensated to order  $\hbar^5$  by the 3-loop term.

## Appendix B

In this appendix we describe an “improved” version of the 2-loop effective potential in Landau gauge used for the computation of the scalar condensate at different temperatures by the “Coleman-Weinberg” method.

It was pointed out in [4] (see also Appendix A) that the effective potential in the Landau gauge contains singularities at the classical tree minimum, where the Goldstone mass

$$m_2^2 = m_3^2 + \lambda_3 \phi^2, \quad (\text{B.1})$$

vanishes. The order of leading singularities on the  $n$ -loop level can be found from power counting:

$$V_n^{\text{sing}} = \frac{\hbar^n C_n}{(m_2^2)^{n-\frac{5}{2}}}, \quad (\text{B.2})$$

where the  $C_n$  are some coefficients. These terms are not dangerous if the location of the minimum of the effective potential is far enough from the tree-level value (this is the Coleman-Weinberg regime). However, deep in the broken phase the quantum corrections are small, the Goldstone mass  $m_2$  is close to zero and terms like (B.2) may become important. As we discussed in Sec. 5 of [4], due to the singular terms the computation of the ground state energy by the CW method, needed for the estimate of the value of the condensate  $\langle \phi^\dagger \phi \rangle$ , differs from the straightforward  $\hbar$  expansion described in Appendix A by fractional powers of  $\hbar$ ; at  $n$  loops, the difference is of order  $\hbar^{(n+\frac{1}{2})}$ . In particular, since the effective potential is known up to two loops, the difference between the two methods is of order  $\hbar^{\frac{5}{2}}$ . This is unacceptable since the  $\hbar^3$ -contribution to the effective potential is to be determined.

Below we show how this disadvantage of the CW method can be removed, so that the CW method can be used both near and far from the critical temperature.

The main idea is to redefine the 2-loop potential, including in it all leading singularities:

$$V_{2\text{-loop}}^{\text{improved}} = V_{2\text{-loop}} + \sum_{n=3}^{\infty} V_n^{\text{sing}}. \quad (\text{B.3})$$

In this way, the expression for the ground state energy becomes analytic in  $\hbar$ , as it must be in the broken phase, where there are no massless physical excitations. It is interesting that the requirement that the  $\hbar^{\frac{5}{2}}$  correction be absent in the expression for the ground state energy is powerful enough to determine the structure of the leading singularities.

Let us rewrite the tree and 1-loop effective potentials in the following form:

$$V_0 = \frac{1}{4\lambda_3} z^4, \quad V_1 = -\frac{\hbar}{12\pi} [6m_W^3 + m_H^3 + 3z^3] - \frac{1}{2\lambda_3} m_G^2 z^2 + O(z^4). \quad (\text{B.4})$$

Here  $m_W = \frac{1}{2}g_3\sqrt{(-m_3^2)/\lambda_3}$  and  $m_H^2 = -2m_3^2$  are the tree-level values of the W and Higgs masses,  $z = m_2$  and

$$m_G^2 = \frac{3\hbar}{8\pi} g_3^2 (m_W + \frac{2\lambda_3}{g_3^2} m_H). \quad (\text{B.5})$$

Then the solution to the minimization equation  $\frac{\partial V_{\text{eff}}}{\partial z} = 0$  has the form

$$z^2 = m_G^2 + O(\hbar^{\frac{3}{2}}). \quad (\text{B.6})$$

Now, if this solution is used in computing the values of the singular parts of the effective potential in eq. (B.2), one can see that any of the  $n$ -loop contributions is of order  $\hbar^{\frac{3}{2}}$ . Since such a term must be absent, we get

$$\sum_{n=1}^{\infty} V_n^{\text{sing}}(z^2 = m_G^2) = 0. \quad (\text{B.7})$$

Therefore, the whole sum must have the form

$$\sum_{n=1}^{\infty} V_n^{\text{sing}}(z) = -\frac{\hbar}{4\pi}(z^2 - m_G^2)^{\frac{3}{2}} \quad (\text{B.8})$$

in order to reproduce correctly the known 1-loop term  $\sim z^3$ , which is non-analytic in  $z^2$ .

In this derivation the explicit form of the 2-loop potential was not used, so that the prediction of the term non-analytic in  $\hbar^2$  may be compared with the direct 2-loop computation. From [2], the non-analytic terms on the 2-loop level are

$$V_2^{\text{sing}} = \frac{\hbar^2}{(4\pi)^2} \frac{9}{4} g_3^2 (m_W + \frac{2\lambda_3}{g_3^2} m_H) m_2 = \frac{3\hbar}{8\pi} m_G^2 z, \quad (\text{B.9})$$

indeed coinciding with the  $\hbar$  expansion of eq. (B.8).

To conclude, the improved form of the effective potential, which reproduces the correct structure of the  $\hbar$  expansion of the ground state energy, has the form

$$V_{2\text{-loop}}^{\text{improved}} = V_{2\text{-loop}}(m_2^2 \rightarrow m_2^2 - m_G^2) - \frac{3}{8\pi} m_G^2 m_2, \quad (\text{B.10})$$

where the last term must be subtracted in order to avoid double-counting. It is this potential which was used for the computation of the scalar condensate at fixed temperature by the CW method in Sec. 4.

## Appendix C

Here we calculate the W and Higgs correlators in the 3d theory of eq. (1.1) at 1-loop order. The Lagrangian masses of the vector, Higgs and Goldstone fields are in eq. (A.3). With these masses, the radiatively corrected propagators of the vector and Higgs fields are of the form

$$\begin{aligned} \langle A_i^a(-p) A_j^b(p) \rangle &= \delta^{ab} \frac{\delta_{ij} - p_i p_j / p^2}{p^2 + m_T^2 - \Pi^W(p^2)} + \text{longitudinal part}, \\ \langle \phi_1(-p) \phi_1(p) \rangle &= \frac{1}{p^2 + m_1^2 - \Pi^H(p^2)}. \end{aligned} \quad (\text{C.1})$$

To calculate the self-energies  $\Pi^W$ ,  $\Pi^H$ , one needs the basic integrals

$$A_0(m^2) = \int dp \frac{1}{p^2 + m^2} = -\frac{m}{4\pi}, \quad (\text{C.2})$$

$$\begin{aligned} B_0(k^2; m_1^2, m_2^2) &= \int dp \frac{1}{[p^2 + m_1^2][(p+k)^2 + m_2^2]} \\ &= \frac{i}{8\pi(k^2)^{1/2}} \ln \frac{m_1 + m_2 - i(k^2)^{1/2}}{m_1 + m_2 + i(k^2)^{1/2}}. \end{aligned} \quad (\text{C.3})$$

The integration measure here is

$$\int dp \equiv \int \frac{d^d p}{(2\pi)^d}, \quad (\text{C.4})$$

where  $d = 3 - 2\epsilon$ .

The contributions of the diagrams in fig. 28.a to the vector self-energy  $\Pi^W$  in eq. (C.1) are (V is a vector, S a scalar, and  $\eta$  a ghost propagator;  $k^2$  is the Euclidian external momentum)

$$\begin{aligned} \Pi_{\text{SS}}^W &= -\frac{g_3^2}{8} \left\{ B_0(k^2; m_1^2, m_2^2) \left[ k^2 + 2(m_1^2 + m_2^2) + \frac{(m_1^2 - m_2^2)^2}{k^2} \right] \right. \\ &\quad + B_0(k^2; m_2^2, m_2^2) (k^2 + 4m_2^2) \\ &\quad \left. + [A_0(m_1^2) - A_0(m_2^2)] \left( \frac{m_1^2 - m_2^2}{k^2} \right) - A_0(m_1^2) - 3A_0(m_2^2) \right\}, \end{aligned} \quad (\text{C.5})$$

$$\begin{aligned} \Pi_{\text{VV}}^W &= g_3^2 \left\{ B_0(k^2; m_T^2, m_T^2) \left[ 5k^2 - 4m_T^2 + \frac{k^4}{m_T^2} - \frac{k^6}{8m_T^4} \right] \right. \\ &\quad + B_0(k^2; m_T^2, 0) \left[ \frac{(k^2 + m_T^2)^2}{4m_T^4 k^2} (k^4 - 6k^2 m_T^2 + m_T^4) \right] \\ &\quad \left. + B_0(k^2; 0, 0) \left( -\frac{k^6}{8m_T^4} \right) + A_0(m_T^2) \left[ \frac{5}{12} - \frac{3}{2} \frac{k^2}{m_T^2} + \frac{(k^2 + m_T^2)^2}{4k^2 m_T^2} \right] \right\}, \end{aligned} \quad (\text{C.6})$$

$$\begin{aligned} \Pi_{\text{SV}}^W &= \frac{g_3^2}{8} \left\{ B_0(k^2; m_1^2, m_T^2) \left[ -k^2 - 2m_1^2 + 6m_T^2 - \frac{(m_1^2 - m_T^2)^2}{k^2} \right] \right. \\ &\quad + B_0(k^2; m_1^2, 0) \frac{(k^2 + m_1^2)^2}{k^2} \\ &\quad \left. + A_0(m_T^2) \left[ 1 + \frac{m_1^2 - m_T^2}{k^2} \right] + A_0(m_1^2) \frac{m_T^2}{k^2} \right\}, \end{aligned} \quad (\text{C.7})$$

$$\Pi_{\eta\eta}^W = \frac{g_3^2}{4} k^2 B_0(k^2; 0, 0), \quad (\text{C.8})$$



$$\Pi_S^W = -\frac{g_3^2}{4} [A_0(m_1^2) + 3A_0(m_2^2)], \quad (\text{C.9})$$

$$\Pi_V^W = -\frac{8}{3} g_3^2 A_0(m_T^2). \quad (\text{C.10})$$

For the 1-loop contributions to the Higgs self-energy  $\Pi^H$  in eq. (C.1), one gets from the diagrams in fig. 28.b the results

$$\Pi_{SS}^H = 6\lambda_3^2 \phi^2 [3B_0(k^2; m_1^2, m_1^2) + B_0(k^2; m_2^2, m_2^2)], \quad (\text{C.11})$$

$$\begin{aligned} \Pi_{VV}^H = & \frac{3}{8} \frac{g_3^2}{m_T^2} \left\{ B_0(k^2; m_T^2, m_T^2) [k^4 + 4k^2 m_T^2 + 8m_T^4] \right. \\ & - 2B_0(k^2; m_T^2, 0)(k^2 + m_T^2)^2 \\ & \left. + B_0(k^2; 0, 0)k^4 - 2A_0(m_T^2)m_T^2 \right\}, \end{aligned} \quad (\text{C.12})$$

$$\begin{aligned} \Pi_{SV}^H = & \frac{3}{4} \frac{g_3^2}{m_T^2} \left\{ B_0(k^2; m_T^2, m_2^2) [k^4 + 2k^2(m_T^2 + m_2^2) + (m_T^2 - m_2^2)^2] \right. \\ & - B_0(k^2; m_2^2, 0)(k^2 + m_2^2)^2 \\ & \left. + A_0(m_T^2) [m_T^2 - m_2^2 - k^2] - A_0(m_2^2)m_T^2 \right\}, \end{aligned} \quad (\text{C.13})$$

$$\Pi_S^H = -3\lambda_3 [A_0(m_1^2) + A_0(m_2^2)], \quad (\text{C.14})$$

$$\Pi_V^H = -\frac{3}{2} g_3^2 A_0(m_T^2). \quad (\text{C.15})$$

## References

- [1] K. Kajantie, K. Rummukainen and M. Shaposhnikov, Nucl. Phys. B 407 (1993) 356.
- [2] K. Farakos, K. Kajantie, K. Rummukainen and M. Shaposhnikov, Nucl. Phys. B 425 (1994) 67 [hep-ph/9404201].
- [3] K. Farakos, K. Kajantie, K. Rummukainen and M. Shaposhnikov, Phys. Lett. B 336 (1994) 494 [hep-ph/9405234].
- [4] K. Farakos, K. Kajantie, K. Rummukainen and M. Shaposhnikov, Nucl. Phys. B 442 (1995) 317 [hep-lat/9412091].

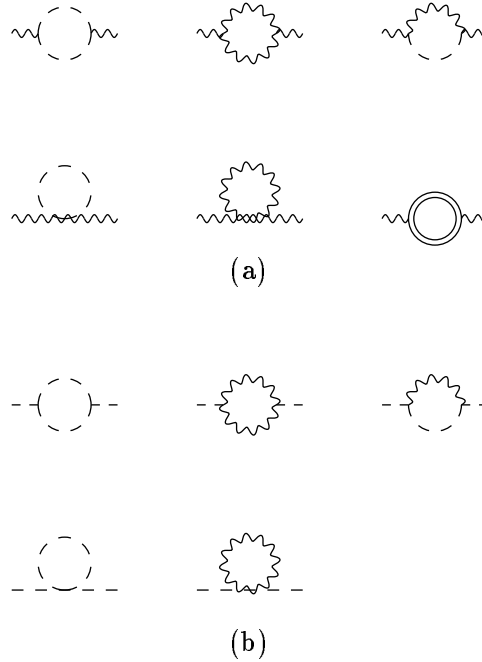


Figure 28: The diagrams needed for calculating (a) the self-energy of the W boson, and (b) the self-energy of the Higgs particle. Dashed line is a scalar propagator, wiggly line a vector propagator, and double line a ghost propagator.

[5] K. Kajantie, M. Laine, K. Rummukainen and M. Shaposhnikov, CERN-TH/95-226 [hep-ph/9508379].

[6] P. Ginsparg, Nucl. Phys. B 170 (1980) 388.

[7] R. Jackiw and S. Templeton, Phys. Rev. D 23 (1981) 2291.

[8] T. Appelquist and R. Pisarski, Phys. Rev. D 23 (1981) 2305.

[9] S. Nadkarni, Phys. Rev. D 27 (1983) 917.

[10] N.P. Landsman, Nucl. Phys. B 322 (1989) 498.

[11] A. Jakovác, K. Kajantie and A. Patkós, Phys. Rev. D 49 (1994) 6810.

[12] A. Jakovác and A. Patkós, Phys. Lett. B 334 (1994) 391.

[13] E. Braaten and A. Nieto, Phys. Rev. Lett. 73 (1994) 2402; Phys. Rev. Lett. 74 (1995) 3530; Phys. Rev. D 51 (1995) 6990; NUHEP-TH-95-10 [hep-ph/9508406].

- [14] F. Karsch, T. Neuhaus and A. Patkós, Nucl. Phys. B 441 (1995) 629.
- [15] E.-M. Ilgenfritz, J. Kripfganz, H. Perlt and A. Schiller, Phys. Lett. B 356 (1995) 561.
- [16] M. Laine, Nucl. Phys. B 451 (1995) 484 [hep-lat/9504001].
- [17] K. Farakos, K. Kajantie, M. Laine, K. Rummukainen, M. Shaposhnikov, IUHET–316 [hep-lat/9509086], in proceedings of LATTICE '95, Nucl. Phys. B, in press.
- [18] P. Damgaard and U. Heller, Nucl. Phys. B 294 (1987) 253.
- [19] H.G. Evert, J. Jersák and K. Kanaya, Nucl. Phys. B 285 (1987) 229.
- [20] B. Bunk, E.-M. Ilgenfritz, J. Kripfganz and A. Schiller, Phys. Lett. B 284 (1992) 371; Nucl. Phys. B 403 (1993) 453.
- [21] F. Csikor, Z. Fodor, J. Hein, K. Jansen, A. Jaster and I. Montvay, Phys. Lett. B 334 (1994) 405.
- [22] Z. Fodor, J. Hein, K. Jansen, A. Jaster and I. Montvay, Nucl. Phys. B 439 (1995) 147.
- [23] F. Csikor, Z. Fodor, J. Hein and J. Heitger, Phys. Lett. B 357 (1995) 156.
- [24] A.D. Kennedy, B.J. Pendleton, Phys. Lett. B 156 (1985) 393.
- [25] Z. Fodor and K. Jansen, Phys. Lett. B 331 (1994) 119.
- [26] A. Berg and T. Neuhaus, Phys. Lett. B 267 (1991) 249.
- [27] A. Hebecker, Z. Phys. C 60 (1993) 271.
- [28] A.M. Ferrenberg and R.H. Swendsen, Phys. Rev. Lett. 61 (1988) 2635.
- [29] H.J. Herrmann, W. Janke and F. Karsch, eds., *Dynamics of first order phase transitions* (World Scientific, 1992).
- [30] C. Borgs and R. Kotecký, J. Stat. Phys. 61 (1990) 79; C. Borgs, R. Kotecký and S. Miracle-Solé, J. Stat. Phys. 62 (1991) 529.
- [31] K. Rummukainen, Nucl. Phys. B 390 (1993) 621; A. Billoire, R. Lacaze and A. Morel, Nucl. Phys. B 370 (1992) 773.
- [32] K. Binder, Phys. Rev. A 25 (1982) 1699.
- [33] B. Bunk, Int. J. Mod. Phys. C 3 (1992) 889.

- [34] M. Caselle, F. Gliozzi and S. Vinti, Phys. Lett. B 302 (1993) 74.
- [35] Y. Iwasaki, K. Kanaya, L. Kärkkäinen, K. Rummukainen and T. Yoshié, Phys. Rev. D 49 (1994) 3540.
- [36] M.M. Tsypin, Phys. Rev. Lett. 73 (1994) 2015 [hep-lat/9401034].
- [37] T. Banks and E. Rabinovici, Nucl. Phys. B 160 (1979) 349.
- [38] E. Fradkin and S. Shenker, Phys. Rev. D 19 (1979) 3682.
- [39] P. Arnold and L.G. Yaffe, Phys. Rev. D 49 (1994) 3003.
- [40] M. Reuter and C. Wetterich, Nucl. Phys. B 408 (1993) 91.
- [41] M. Shaposhnikov, Phys. Lett. B 316 (1993) 112.
- [42] W. Buchmüller and O. Philipsen, Nucl. Phys. B 443 (1995) 47.
- [43] M. Laine, Phys. Lett. B 335 (1994) 173; Phys. Rev. D 51 (1995) 4525.
- [44] J. Kripfganz, A. Laser and M.G. Schmidt, Phys. Lett. B 351 (1995) 266.
- [45] H.-G. Dosch, J. Kripfganz, A. Laser and M.G. Schmidt, HD-THEP-95-42 [hep-ph/9509352].
- [46] W. Buchmüller, Z. Fodor, T. Helbig and D. Walliser, Ann. Phys. 234 (1994) 260.
- [47] M. Quirós, J.R. Espinosa and F. Zwirner, Phys. Lett. B 314 (1993) 206.
- [48] W. Buchmüller and T. Helbig, in [29], p.27.
- [49] J. Baacke and A. Surig, DO-TH-95-08 [hep-ph/9505435]; J. Baacke, DO-TH-95-04 [hep-ph/9503350].
- [50] J. Ignatius, K. Kajantie, H. Kurki-Suonio and M. Laine, Phys. Rev. D 50 (1994) 3738.
- [51] V.A. Kuzmin, V.A. Rubakov and M.E. Shaposhnikov, Phys. Lett. B 155 (1985) 36.
- [52] M.E. Shaposhnikov, JETP Lett. 44 (1986) 465, Nucl. Phys. B 287 (1987) 757.
- [53] P. Arnold and L. McLerran, Phys. Rev. D 36 (1987) 581.
- [54] J. Ambjørn, T. Askgaard, H. Porter and M. Shaposhnikov, Nucl. Phys. B 353 (1991) 346.

- [55] J. Ambjørn and A. Krasnitz, NBI-HE-95-23 (1995) [hep-ph/9508202].
- [56] J. Baacke and S. Junker, Phys. Rev. D 49 (1994) 2055; Phys. Rev. D 50 (1994) 4227.
- [57] D. Dyakonov, M. Polyakov, P. Pobylytsa, P. Sieber, J. Schaldach and K. Goeke, Phys. Lett. B 336 (1994) 457; Phys. Rev. D 49 (1994) 6864.
- [58] G.D. Moore, PUPT-1557 [hep-ph/9508405].
- [59] A. Bochkarev and M. Shaposhnikov, Mod. Phys. Lett. A 2 (1987) 417.
- [60] S. Braibant, Y. Brihaye and J. Kunz, Int. J. Mod. Phys. A 8 (1993) 5563.
- [61] A.D. Linde, *Particle Physics and Inflationary Cosmology* (Harwood, 1990).
- [62] G.F. Giudice, Phys. Rev. D 45 (1992) 3177.  
J.R. Espinosa, M. Quirós and F. Zwirner, Phys. Lett. B 307 (1993) 106.  
A. Brignole, J.R. Espinosa, M. Quirós and F. Zwirner, Phys. Lett. B 324 (1994) 181.
- [63] A.I. Bochkarev, S.V. Kuzmin and M.E. Shaposhnikov, Phys. Lett. B 244 (1990) 275; Phys. Rev. D 43 (1991) 369.  
N. Turok and J. Zadrozny, Nucl. Phys. B 369 (1992) 729.